5-2014

Rotordynamic Analysis of a Two-Pole Synchronous Motor with Sleeve and Pressure Dam Bearings

Justin Matthew Garrard
University of Tennessee - Knoxville, jgarrard@utk.edu

To the Graduate Council:

I am submitting herewith a thesis written by Justin Matthew Garrard entitled "Rotordynamic Analysis of a Two-Pole Synchronous Motor with Sleeve and Pressure Dam Bearings." I have examined the final electronic copy of this thesis for form and content and recommend that it be accepted in partial fulfillment of the requirements for the degree of Master of Science, with a major in Mechanical Engineering.

Trevor Moeller, Major Professor

We have read this thesis and recommend its acceptance:

Joseph Wehrmeyer, Milt Davis

Accepted for the Council:
Carolyn R. Hodges

Vice Provost and Dean of the Graduate School

(Original signatures are on file with official student records.)

Rotordynamic Analysis of a Two-Pole Synchronous Motor with Sleeve and Pressure Dam Bearings

A Thesis Presented for the

Master of Science

Degree

The University of Tennessee, Knoxville

Justin Matthew Garrard

May 2014

Dedication

To my parents, Doug and Angelia,

for their continued love and support.

They have taught me the value of hard work,

given me the push required to fulfill my dreams,

and whose suggestions and encouragement made this all possible.

Acknowledgements

I would first like to thank my father, Dr. Glenn D. Garrard, for constantly pushing me to continue my education, better myself, and not the least of which for checking this thesis in its entirety. Next, I would like to thank my committee, Dr. Trevor Moeller, Dr. Joseph Wehrmeyer, and Dr. Milton Davis, Jr., for providing guidance and furthering my education over the course of my Masters studies. I would also be remiss if I did not thank my co-workers Joseph Capps, Gary Jarrell, and Don Brandt for their mentorship and help with understanding motor operations and the field of rotordynamics. Without them, I never would have considered this as a possible thesis topic and it has opened up to me a field which I hope to continue to contribute as my career continues. Finally, the work reported herein was done at Arnold Engineering Development Complex (AEDC) on the author's own time. This report was approved for public release on March 24, 2014 under AEDC PA Number: AEDC2014-037. Distribution is unlimited.

Abstract

A two-pole synchronous motor was recently rewound for the von Karman Gas Dynamics facility at Arnold Engineering Development Complex, Arnold Air Force Base, Tennessee. After installing the rewound rotor, unexpected vibration amplitudes were recorded during motor checkouts. To resolve this issue, an investigation was initiated to investigate the causes of the vibration issues. The investigation discovered that the original design used sleeve bearings rather than pressure dam bearings. A study was formed to determine the effect of changing the pressure dam bearings back to sleeve bearings. Because only one spare bearing shell existed, the bearing with the highest vibration amplitudes was chosen to be switched. A lateral rotordynamic analysis was performed to determine the impact of this switch, prior to performing the bearing swap.

The rotordynamic model predicted that the rotor was operating near the second critical speed. Regardless of the bearing change, the second critical speed was not impacted. However, the determination was made to change the bearing to the sleeve bearing due to predicted lower vibration amplitudes. From the motor checkout runs, the model prediction was verified and the sleeve bearing was kept. Vibration amplitudes have been reduced, but issues still remain with the rotor operation near the second critical speed. Further analysis is required to successfully shift the rotor operation away from the second critical speed.

Table of Contents

List of Figures

List of Symbols/Nomenclature

A	Finite element cross-sectional area
AC	Alternating current
AEDC	Arnold Engineering Development Complex
ASME	American Society of Mechanical Engineers
c	Damping coefficient
c_x	Damping coefficient, x-direction
c_y	Damping coefficient, y-direction
C	Radial clearance
C_b	Radial clearance in DyRoBeS©
C_d	Pressure dam clearance
C_p	Lubricant specific heat
DC	Direct current
e	Rotor eccentricity, O_b-O_j
e_m	Eccentricity of unbalanced mass on Jeffcott rotor
E	Modulus of elasticity, also known as Young's modulus
F	Fluid film reaction force
F_x	Fluid film reaction force, x-direction
F_y	Fluid film reaction force, y-direction
$F_{u,x}$	Unbalance force, x-direction
$F_{u,y}$	Unbalance force, y-direction
G	Shear modulus
G_x	Turbulent flow coefficient, x-direction
G_y	Turbulent flow coefficient, y-direction
h	Lubricant film thickness

I	Area moment of inertia
I_d	Diametral moment of inertia
I_p	Polar moment of inertia
k	Stiffness coefficient
k_x	Stiffness coefficient, x-direction
k_y	Stiffness coefficient, y-direction
k_{ij}	Stiffness matrix coefficients
L	Finite element length
m	mass
$M_{u,x}$	Unbalance moment, x-direction
$M_{u,y}$	Unbalance moment, y-direction
Npad	Number of bearing pads
O_b	Bearing center
O_j	Journal (rotor) center
p	Lubricant pressure
PLC	Programmable Logic Controller
s	Spatial coordinates
r	Orbit radius
R_b	Bearing radius
R_j	Journal (rotor) radius
Re	Reynold's number, $Re = \frac{\rho U h}{\mu}$
t	Time
t_n	Time at value n, n=0,1,2,...etc.
T	Temperature
U	Surface velocity

VFSS Variable frequency starting system

W Bearing load, half the rotor weight for two bearing system

x Horizontal coordinate

x_c Centerline of finite element, x-direction

y Vertical coordinate

y_c Centerline of finite element, y-direction

z Axial coordinate

G Gyroscopic matrix

K Stiffness matrix

$\mathbf{K_b}$ Bending stiffness matrix

$\mathbf{K_\beta}$ Shear stiffness matrix

$\mathbf{K_a}$ Axial force stiffness matrix

$\mathbf{M_T}$ Translational mass matrix

$\mathbf{M_r}$ Rotational inertia matrix

q Time-dependent end point displacement vector

u Nodal variable vector

y Mode shape vector (eigenvector)

γ Spin-whirl ratio

δ Log-decrement, damping ratio of mode

ζ_x Viscous damping factor, x-direction

ζ_y Viscous damping factor, y-direction

η Non-dimensionalized y-coordinate for finite element grid generation

θ Angle from x-axis, bearing circumferential pad angle, or journal rotational angle

θ_h Angle measured from bearing-journal line of centers to location of calculated film thickness

κ Heat conductivity

μ Lubricant absolute viscosity

ν Poisson's ratio, negative ratio of transverse to axial strain particular to each material

ξ Non-dimensionalized x-coordinate for finite element grid generation

ρ Density, fluid or solid

ϕ Attitude angle of journal, angle between load and bearing/journal line of centers

ϕ_u Phase angle of unbalance force

Φ Transverse shear parameter

ω Journal (rotor) angular velocity

ω_x Damped natural frequency, x-direction

ω_{nx} Undamped natural frequency, x-direction

ω_y Damped natural frequency, y-direction

ω_{ny} Undamped natural frequency, y-direction

Ω Critical speed (eigenvalue)

$\boldsymbol{\Psi}$ Shape function matrix

1.0 Introduction

1.1 Background

The von Karman Gas Dynamics Facility (VKF), located at Arnold Engineering Development Complex (AEDC), Arnold Air Force Base, Tennessee, contains three continuous flow wind tunnels: Tunnels A, B, and C. Primarily used in the development of supersonic and hypersonic aircraft, the tunnels can be used to simulate conditions with flight Mach numbers ranging from 1.5 to 10 and temperatures up to 1440°R [1]. In order to move the volume of air required to meet these conditions, a nine stage compressor system driven by five (18,500 horsepower each) electric motors is used. Each electric motor contains a steel rotor which is machined from one block of steel. The rotor has two non-salient poles, wrapped in copper windings and insulated with G10 insulation material [2] between the windings which prevents shorts and acts as retaining blocks for the copper windings. A picture of a comparable rotor is shown in Figure 1 [3].

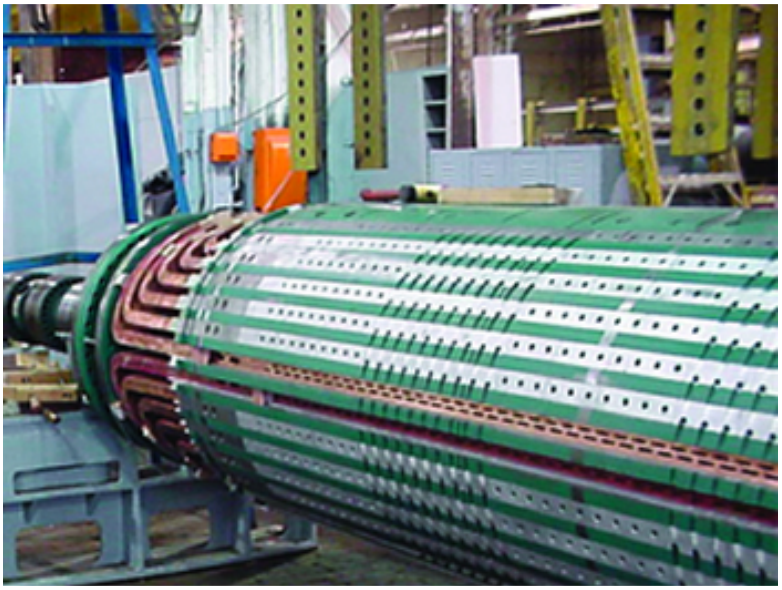

Figure 1 – Example of Two Pole Rotor Construction

A direct current (DC) voltage is applied to the rotor using a slip ring assembly with carbon brushes, creating a magnet. A variable frequency start system (VFSS) applies an alternating current (AC) at varying frequency to the motor stator which causes the rotor to begin to spin with the alternating electromagnetic field of the stator. As the frequency of the alternating current reaches 60 Hz, which is the incoming transmission line frequency, the motor is synchronized with the incoming line frequency and the VFSS drops off as the synchronization breaker is closed. Multiplying the line frequency by 120 and dividing by the number of poles calculates the synchronous speed of the rotor, which equals 3600 rotations per minute (RPM) in this case.

During operation, the electricity running through the copper windings causes the windings to heat up, which causes the windings to expand. The windings are designed to expand and contract in the rotor slip planes, shown above in Figure 1 running axially across the rotor. Over multiple years; however, this constant heating and cooling can lead to the copper windings binding in their slip plane or delaminating at the ends of the windings where they wrap around the pole. This process may create short circuits and can eventually lead to failure of the motor, showing up in increased vibration levels which eventually become untenable for motor operation. To fix this problem, the rotor can be removed from service and rewound with new copper windings, as shown in Figure 2 [4].

Figure 2 – Rewinding of Two Pole Rotor

A major refurbishment project was begun in late 2009 to repair the VKF motors due to their age and issues with vibration levels on the machines creeping upward. The motors were rewound and each rotor was balanced in a high speed balancing pit to ensure minimal vibration during operation. Once this was performed, the motors were then shipped back and reinstalled in the VKF facility. Following installation, motor checkouts were performed to ensure the motors performed as expected across its operational design envelope. During operational checkouts, two problems were detected. First, vibration levels were higher than expected and higher than that shown in the balance pit, a facility which runs the rotor to operational speed for balancing purposes after the rewind is completed. Second, oil leaks from the hydrodynamic bearings became frequent during these checkouts. An investigation was begun to look into the source of these issues.

Several causes were proposed as to the source of the vibrations. Prior rotordynamic studies suggested that the system is running near the second critical speed, which can lead to instabilities that make the rotor difficult to balance. The critical speed of the rotor is the angular velocity which excites a natural frequency of the rotor where resonances occur which can lead to large increase in system vibration. Also, any error in the rewinding process can lead to thermal sensitivity, a problem which causes the rotor to bow as the rotor temperature rises [5]. Thermal sensitivity can be caused by numerous issues with the rotor rewinding process, including shorted turns, coil expansion restriction, slot wedge binding, and many other issues with the winding. Any one of these issues can make the rotor difficult to balance which can lead to rewinding the rotor.

The motors were originally designed to use sleeve bearings. The current installation used pressure dam bearings. Pressure dam bearings are typically more stable, and requires more make up oil flow into the bearing to maintain the proper oil film. The forced feed oil lubrication system for the motor bearings were designed for sleeve bearings, and the question was raised whether to switch the bearing type back to the sleeve bearing.

1.2 Problem Statement

The VKF motor was suffering from high vibration levels and oil leaks stemming from improper system design for the bearing type which was installed in the motor. Since there was some belief that the rotor was operating near the second critical speed, it was desired to shift the critical speed away from the rotor operational speed of 3600 rpm. One of the methods of shifting the critical speed is to change the bearing types. Since the bearings installed in the motor were already different than the original design, it was decided to change the bearing type back from a pressure dam to a plain journal (sleeve) bearing. A rotordynamic analysis was required to check if this change would affect the operation of the motor.

This thesis seeks to detail and document the three major tasks stemming from the proposed bearing switch. First, a finite element analysis was performed using a rotordynamic software package to simulate the system with both bearing types, sleeve and pressure dam. Next, the system was instrumented and data were recorded with the system operating with each bearing type. Finally, the data taken from the two individual runs were compared to the predictions made using the finite element analysis. Using the model and the data, a determination will be made whether to keep the sleeve bearings or switch back to the pressure dam bearing. The inherent problem that this thesis seeks to answer is as follows: will the change of bearing type from pressure dam to sleeve result in a more stable rotor-bearing system?

1.3 Problem Approach

Understanding the dynamics of a rotor-bearing system is important to diagnosing and analyzing problems that may arise when operating large scale rotating machinery. Modeling the system is important to gain a comprehension of how the rotor will deform during steady state running conditions as well as transient conditions such as startup and shut down. This vibration created by the rotating

machinery will need to be minimized in order to ensure mechanical reliability of the equipment. There are several important items to understand during a rotor-bearing system analysis, including bearing stability and performance, rotor critical speeds, and rotor orbits.

Varying bearing designs will impact the overall stability of the rotating system and can influence vibration with different bearing stiffness and damping coefficients applied to the rotating system. The rotor has specific natural frequencies which are important to avoid when operating the machinery, as this can cause resonance which greatly amplifies vibration. These critical speeds can be shifted depending on the bearing stiffness and damping. The rotor orbit, showing the travel of the rotor centerline from a fixed location, can be measured to ensure there are no mechanical faults such as misalignment, bearing lubrication instabilities such as whirl or whip, or any other items of note that occur during operation of the rotor system.

Prior to performing any change to a rotor-bearing system, it is desirable to build an analytical model to ensure that the change won't shift a critical speed towards the system running speed. Other important items to be included in the rotordynamic analysis is a look at the system's behavior to an unbalance, or a torsional analysis to see if any torsional natural frequencies exist near that of the exciting frequency (i.e. the electrical frequency of the motor). This can be exceedingly difficult to perform by hand for rotors such as the motor rotor included in this study, for various reasons including the effects of the copper windings on the steel shaft, numerous shaft sections of varying diameters and lengths, and shrunk-on pieces such as the winding retaining rings.

The use of a computer code to perform this analysis is a valuable tool. DyRoBeS©, a software package developed and sold by Rodyn Vibration Analysis, Inc. [6], is used to perform a rotor-bearing analysis using a finite element based code to perform the tasks detailed above. The rotor and each bearing type are modeled using the DyRoBeS© software and the results were analyzed to determine whether to proceed with the bearing change. Provided no major red flags are seen in the results, then

the new bearings will be machined and installed in the machine. The mathematical underpinnings of the DyRoBeS© software and a look at the results will be described in Appendix I, Appendix II, and Chapter 3, respectively, of this thesis.

During the aforementioned motor checkouts, the system was instrumented and a data logger saved data from the runs with the pressure dam bearings. This same system was used to record data from the checkout runs with the journal bearings installed. The probes were connected to a National Instruments IOtech dynamic signal analyzer which was connected to a laptop. National Instruments ez-TOMAS™ (Total Online Monitoring and Analysis Software) was used to record the data and perform the analysis during both checkouts. Afterwards, the data were compared to those predicted results from the DyRoBeS© simulation.

With the results in hand and the data analyzed, the determination must be made whether to switch from pressure dam to sleeve bearings permanently. If the vibration levels are improved and the system model matches the experimental results, then the sleeve bearings will be kept. If the vibration levels are improved but the model doesn't match the physical data, then the sleeve bearings will be kept and an investigation into the weaknesses of the model should be described as well as proposed improvements for future iterations of the model. If the vibration levels aren't improved but the model predicts an improvement, then further investigation is required into either possible weaknesses of the model or whether there is a potential thermal sensitivity problem creating the high vibration levels.

2.0 Literature Review

2.1 Background

Rotordynamics as a field of study has spanned approximately 145 years. In 1869, Rankine published "On the Centrifugal Force of Rotating Shafts" [7], which is believed to be the first reference to vibrations in a rotating system, and thus the first paper fully devoted to rotordynamics. Rankine showed that past a certain angular velocity, the flexible rotor is "…bent, and whirls around in this bent form." This speed, defined by Rankine as the whirling speed but now known as the critical speed, influenced the design of machinery for many years afterwards. Rankine believed, incorrectly, that above this speed a "centrifugal force" would overcome the restoring elastic force of the rotor, causing the whirl amplitude to become unbounded. This prediction was due to an incorrect reading of Rankine's free-body diagram of the whirling rotor, which is depicted in Figure 3 [8].

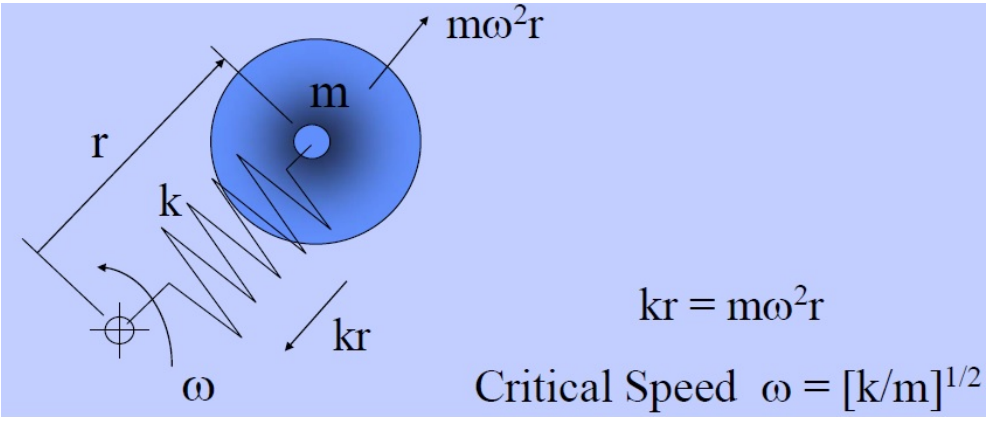

Figure 3 – Rankine's Rotor Free Body Diagram

Rankine predicted a centrifugal force, the rotor mass m multiplied by the square of the angular velocity ω by the whirl orbit radius r, which pulls the rotor outward. Unfortunately for Rankine and machine designers of the era, this force does not actually exist. The spring force k (which is the stiffness

of the rotor-bearing system) acts on the rotor mass to produce the centripetal acceleration, which is the angular velocity squared multiplied by the orbit radius. Because Rankine's predicted force grows unbounded above the critical speed, he believed that it wasn't allowable to run the rotor above this speed, since this force would eventually cause the rotor to fail.

The flaw in this analysis was not accepted in a widespread manner for quite some time. De Laval and Parsons individually developed machines that operated well above this critical speed in the mid 1880's. In this way, the practice of rotordynamics far exceeded the accepted theory for quite some time. Dunkerley published a paper in 1894 detailing the fact that a shaft has multiple critical speeds, correlating to the natural frequency of the shaft [9]. Dunkerley also developed a method for calculating the first critical speed. A German engineer, August Föppl, showed just one year later a rotor solution that appeared to be valid for speeds higher than the critical (i.e. supercritical) [10].

Despite these findings, it wasn't until 1916 that the engineering community began to consider the possibility of designing machines to operate above the first critical speed. Kerr found evidence of a second critical speed above the first, which could only be reached by safely passing the first [11]. With the preponderance of evidence tipping against Rankine's hypothesis, the Royal Society of London commissioned Henry Jeffcott to resolve the dichotomy of Rankine's approach and the experimental findings of Kerr and Foppl. Jeffcott published his classic paper in response to this commission in 1919, "On the Lateral Vibration of Loaded Shafts in the Neighbourhood of a Whirling Speed" [12].

2.2 Jeffcott's Contribution

Jeffcott's landmark paper established that a stable supercritical solution existed. Jeffcott developed a model that is frequently used to this day to describe the basic attributes of a flexible rotor operating above the first critical speed. The Jeffcott model depicts an unbalanced disc located on a symmetric flexible shaft, shown in Figure 4 [13].

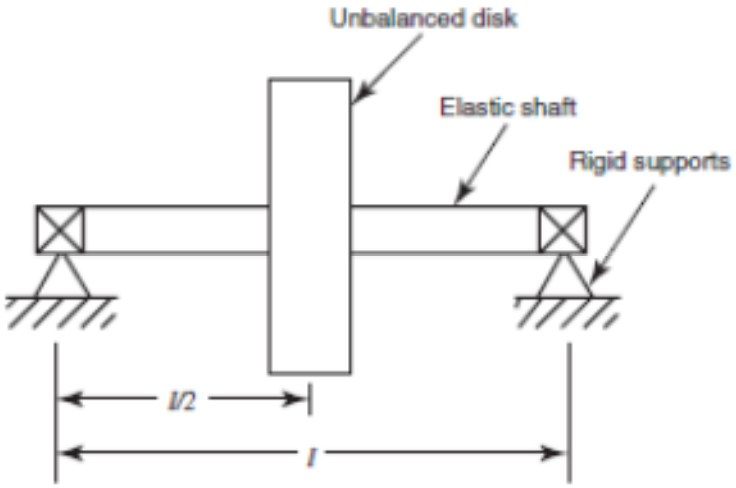

Figure 4 – Jeffcott Rotor

Because the disk is mounted in the center of the shaft, the first two fundamental translational and rotational motions are decoupled and can be solved using basic beam deflection equations. Jeffcott also used the model to explain the effects of unbalance when the angular velocity is near the natural frequency of the rotor. He showed that vibration amplitude increases rapidly in that region depending on the amount of unbalance. His model included both vertical and horizontal motion of the rotor, which therefore defined the orbital motion of the rotor. The equations of motion for the Jeffcott Rotor are as follows.

$$m\ddot{x} + c\dot{x} + kx = me_m\omega^2 \cos(\omega t + \phi_u) \tag{2.1}$$

$$m\ddot{y} + c\dot{y} + ky = me_m\omega^2 \sin(\omega t + \phi_u) \tag{2.2}$$

Jeffcott defined a damping force, c, which was proportional to the velocity of the lateral motion of the shaft. He also defined the eccentricity, e_m, of the unbalanced mass from the mass center. The phase angle of the unbalanced mass on the disk, ϕ_u, is defined here but for the single unbalanced force of the original Jeffcott paper can be set to zero without loss of generality [14]. From these two

equations, the undamped natural frequency, viscous damping factor, and damped natural frequency for each direction of the rotor can be calculated.

$$\omega_{nx} = \sqrt{\frac{k_x}{m}}, \zeta_x = \frac{c_x}{2m\omega_{nx}}, \omega_x = \omega_{nx}\sqrt{1-\zeta_x^2} \tag{2.3}$$

$$\omega_{ny} = \sqrt{\frac{k_y}{m}}, \zeta_y = \frac{c_y}{2m\omega_{ny}}, \omega_y = \omega_{ny}\sqrt{1-\zeta_y^2} \tag{2.4}$$

Any excitation with a frequency that aligns with the rotor system natural frequency will create a state of resonance. One of the most common excitation forces is that of a rotor unbalance. When the rotor angular velocity coincides with the rotor natural frequency, the rotor unbalance will excite a rotor resonance. This angular velocity is known as a critical speed of the rotor. Using Jeffcott's equations of motion, the differential equations shown in equations 2.1 and 2.2 can be solved to depict the rotor behavior before, during, and after reaching the first critical speeds and further. From Jeffcott's model, several important results of rotordynamic behavior were shown. First, an increase in damping results in an increase in the critical speed of the rotor. The damping is also responsible for reducing vibration amplitude at the critical speed. Second, as the angular velocity is increased through the critical speeds, the phase angle changes. This can be used to predict the critical speed. Finally, instead of the rotor instability causing the amplitude of vibration to continue increasing past the critical speed, the center of mass comes around inside of the rotor whirl orbit, and the rotor rotates about the center of gravity. Future analysis would build off of Jeffcott's rotor model, further enhancing rotordynamic modeling capabilities, and providing better predictions of rotor behavior.

2.3 Jeffcott to Myklestad-Prohl

In 1924, Stodola [15] summarized all of the rotordynamic developments up to that point in his seminal work, *Steam Turbines*. Stodola presented methods of calculating critical speeds of rotors with

variable cross sections and showed that the supercritical solutions (i.e. above the first critical speed) were stabilized by coriolis accelerations. Stodola also was the first to include gyroscopic moments for rotors that have disks on them that wobble, such as fan blades or pump impellers. A Stodola-Green rotor, shown in Figure 5, is a rotor with an overhung disk like that of a cantilever beam and is often used as a prime example of these gyroscopic effects.

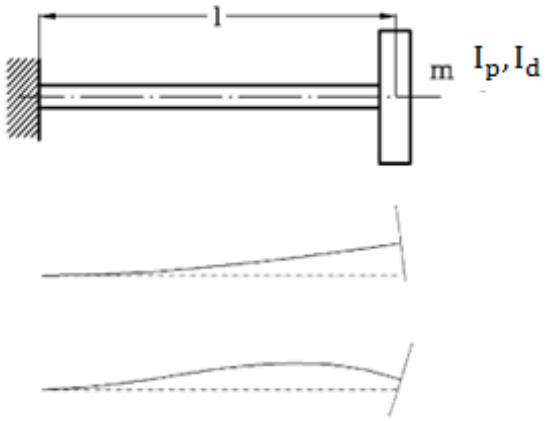

Figure 5 – Stodola-Green Rotor and Corresponding Mode Shapes

Multiple other sources of instability were found in the following years. Kimball [16] described rotor internal damping, which is a supercritical instability in built up rotors between the individual components. Newkirk and Taylor [17] were the first to introduce the possibility of instabilities introduced by the bearing supporting the rotor. At high speeds, the oil wedge can become unstable introducing oil whirl which can lead to oil whip. Smith [18] showed formulas that predicted threshold spin speed for super critical instability and showed that they varied with bearing stiffness and ratio of internal to external damping. External damping refers to the damping from the stationary element of the rotating machine to the rotor, while internal damping is that integral to the rotor itself, such as the material internal dissipation of mechanical energy or friction from built on rotor parts [19].

With all of these advancements, the analysis of many rotor variations was made possible. This would not be nearly enough to fulfill the needs of industry. The dynamic behavior of gas turbines, high speed compressors, and many others were outside of the modeling capabilities of a Jeffcott or modified Jeffcott model. Further developments were required to make rotordynamic analyses commonplace. Prohl and Myklestad in 1944/45 independently developed work which led to a method that did just that, known as the Transfer Matrix Method (TMM) [20,21]. This method models a flexible rotor as a number ($8<N<80$) of lumped inertias connected by massless elastic shaft sections. Point and field matrices, for the inertia and shaft elements, respectively, are multiplied together to give expressions for the boundary conditions at the right end of the rotor in terms of the boundary conditions at the left end [22]. The coefficients which result from this analysis form what is called the overall transfer matrix.

2.4 Lund and Gunter to Present Day

The 1960's were predominantly dedicated to studying hydrodynamic bearings and their impact in rotordynamic stability problems. Numerous papers written by Lund [23-28] and Gunter [29-34] pushed rotor-bearing stability analysis to the forefront of rotor dynamics. Both men studied various types of bearings and their effects on the rotor. Multiple bearing types including plain journal, pressure dam, multi-lobe, and tilt pad bearing types were investigated over the course of the 1960's and 1970's. Lund [23, 26, 27] contributed greatly to the transfer matrix method and created computer codes to solve critical speed analyses for many rotor bearing systems.

The 1970's introduced the finite element method (FEM) to rotordynamic analyses. Ruhl and Booker [35] were the first to apply the finite element model to a rotor-bearing system in 1972. Nelson and McVaugh [36] further enhanced the method to include rotary inertia, gyroscopic moments, and axial forces. Finite element methods can be used to solve for bearing solutions to determine bearing

coefficients under various load characteristics. Nicholas [37-41] used the finite element method to solve for pressure dam and tilting pad bearing coefficients.

The finite element method is currently the backbone of many current rotordynamic codes. DyRoBeS©, the code used for the analysis in the following chapters, uses finite element methods to perform rotor-bearing system analysis. The code allows the user to combine flexible shafts, flexible disks, flexible bearings, and flexible supports into a single model [13]. Other codes include ANSYS©, XL-Rotor, and VT-FAST. In the present day, systems combining FEM and solid modeling techniques are combined to create one major large overarching model which includes cross coupling between couplings, flexible disks, flexible shafts, flexible foundations, and flexible bearings.

From the 1970's onward, research of various rotordynamic issues has exploded. Textbooks written by some of the field's top researchers such as Gunter, [14], Vance [22], Rao [42], and Childs [43] are invaluable for teaching engineers new to the field about performing rotordynamic analysis. Turbomachinery labs at Texas A&M [44] and Virginia Tech [45] are pushing the field further by researching magnetic bearings and extremely high speed rotors. Texas A&M hosts yearly rotordynamic symposiums with papers that are investigating the cutting edge of rotordynamic analysis. The American Society of Mechanical Engineers (ASME) Journals of Rotordynamics, Turbomachinery, and Tribology are pushing the field forward with every publication. The following will describe multiple papers written by various authors which proved particularly useful during the course of this thesis.

Allaire and Flack [46] described various journal bearing types and their design for rotating machinery. Leader [47], and Zeidan and Herbage [48] also went in depth with various bearing designs and bearing dynamics with regards to rotor systems. Other papers by He, Cloud, and Byrne [49] and San Andres [50] were also useful in regards to bearing design and modeling. Kirk [51-53] wrote several papers which were useful in understanding rotordynamic instabilities. Mirro [54] described several

design deficiencies in existing equipment using modern rotordynamic analysis tools. Graybeal [55] showed various applications for diagnosing electrical machines using vibration analysis. Finally, Jordan [56] gave a good description of what orbit plots show that was extremely helpful in interpreting the data results shown in Chapter 4.0.

Since the time of Rankine, rotordynamic analysis has matured as a field of study. While at times practice appeared to outpace theory, the field is mature enough now that most practical problems in rotor-bearing systems can be explained or modeled appropriately using the correct tools and techniques. The practice of performing a rotordynamic analysis has become so common that the American Petroleum Institute has created a standard, API 684 [13], which describes the required steps for any new or existing machine analysis. The rotor-bearing model created in DyRoBeS© for the purpose of performing the rotordynamic analysis is shown in the following chapter.

3.0 Rotor-Bearing System Model

3.1 Bearing Analysis

The study of friction, lubrication, and wear of interacting surfaces [57] has been an important one since the beginning of the machine age. Without a proper understanding of the dynamics of bearing operation, advances in rotating machinery would not have been possible. Proper bearing design ensures reliable, stable operation for all kinds of machinery. As such, this field has seen an increasing amount of study over the past century, resulting in methods to completely analyze bearing properties to insert into large scale rotor-bearing systems with multiple components. The properties of various bearing types, such as plain, pressure dam, three-lobe, four-lobe, and tilting pad have all been analyzed for various rotor configurations.

This study concerns itself with two primary bearing designs, the sleeve bearing and the pressure dam bearing. The sleeve bearing, shown in Figure 6 [50], simply consists of a plain bearing cylinder of radius R_b with the rotor (journal) of radius R_j rotating within it with a radial clearance between the two, here shown as C. While the journal is rotating, a thin film of incompressible, Newtonian lubricant fills the clearance between the journal and the bearing shell. This film thickness is designated h. The journal bearing center is typically designated as O_b and the journal center is O_j. The difference between the two, e, is known as the journal eccentricity. The journal eccentricity can change with time and depends on the external forces on the bearing. The eccentricity cannot exceed the bearing clearance, or else a catastrophic failure will occur. Finally, the attitude angle, ϕ, is the angle between the load (the weight of the rotor the bearing is supporting) and the line of centers, the line between the journal center and the bearing center [50].

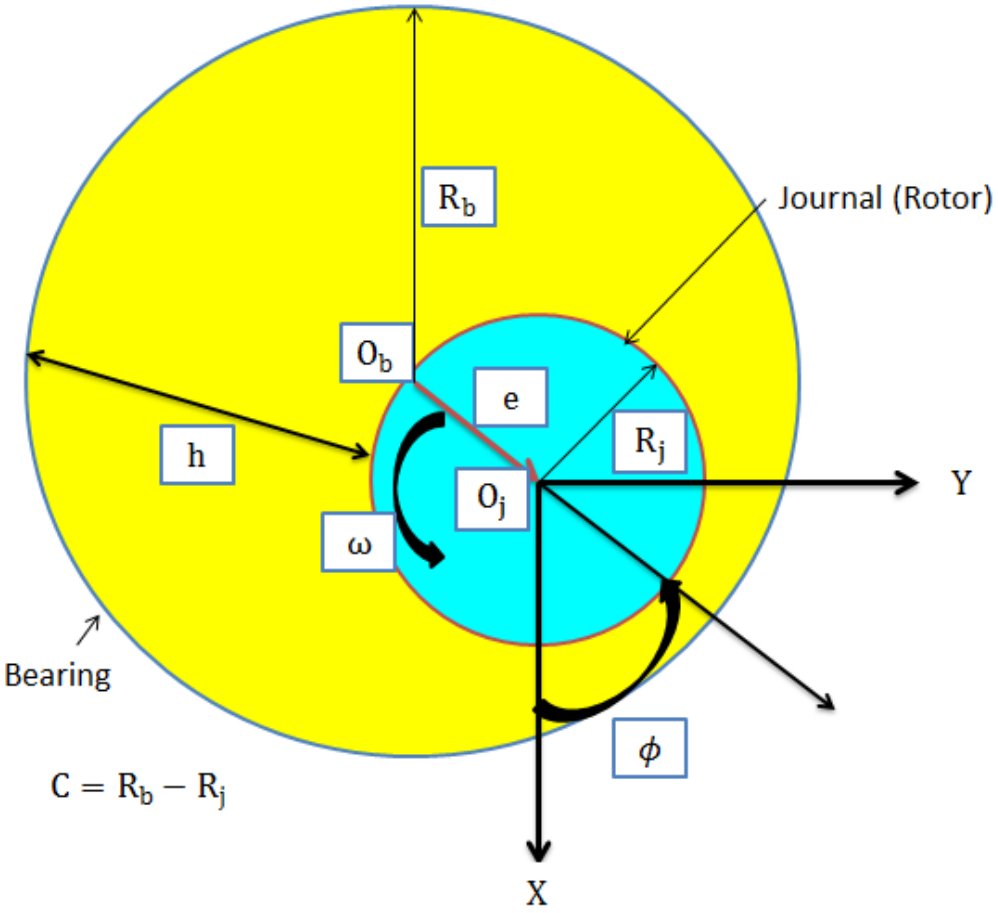

Figure 6 – Sleeve Bearing

Pressure dam bearings, also known as step bearings, are similar to sleeve bearings except they have a machined dam in the upper half surface of the bearing. A cross-sectional view of the pressure dam bearing is shown in Figure 7 [40]. The step produces a pressure rise at the dam which creates a hydrodynamically generated load on the journal [37]. The artificial load increases stability over that of a sleeve bearing. A circumferential relief track is machined in the bottom half of the bearing as well to provide further stability. Both of these work together to induce a minimum eccentricity in the bearing at high speeds or low loads, which will be shown later to enhance the stability of the bearing.

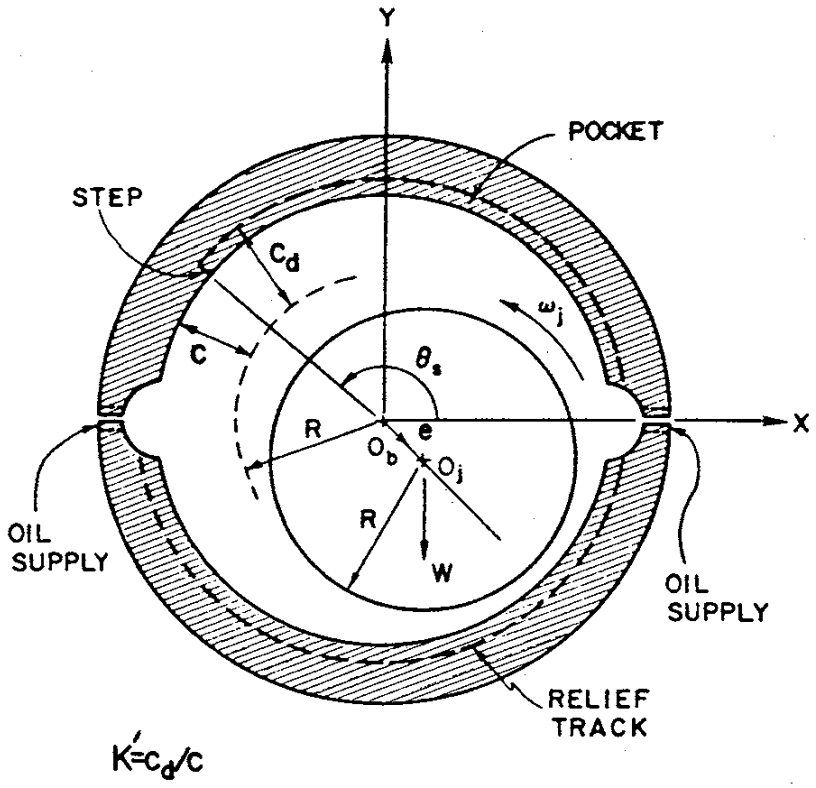

Figure 7 – Pressure Dam Bearing

For a given operating condition, with journal speed ω and load W, the journal has a given eccentricity and attitude angle. At static equilibrium, the fluid film reaction force F and load W are balanced. At ω=0 and at constant load, the journal sits at the bottom of the bearing. As the speed increases, the journal rises along the journal centers moves along the journal equilibrium locus towards the bearing center (e=0) as ω increases to infinity. For constant ω, the journal sits at the bearing center and moves along the locus until it reaches the bottom of the bearing when the load reaches infinity. For rotors operating with large eccentricities, full hydrodynamic lubrication is not reached and the film thickness is very small. For high ω and low W, the attitude angle ϕ becomes large and the eccentricity small. The tangential force created by the fluid film under these circumstances can destabilize the rotor-bearing system, known as oil whirl and oil whip.

If the journal and bearing are completely separated by the lubricating oil, full hydrodynamic lubrication is obtained. The lubricant is drawn into the thin converging wedge due to the high shear forces created by the rotating journal. This creates a pressure wave which is shown in Figure 8 [13].

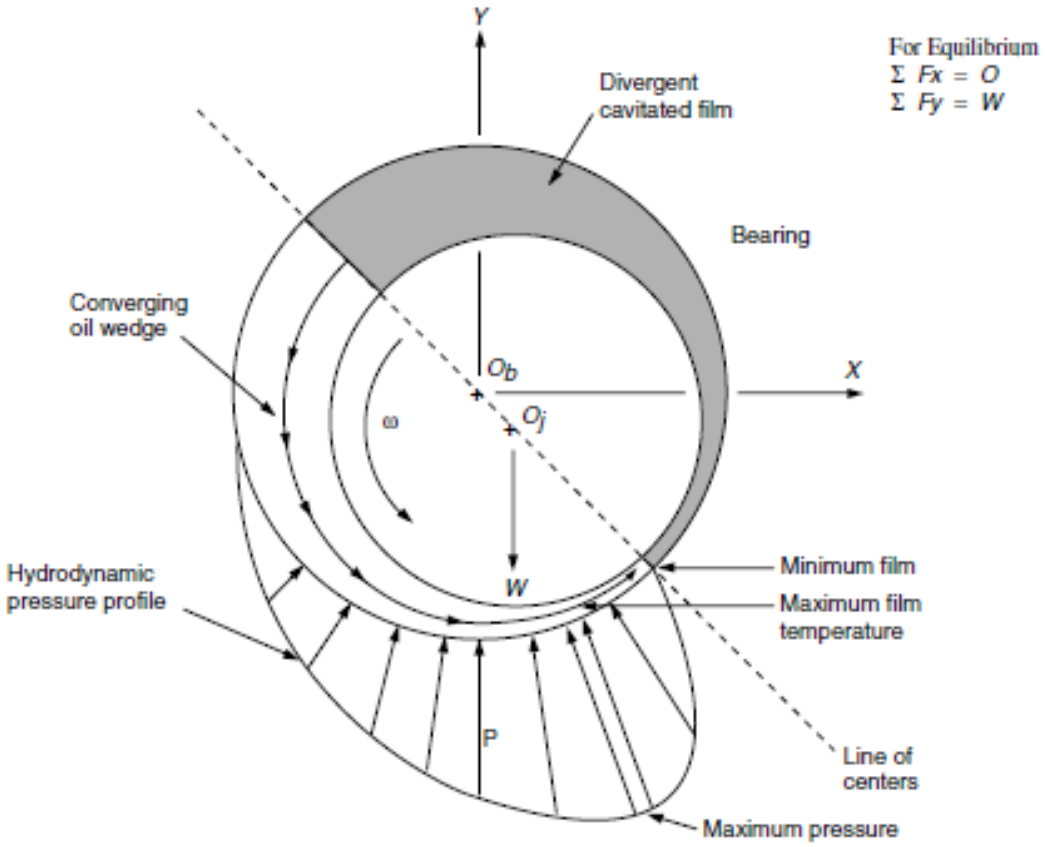

Figure 8 – Hydrodynamic Film in Journal Bearing

The pressure, P, builds to allow the lubricant to escape the thin clearance. The film's pressure distribution and velocity distributions are governed by the continuity and three dimensional momentum equations. A theoretical solution of any bearing requires a simultaneous solution of the four equations. For a summary of the equations and their solution using the finite element method, reference Appendix I. The following section will present the results from the sleeve bearing.

3.2 Sleeve Bearing Model

Sleeve bearings are the most common type of hydrodynamic bearings. As discussed in Section 3.1, sleeve bearings simply consist of a plain cylinder in which the rotor spins on a film of oil which is provided through forced lubrication by oil supply holes in the bearing. Incompressible lubricant fills the space between the bearing surface and rotor. For the VKF motors, the length of the bearings are eight inches, with a diameter of seven inches. The diametral clearance of the bearing is 12 mils, or 0.012 inches. Looking at the bearing axially, the bearing is shown as in Figure 9.

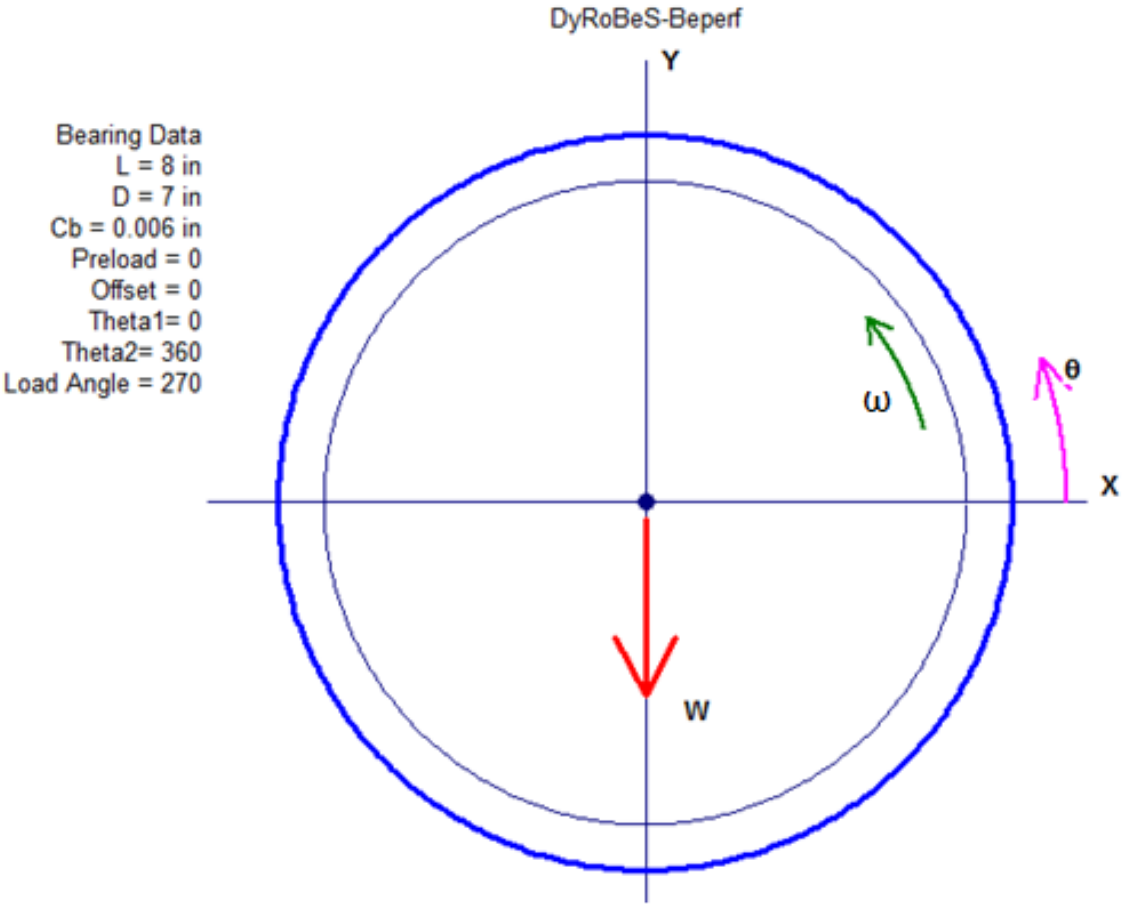

Figure 9 – Sleeve Bearing DyRoBeS© Screen

A dimensional analysis in DyRoBeS© was performed to solve for the required stiffness and dampness coefficients required for the rotor-bearing model. The DyRoBeS© input screen is shown in Figure 10. A heat balance analysis was chosen with 70% of the heat generated by the spinning rotor taken away by the oil. This effects the viscosity of the oil, as higher temperature oil is less viscous. A heat balance with 70-80% of the heat removed is typical for these analyses.

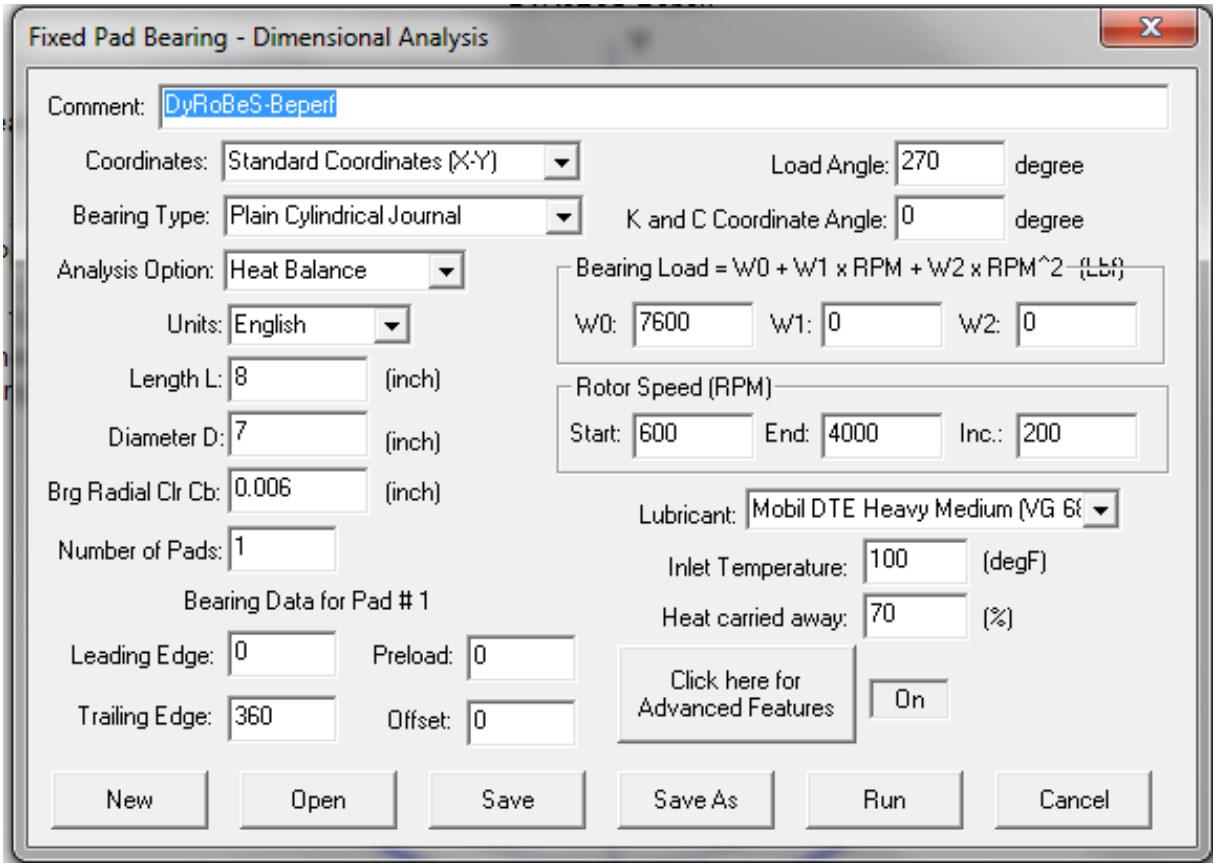

Figure 10 – Sleeve Bearing DyRoBeS© Dimensional Analysis Screen

The lubricant used in this study is Mobil DTE Heavy Medium, an ISO viscosity grade 68 lubricant which is commonly used in large industrial equipment. The forced lubrication oil system provides oil at 100°F to the bearings, so this was chosen as the inlet temperature. The bearing load is calculated to be

half the overall rotor mass of 15,200 lbm, which creates a force of 15,200 lbf that is supported by two bearings. Therefore, each bearing supports a load of 7600 lbf. The load angle is measured circumferentially counter clockwise from the positive x-axis to the negative y-axis, which is 270°. With these inputs, the bearing model was analyzed from 600 RPM to 4000 RPM in increments of 200 RPM, which covers the entire operational span of the rotor system, which operates at 3600 RPM. For operation between the increments, a linearly interpolated value is calculated.

After running the finite element analysis, DyRoBeS© presents an output file which presents the bearing operating characteristics at each speed increment. This output file is presented in Appendix V for both sleeve and pressure dam bearings. The graphical presentation will be shown in the following pages. As the bearing comes up to operating speed, the rotor eccentricity slowly decreases as the rotor equilibrium locus reaches the center of the locus, as Figures 11 and 12 show.

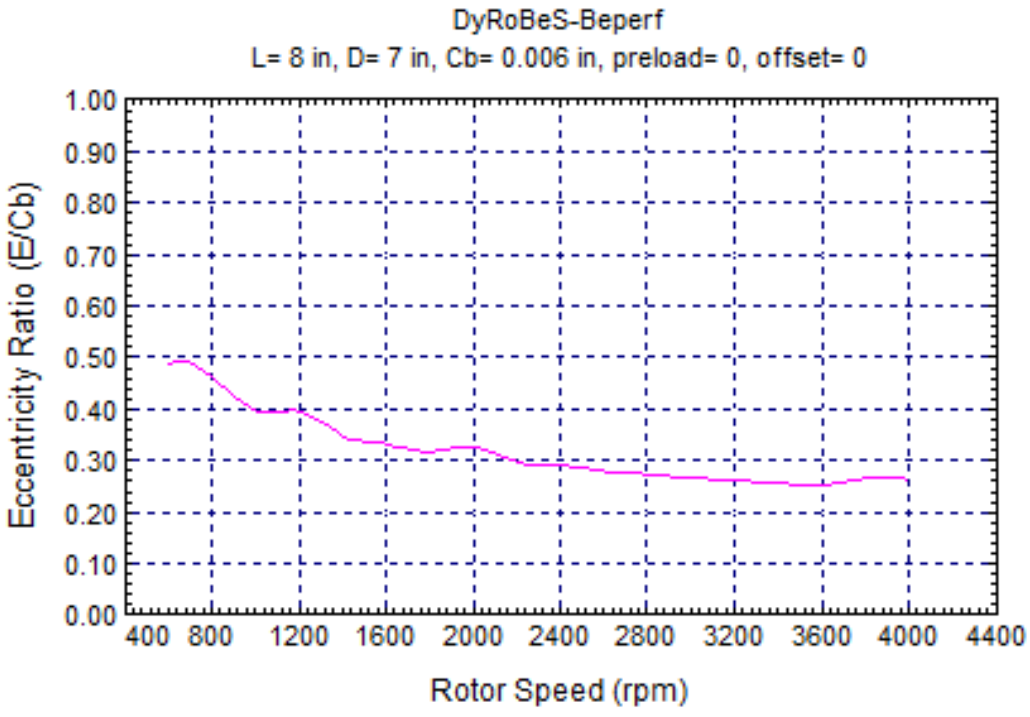

Figure 11 – Sleeve Bearing Journal Eccentricity Ratio

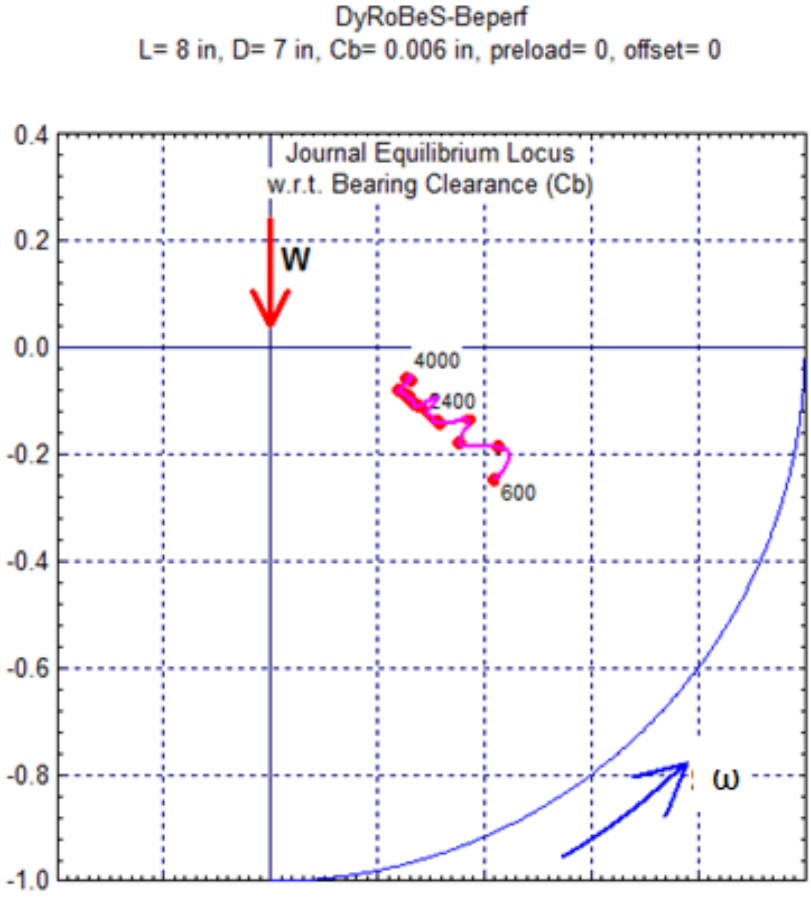

Figure 12 – Sleeve Bearing Journal Equilibrium Locus

As the bearing speed increases, the eccentricity of the bearing decreases and the overall film thickness increases, leading to the make up flow of oil required to maintain the full pressure film is increased. At the operating speed of 3600 RPM, a makeup flow of 3.25 gpm is required. The operating temperature of the oil steadily increases as the journal speed increases. The operating temperature range of the bearing is shown in Figure 13. The expected operating range of the bearing at operating speed is around 160°F.

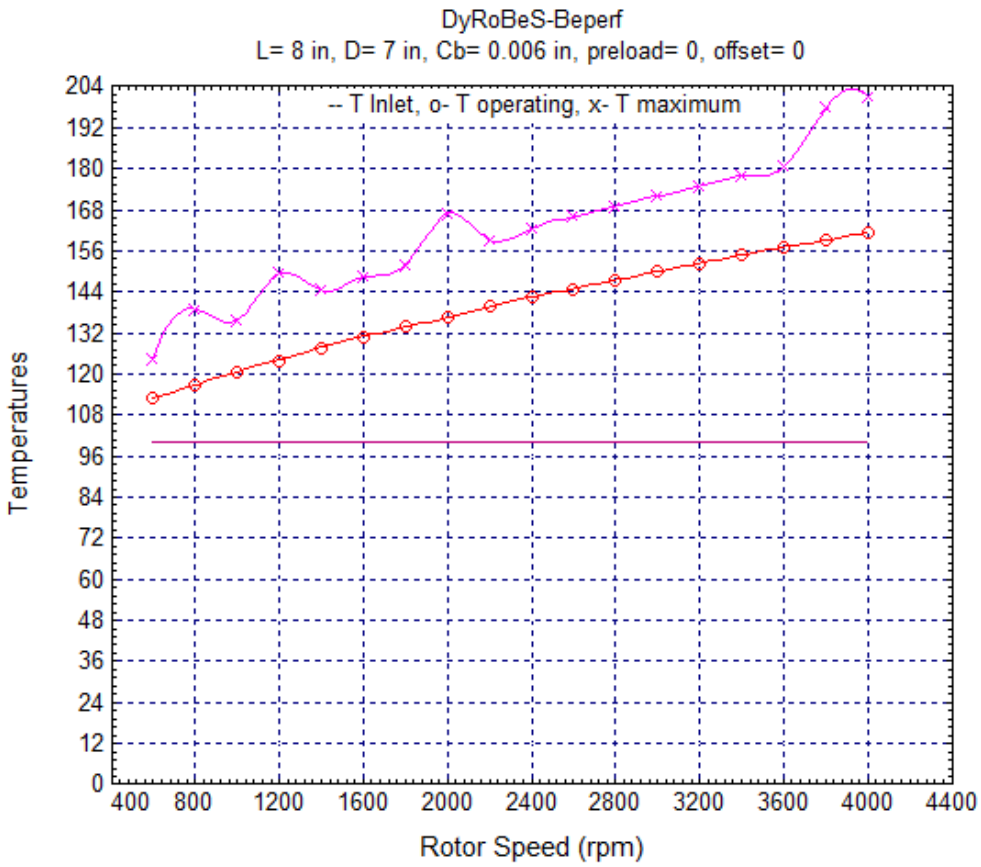

Figure 13 – Temperature Range of Sleeve Bearing

Maximum operating temperature is around 205°F. For this application, keeping the bearing operating temperature less than 250°F is desireable due to the corresponding reduction in oil viscosity. This reduction in viscosity correspondingly reduces film thickness and can lead to bearing damage.

With the given viscosity, eccentricity, and load detailed as shown in prior figures, the pressure profile in the bearing can be detailed. DyRoBeS© offers two individual outputs to depict the pressure profile in the bearing, a two dimensional bearing centerline pressure profile and a three dimensional pressure profile which depicts the bearing as if the cylindrical bearing were rolled onto a flat surface. The respective pressure profiles for the given system at operating speed of 3600 are given below in Figures 14 and 15.

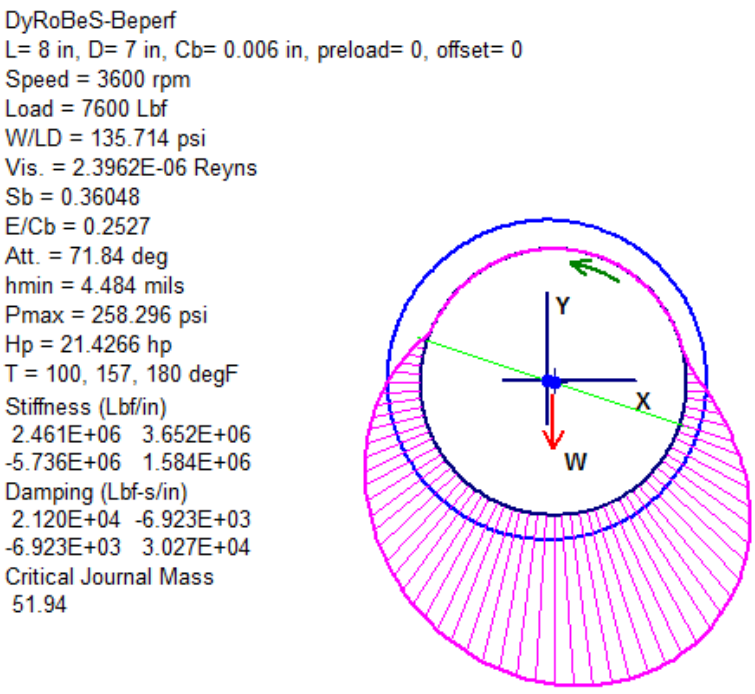

Figure 14 – Sleeve Bearing Pressure Profile at Centerline

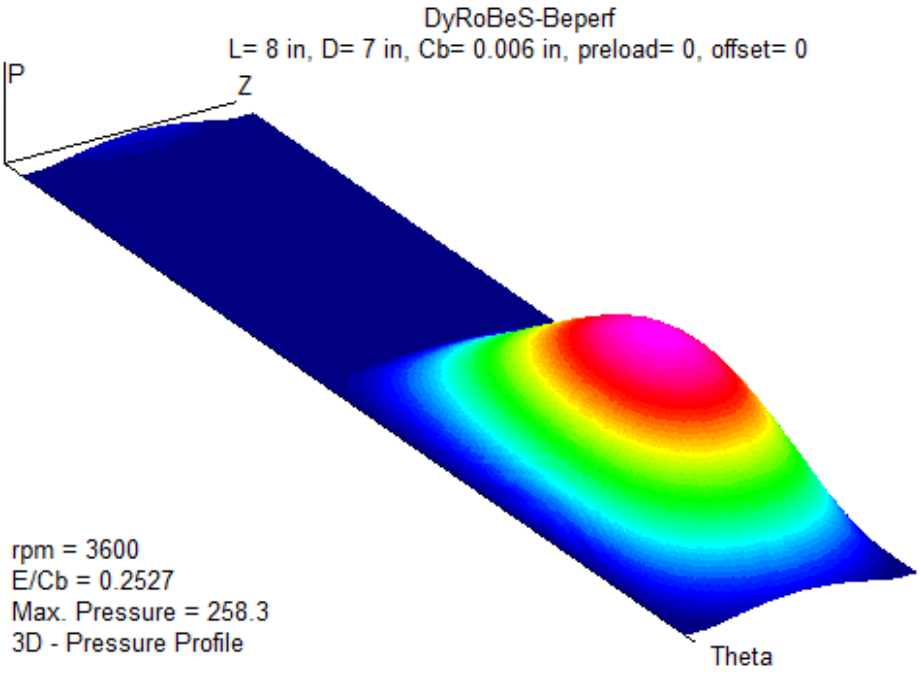

Figure 15 – Sleeve Bearing 3D Pressure Profile

Finally, the stiffness and damping coefficients for each speed increment is presented in Figure 16 for K_{xx}, K_{yy}, C_{xx}, and C_{yy} and Figure 17 for K_{xy}, K_{yx}, C_{xy}, and C_{yx}. These coefficients are exported to the DyRoBeS_Rotor© program as a .brg file for use in the finite element analysis of the rotor-bearing system. See Appendix V for the complete output file of the journal bearing. As shown in Figure 17, the cross coupled damping coefficients are the same. The uncoupled (also known as direct) stiffness and damping coefficients vary depending on the speed and do not appear to follow any specific trend.

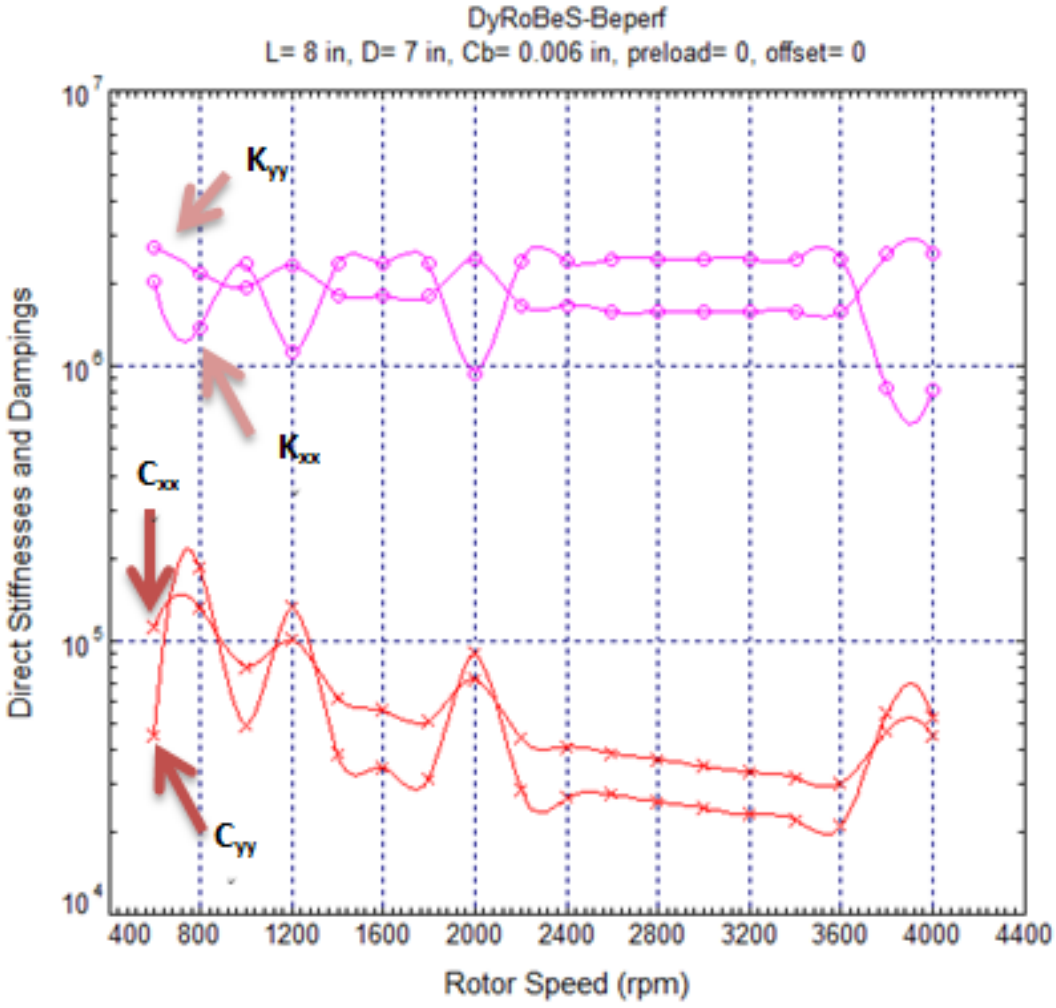

Figure 16 – Sleeve Bearing Kxx, Kyy, Cxx, and Cyy Coefficients

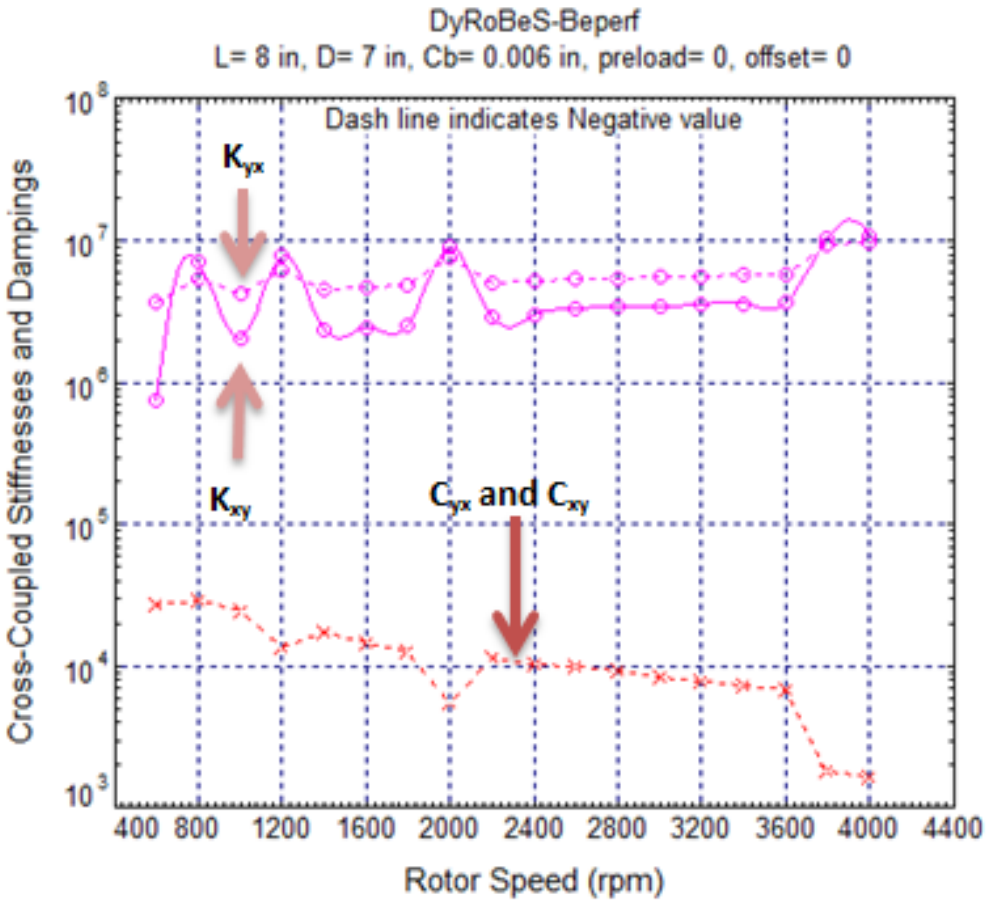

Figure 17 – Sleeve Bearing Kxy, Kyx, Cxy, and Cyx Coefficients

3.3 Pressure Dam Bearing Model

Pressure dam bearings, as discussed in Section 3.1, have a machined step in the upper half of the bearing which generate a hydrodynamically generated load. This load created by the step, or dam, induces a minimum eccentricity that stabilzes the rotor, working to prevent oil whirl and whip. The pressure dam bearing is generally intended for rotor-bearing systems with either high speeds or low loads. This effect is further enhanced by a circumferential relief track machined in the bottom half of the bearing which decreases the surface area which the load is spread, increasing the operating eccentricity of the rotor. The bearing is shown, viewing into the bearing axially, in Figure 18.

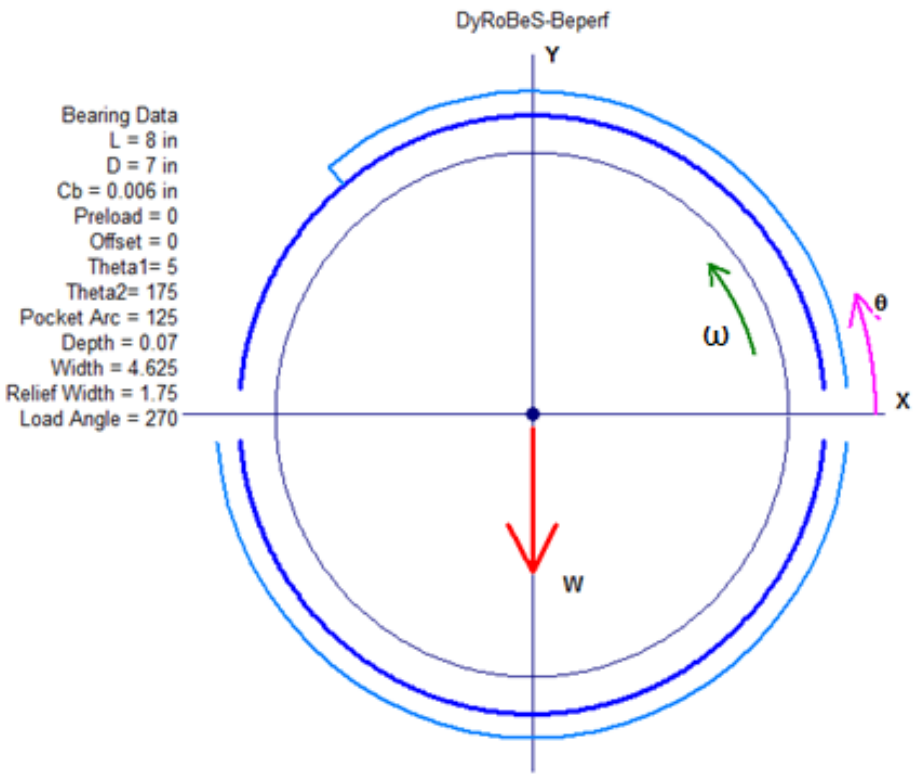

Figure 18 – Pressure Dam Bearing DyRoBeS© Screen

As with the sleeve bearing described in the previous section, the length of the pressure dam bearing eight inches, with a diameter of seven inches. The diametral clearance of the bearing is 12 mils, or 0.012 inches. The dam is machined into the upper half of the bearing at a depth of 0.07 inches 125° circumferentially counterclockwise from the centerline of the bearing. Machined centered at the axial centerline of the bearing, the width of the dam is 4.75 inches. The relief track machined on the bottom half of the bearing is centered at the axial centerline of the bearing and is 1.75 inches wide. The depth of the relief track, like the dam, is 0.07 inches.

A dimensional analysis was performed in DyRoBeS©, performing a heat balance with 70% of the given heat taken away by the lubricating oil as in the sleeve bearing analysis. The given lubricant was also Mobil DTE Heavy Medium and the specified load was 7600 lbf on the bearing. The rotor system was

modeled from 600 RPM to 4000 RPM in increments of 200 RPM. Figure 19 shows the DyRoBeS© input screen for the dimensional analysis with the heat balance. The advanced features button is used to define the width/length of the pressure dam and relief track.

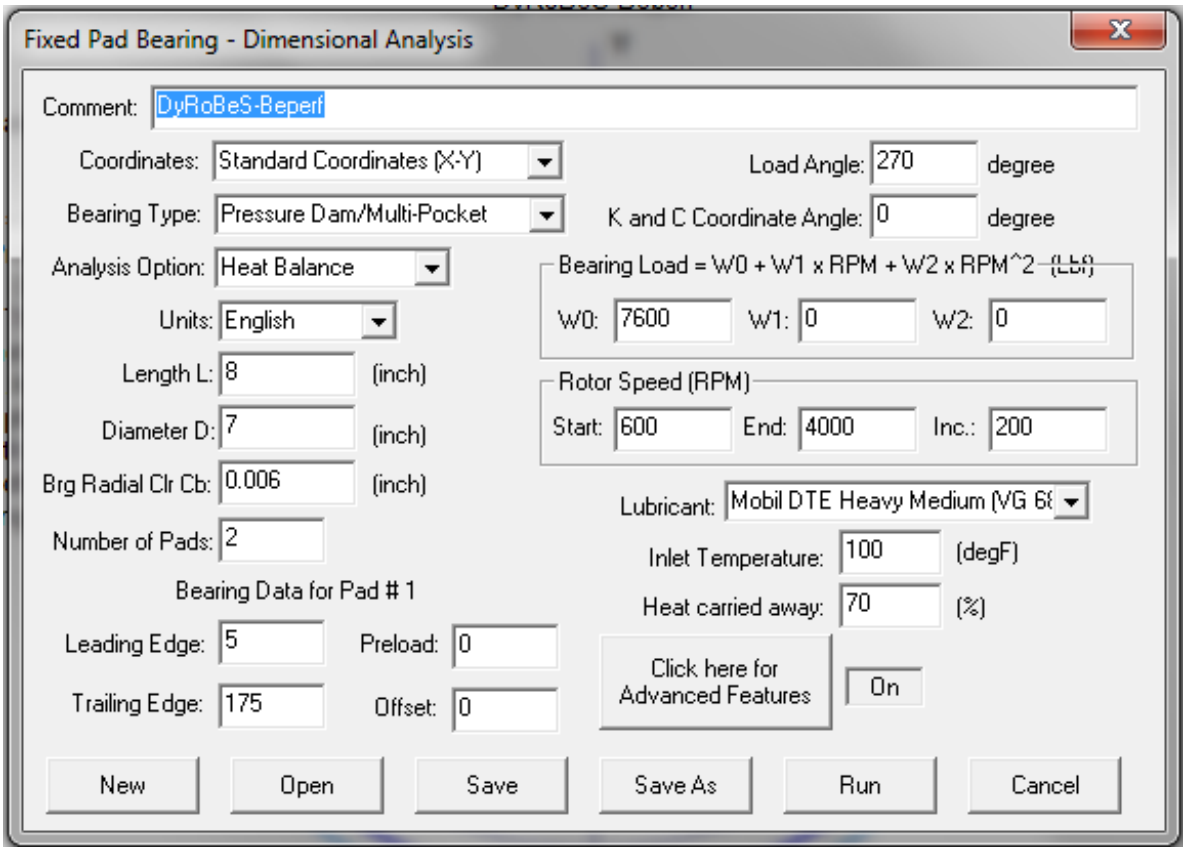

Figure 19 – Pressure Dam Bearing DyRoBeS© Dimensional Analysis Screen

Once again, the finite element analysis was performed and an output file was created by DyRoBeS© which was then exported as a .brg file for use with the DyRoBeS_Rotor© program. As was expected, the dam and relief track forces combined to prevent the journal from reaching a minimum eccentricity. The pressure dam bearing eccentricity ratio at operating speed is 0.62 compared to 0.25 for the journal bearing, as shown in Figure 20 and further exemplified by the journal equilibrium locus

shown in Figure 21, which is much further away from the bearing centerline than the sleeve bearing journal equilibrium locus shown in Figure 12.

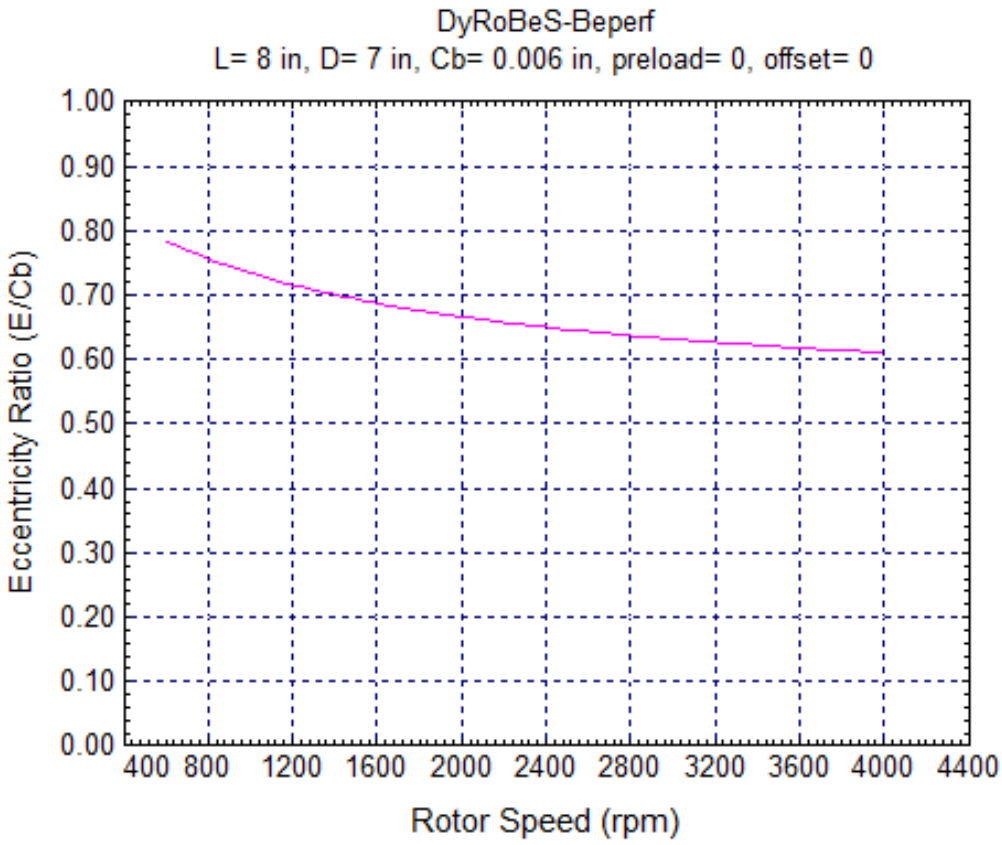

Figure 20 – Pressure Dam Bearing Journal Eccentricity Ratio

Since the pressure dam increases the eccentricity of the bearing, a greater oil flow is required to make up for that which leaks out the side to maintain full hydrodynamic lubrication. The pressure dam bearing requires 6.5 gpm of oil at the operating speed of 3600 RPM, which is double the amount of the sleeve bearing. Similarly, the increase in film thickness from the increased eccentricity ratio of the bearing leads to oil temperatures which are lower than that seen in the journal bearing. The operating temperature in Figure 22 at 3600 RPM is less than 140°F. Also, the maximum temperature is less than 200°F. The lower oil temperatures leads to higher viscosity oil, providing a stiffer bearing.

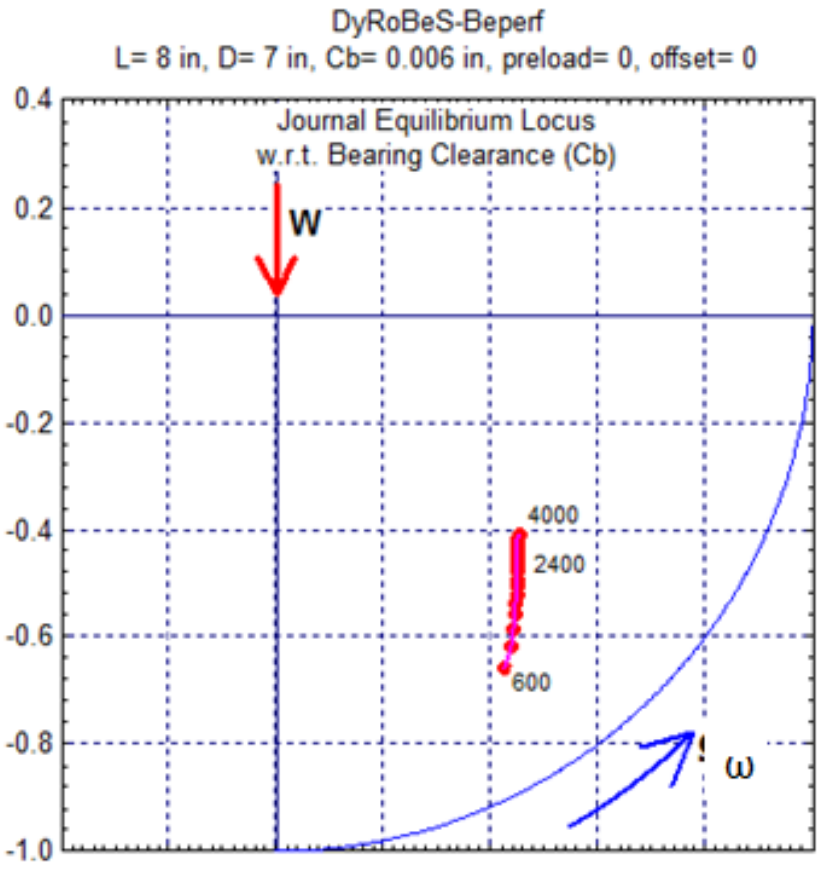

Figure 21 – Pressure Dam Bearing Journal Equilibrium Locus

The relief track in the bottom of the bearing reduces the overall surface area over which the load can be spread. This creates much higher pressures in the lower half of the bearing. Instead of a maximum pressure of 258.3 psi, the predicted maximum pressure in the pressure dam bearing is 591.4 psi, as shown in Figure 24. The dam acting on top of the bearing also creates a pressure force in the upper half of the bearing that is not seen in the sleeve bearing. This effect is shown in the two dimensional pressure profile of the aforementioned Figure 23 and three-dimensionally in Figure 24.

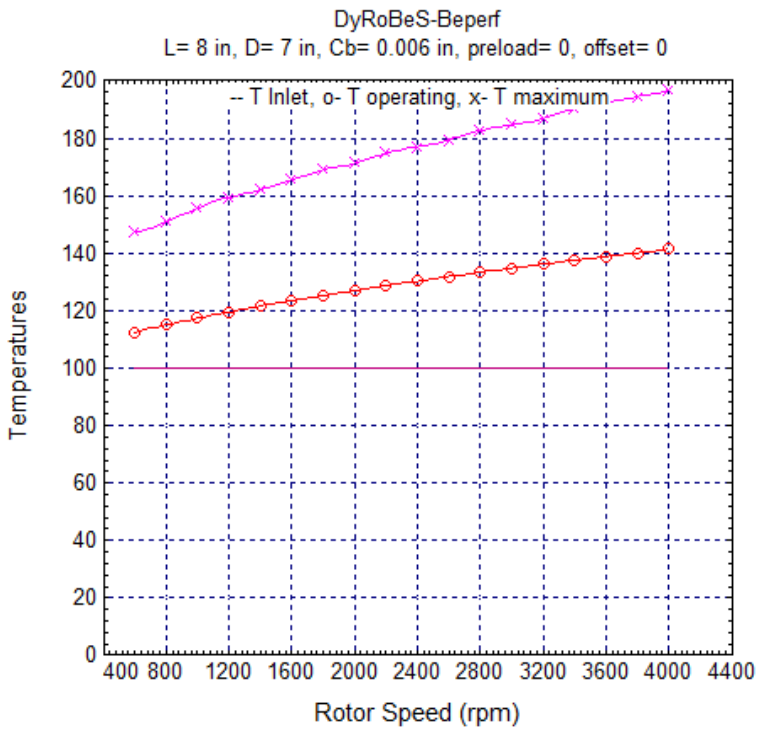

Figure 22 – Temperature Range of Pressure Dam Bearing

DyRoBeS-Beperf
L= 8 in, D= 7 in, Cb= 0.006 in, preload= 0, offset= 0
Speed = 3600 rpm
Load = 7600 Lbf
W/LD = 135.714 psi
Vis. = 3.4518E-06 Reyns
Sb = 0.51929
E/Cb = 0.6179
Att. = 46.97 deg
hmin = 2.293 mils
Pmax = 591.641 psi
Hp = 28.767 hp
T = 100, 138, 192 degF
Stiffness (Lbf/in)
3.032E+06 5.136E+05
-6.011E+06 5.404E+06
Damping (Lbf-s/in)
9.727E+03 -8.951E+03
-8.949E+03 2.702E+04
Critical Journal Mass
80.3

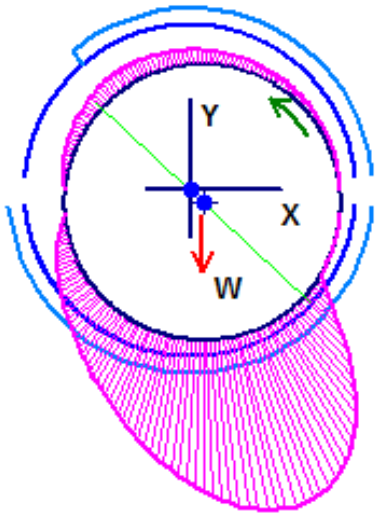

Figure 23 – Pressure Dam Bearing Pressure Profile at Centerline

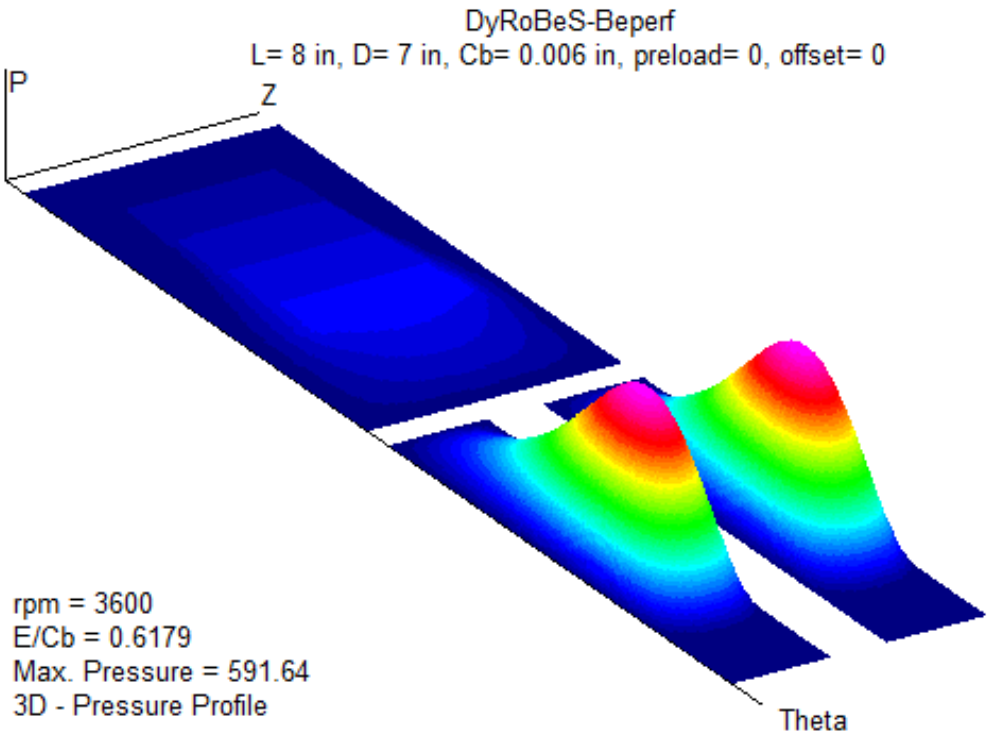

Figure 24 – Pressure Dam Bearing 3D Pressure Profile

The given stiffness and damping coefficients for each speed increment is presented in Figure 25 for K_{xx}, K_{yy}, C_{xx}, and C_{yy} and Figure 26 for K_{xy}, K_{yx}, C_{xy}, and C_{yx}. As with the sleeve bearing, these coefficients are exported to the DyRoBeS_Rotor© program as a .brg file for use in the finite element analysis of the rotor-bearing system. See Appendix V for the complete output file of the pressure dam bearing, as well as the sleeve bearing.

From Figures 25 and 26, it can be seen that the uncoupled (direct) stiffness and damping coefficients for the pressure dam bearings are in the same order of magnitude as the sleeve bearings. The cross-coupled stiffness coefficients are considerably different for the pressure dam bearing. The cross-coupled damping coefficients at lower speeds are of a similar order of magnitude for each bearing type, but as the speed increases the sleeve bearings cross coupled damping coefficients decrease. The stiffness coefficient K_{xy} is also considerably different for each bearing.

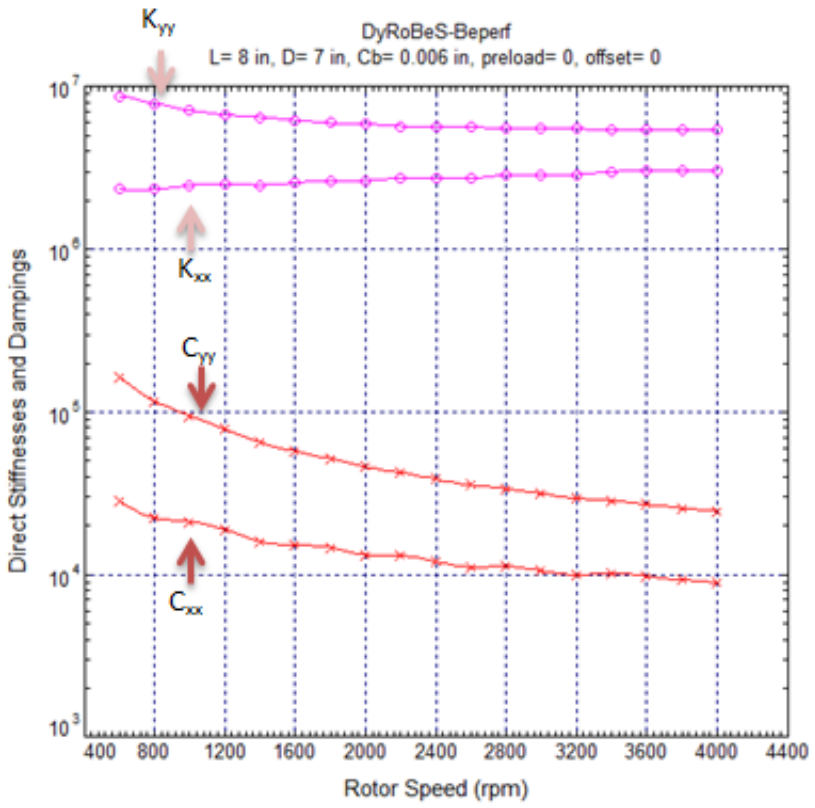

Figure 25 – Pressure Dam Bearing Kxx, Kyy, Cxx, and Cyy Coefficients

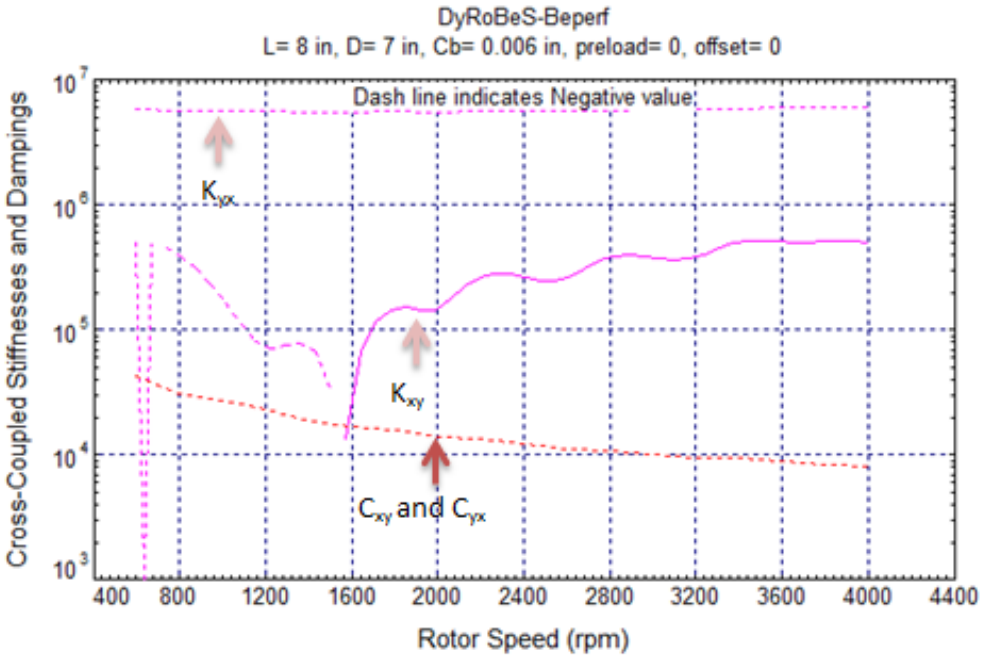

Figure 26 – Pressure Dam Bearing Kxy, Kyx, Cxy, and Cyx Coefficients

With the finite element analysis performed for each bearing, the bearing performance coefficients in terms of damping and stiffness can be exported to the DyRoBeS© rotor-bearing software for the complete rotor-bearing system performance. The next three sections of this chapter will describe the rotor model with the individual bearing results. Section 3.4 will present the rotor model. Sections 3.5 and 3.6 will present the results of the rotor-bearing system simulation.

3.4 Rotor-Bearing Model

If beginning a rotating system design and analysis from scratch, then it is vital to consider the rotating equipment first and then size the bearings correspondingly. For the problem at hand, because the bearing load, rotating speed, and bearing size were known, the bearing coefficients could be calculated first and then implemented into the overall system design. This section will present the steps to modeling the rotor with the bearings and performing the lateral rotordynamic analysis. This analysis will predict the location of the various critical speeds and determine the amount of vibration expected in the rotor-bearing system with each bearing type. Lateral rotordynamic analyses provide the user with information on critical speeds, mode shapes, forced responses, and rotor-bearing stability. Because DyRoBeS© uses finite elements, a finite element approach to the rotor-bearing analysis will be presented.

Rotor systems consist of three primary components: the rotating assemblies, non-rotating flexible supports, and massless interconnection components such as bearings that provide interacting forces between components. Finite element stations are numbered consecutively from left to right on the shaft, as shown in Figure 27. Each element can consist of several subelements, allowing for geoemetric discontinuities. While each station can consist of multiple subelements, any bearings or seals must be located at the finite element station. The degrees of freedom of the finite element station are considered “master” degrees of freedom.

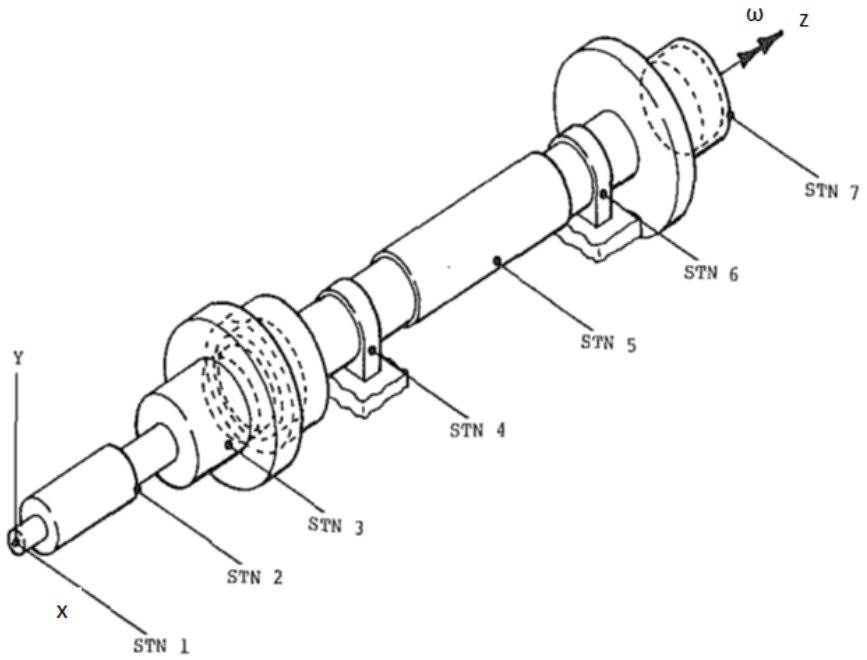

Figure 27 – Typical Rotor-Bearing Finite Element Assembly [36]

When the equations of motion of the rotor are assembled, these are kept while the degrees of freedom of the internal subelements are condensed out prior to the assembly process [14]. Once the displacements at the "master" stations have been found,then the displacements of the subelements can be calculated. Per the API standard [13], maintaining a length-to-diameter ratio of less than 1.0 and greater than 0.1 is preferred for each element for computational accuracy, with an L/D of 0.5 preferred for these analyses.

Each element is homogenous, with distributed mass and elasticity. The lateral motion of the element is described by two translational and two rotational displacements, x, y, θ_x, and θ_y. Each displacement is a function of spatial coordinates, s, and time, t. The finite element analysis thus reduces the governing partial differential equations with infinite degrees of freedom to ordinary differential

equations with discrete, finite degrees of freedom. Each element can be expressed by eight end-point displacements by specifying a spatial shape function shown by,

$$\begin{Bmatrix} x(s,t) \\ y(s,t) \\ \theta_x(s,t) \\ \theta_y(s,t) \end{Bmatrix} = \begin{bmatrix} \boldsymbol{\Psi}_T(s) \\ \boldsymbol{\Psi}_R(s) \end{bmatrix}_{4x8} \boldsymbol{q}^e(t)_{8x1} \tag{3.1}$$

where

$$\boldsymbol{q}^e = \left(x_1, y_1, \theta_{x1}, \theta_{y1} \middle| x_2, y_2, \theta_{x2}, \theta_{y2}\right)^T \tag{3.2}$$

The primary source of these equations is the work of Chen and Gunter [14], as they have presented the mathematical background of the DyRoBeS© program. In this instance, **q** is the time-dependent end point displacement vector. The shape function matrices, $\boldsymbol{\Psi}_T$ and $\boldsymbol{\Psi}_R$, are established by beam elasticity theory. For further explanation and solution of these equations, reference Appendix III.

Using this background, the DyRoBeS© rotor model was built which allowed the various bearing tests to be implemented. Using rotor manufacturing drawings, the rotor was converted into finite element stations and implemented input into the DyRoBeS© program. The finalized model consists of 32 elements covering the entire length of the rotor. Disks were added to the rotor to simulate the rotor couplings, cooling fans, centering rings, and retaining rings. Bearings were located at the each requisite station on the rotor. The resultant rotor finite element model is shown in Figure 28.

The resulting rotor model length is within one thousandth of an inch of the actual measured length of the rotor. The rotor weight was matched to the measured weight of the rotor plus the given weight of the couplings. In order to accomplish this, steel density, modulus of elasticity,and shear modulus were used for each station's properties except the motor core stations containing the copper windings and end windings. For these stations, an equivalent density was used to match the weight of

the rotor containing the windings. For these stations, the stiffness of the windings were considered neglible, as per API code 684, Section 2.8.2. [13]. Therefore, carbon steel properties of modulus of elasticity and shear modulus were used for the motor core. For carbon steel, the modulus of elasticity is 2.9×10^7 psi while the shear modulus is 1.1154×10^7 psi. The density of steel, 0.283 lbm/in^3, was used for the rotor pieces shown in blue in Figure 28. The equivalent density, 0.17 lbm/in^3, was used for the motor core depicted in green in Figure 28.

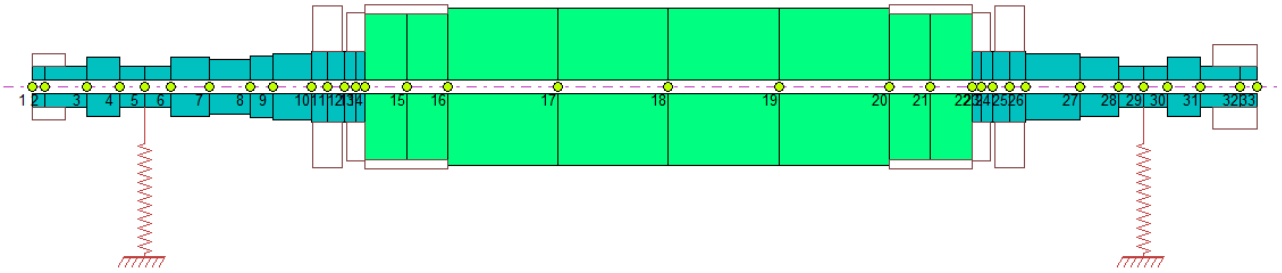

Figure 28 – DyRoBeS© Rotor Model

Per the API standard [13], the length to diameter ratio of each finite element was ensured to be less than 1.0 and greater than 0.1 to ensure the model contains sufficient resolution for calculating rotor properties such as critical speeds while also preventing numerical errors that can occur between adjacent elements with large length differentials. A 2.5” diameter bore through the rotor was included, which was originally used for periscope inspection of the rotor forging during rotor construction. Seven individual disks were used in the modeling of the rotor. At the rotor ends, the two coupling disks were modeled using coupling manufacturer drawings. Each end supports half the weight of the coupling assembly. The moments of inertia were taken from the drawings.

Viewing the rotor in Figure 28 from left to right, the disks containing the cooling fan, centering ring, and retaining ring are located to the left and right of the motor core. Each disk was sized using

manufacturer drawings and lumped masses/inertias were added to these stations. An undamped critical speed analysis was performed to determine how near the rotor was to the respective critical speeds depending on varying bearing stiffness. Figure 29 shows the critical speed map of the rotor. Each line represents another natural frequency of the rotor depending on the bearing frequency. The blue line represents the operational speed of the rotor, 3600 RPM.

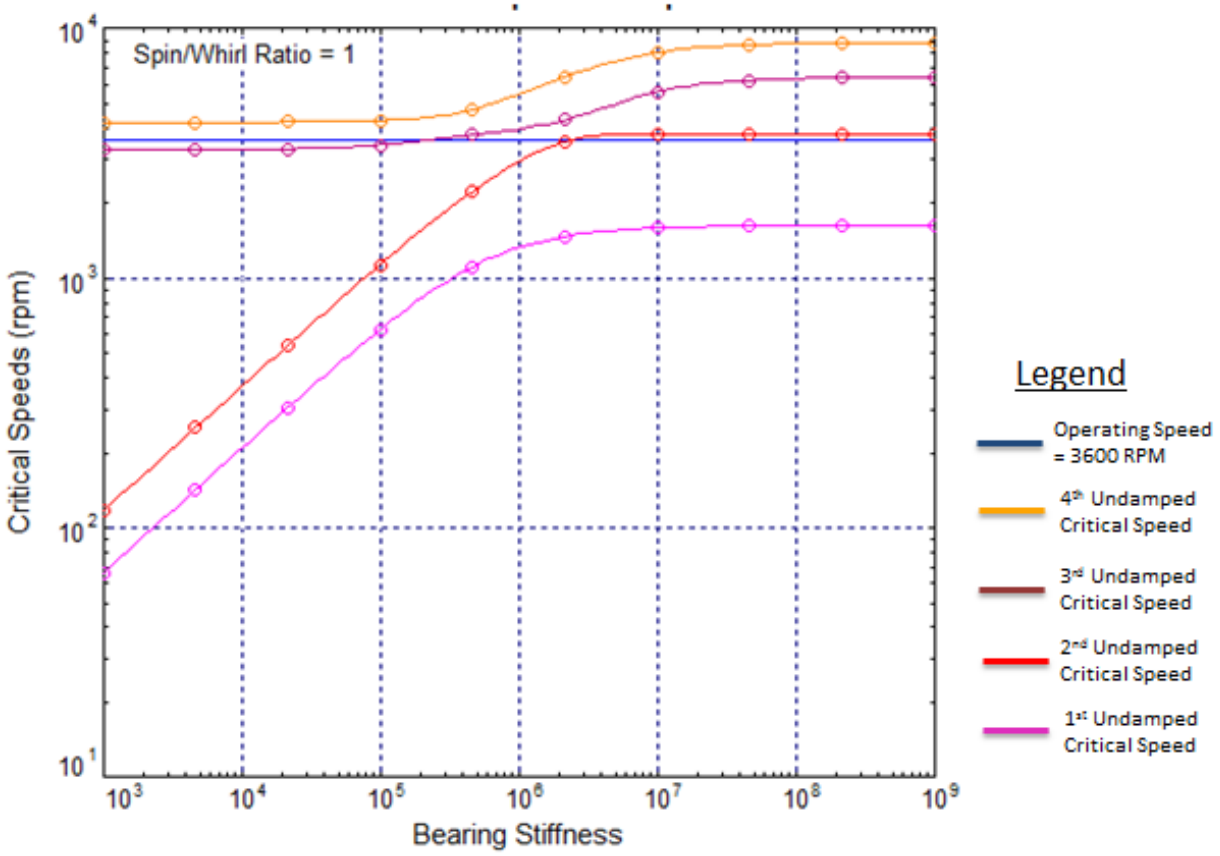

Figure 29 – Undamped Critical Speed Map

Referencing the bearing stiffnesses from Figures 16 and 25, from the map the rotor should pass through at least one critical speed while running up to operational speed. The second critical speed appears to be extremely close to operational speed for bearings with a stiffness range of 10^6 to 10^7, as

both of the bearing models indicate. This critical speed map indicates that reducing the bearing stiffness will lower the second critical below operational speed, but the third critical speed would shift towards the operational speed at that point. Since these results are inconclusive, other analyses were performed with the individual bearing models. The bearing coefficients were imported from the bearing performance software of DyRoBeS© to the rotor analysis software. Using the pressure dam bearing properties, various simulations of the rotor-bearing dynamic behavior were performed, as seen in the following section.

3.5 Rotor Model with Pressure Dam Bearings

Using the bearing coefficients determined in Section 3.3, several rotordynamic analyses were performed including critical speed analyses, stability analyses, and steady state response analyses. The critical speeds were analyzed to determine the energy distribution of each mode shape, allowing for an estimation of which part of the rotor is the predominant one in influencing that critical speed (rotor natural frequency). For the first bending mode, using an averaged bearing stiffness the calculated critical speed occurs at 1547 RPM, as seen in Figures 30, 31, and 32. Figures 31 and 32 show the potential and kinetic energy distribution of this mode shape.

Because the potential energy of the mode shape is over 70% shaft energy, the mode is considered a flexible rotor mode [14], as seen in Figure 31. From Figure 32, the “T” energy represents the kinetic energy from mass translational motion. “R” energy represents the kinetic energy due to rotary inertia. “G” energy represents the kinetic energy due to gyroscopic moment. As was the case with the potential energy, the kinetic energy is dominated by the shaft energy, as 69.41% of the overall system kinetic energy is from the shaft.

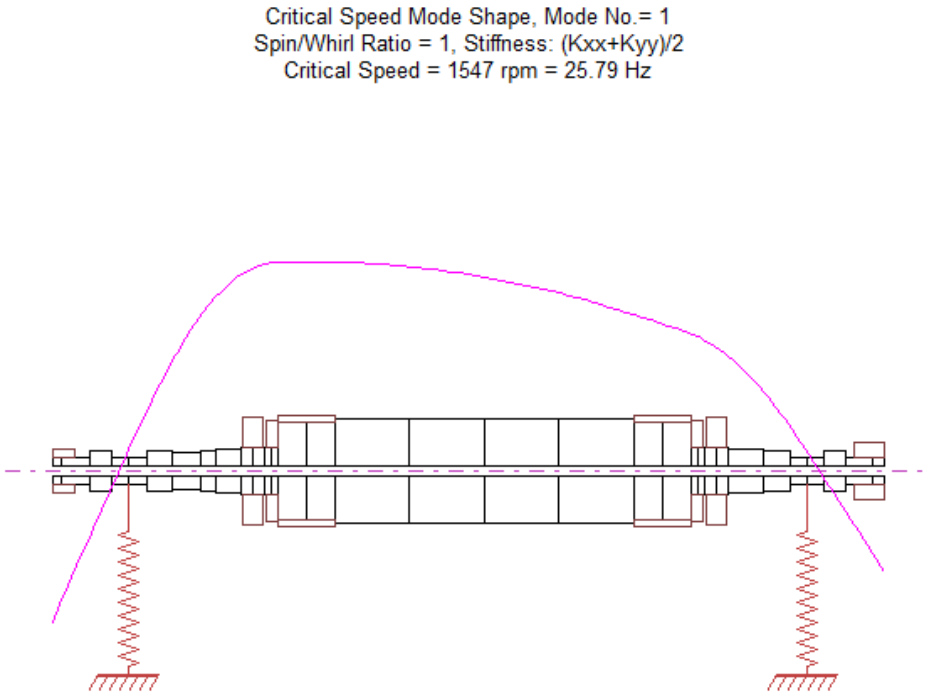

Figure 30 – Rotor-Pressure Dam Bearing Model Mode No. 1

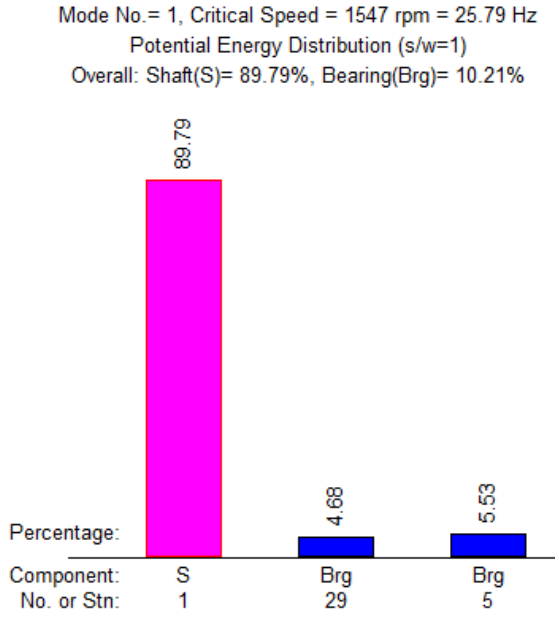

Figure 31 – Rotor-Pressure Dam Bearing Model Mode Shape No. 1 Potential Energy Distribution

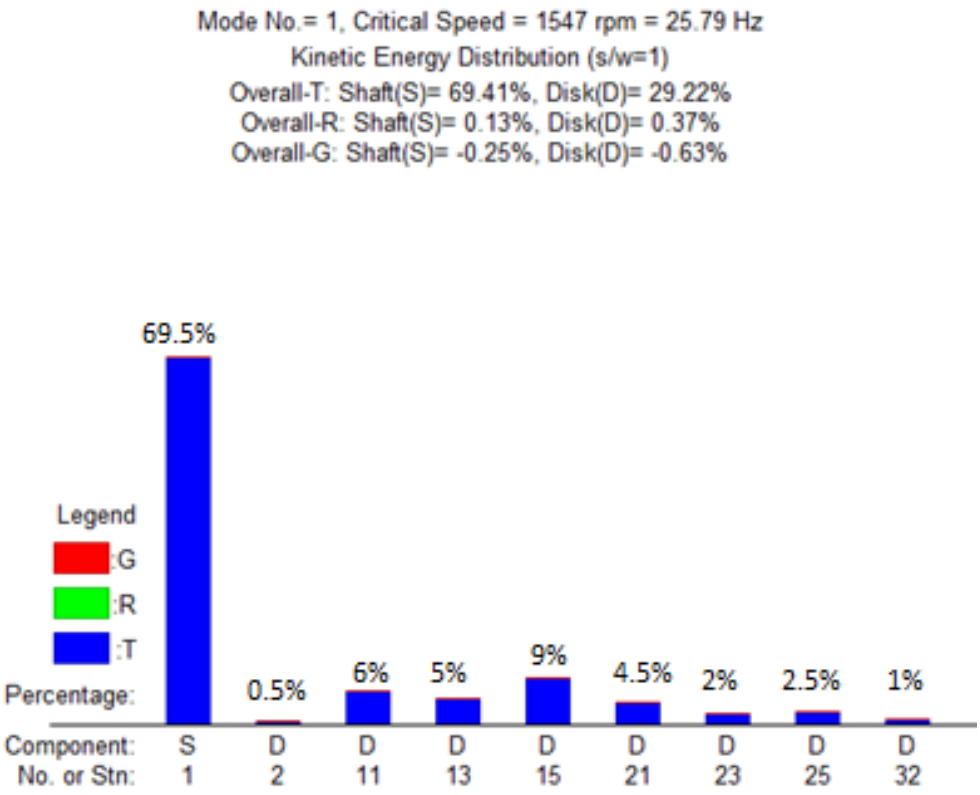

Figure 32 – Rotor-Pressure Dam Bearing Model Mode Shape No. 1 Kinetic Energy Distribution

The next critical speed appears at 3708 RPM, just 100 RPM and just over 3% away from the operational speed of 3600 RPM, as shown in Figure 33. Typically, most designs operate over 10% away from the critical speed, so this mode may infringe on the operation of the motor. This mode is considered the second bending mode. As can be seen in Figures 34 and 35, this mode is a flexible rotor mode that is dominated by the shaft energy and the coupling located on the right end of the shaft as shown in Figure 28. As can be seen by the Overall-G of Figure 35, the gyroscopic kinetic energy (G) is negative. This ultimately results in the gyroscopic effect raising the natural frequency of the rotor, i.e. increasing the critical speed of the rotor. Inertial (R) energy as seen in Figure 35, can lower the critical speed [14]. The coupling contributes the greatest percentage of inertial and gyroscopic energy, with the gyroscopic energy having a larger percentage of the kinetic energy than the inertial effects.

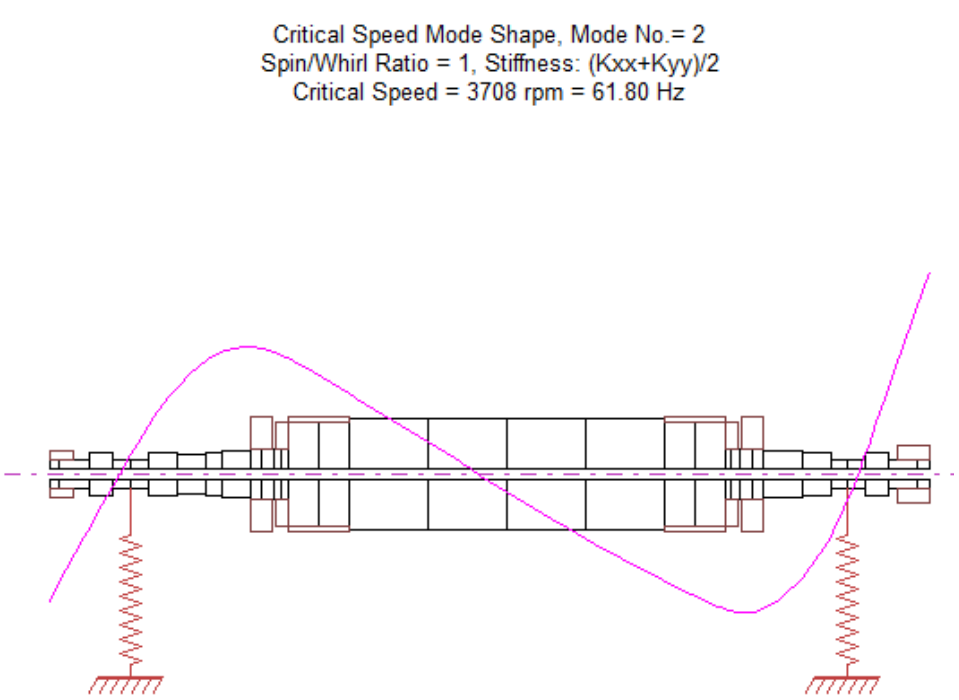

Figure 33 – Rotor- Pressure Dam Bearing Model Mode No. 2

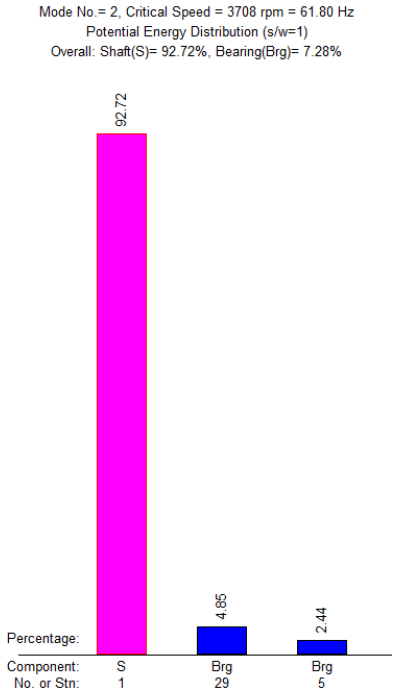

Figure 34 – Rotor- Pressure Dam Bearing Model Mode Shape No. 2 Potential Energy Distribution

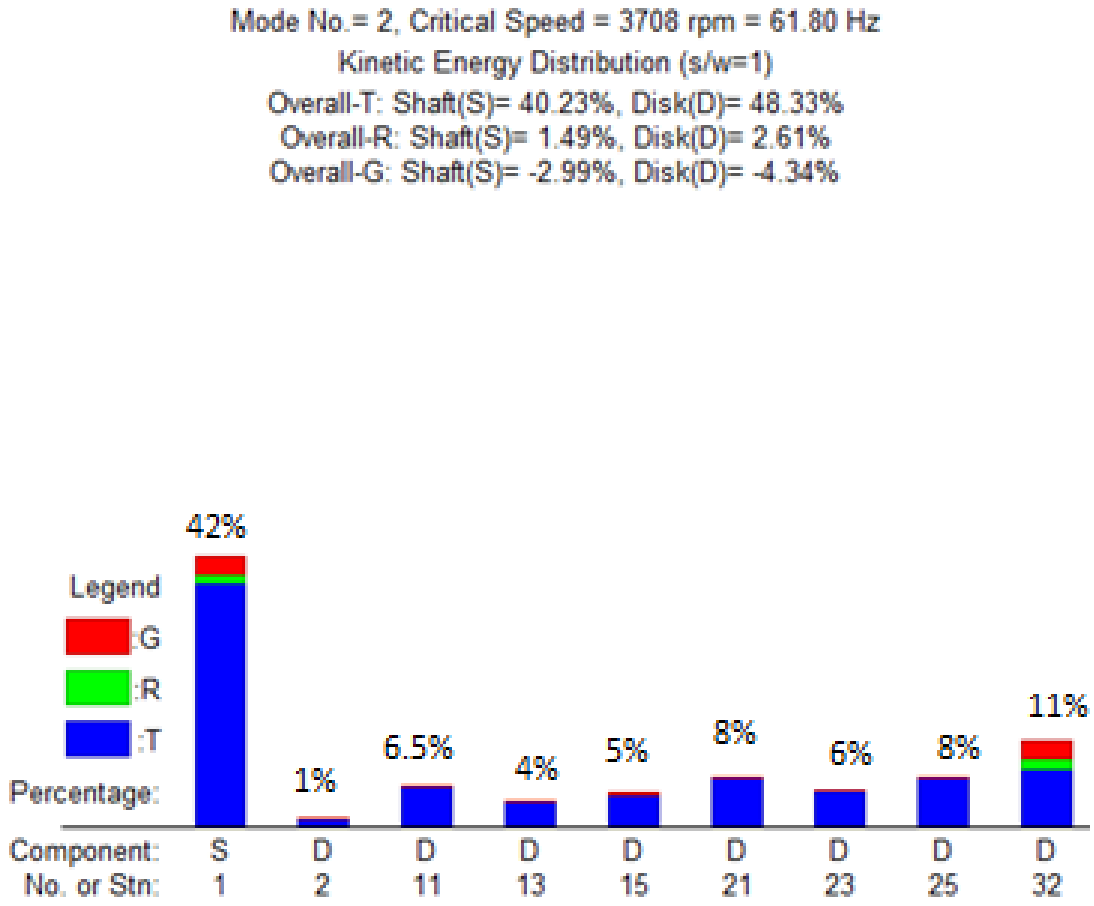

Figure 35 – Rotor-Pressure Dam Bearing Model Mode Shape No. 2 Kinetic Energy Distribution

The next two critical speeds occur at 4914 RPM and 7269 RPM, well above the rotor operational speed. These modes will not be considered. A whirl speed and stability analysis was ran for the rotor-bearing model from a speed of 600 RPM to 5000 RPM. As can be seen in Figure 36, the rotor experiences multiple natural frequencies as it comes up to speed. Fortunately, many of these frequencies do not effect the operation of the rotor and are the result of backwards precessional motion or are significantly damped and nearly undetectable, as will be seen.

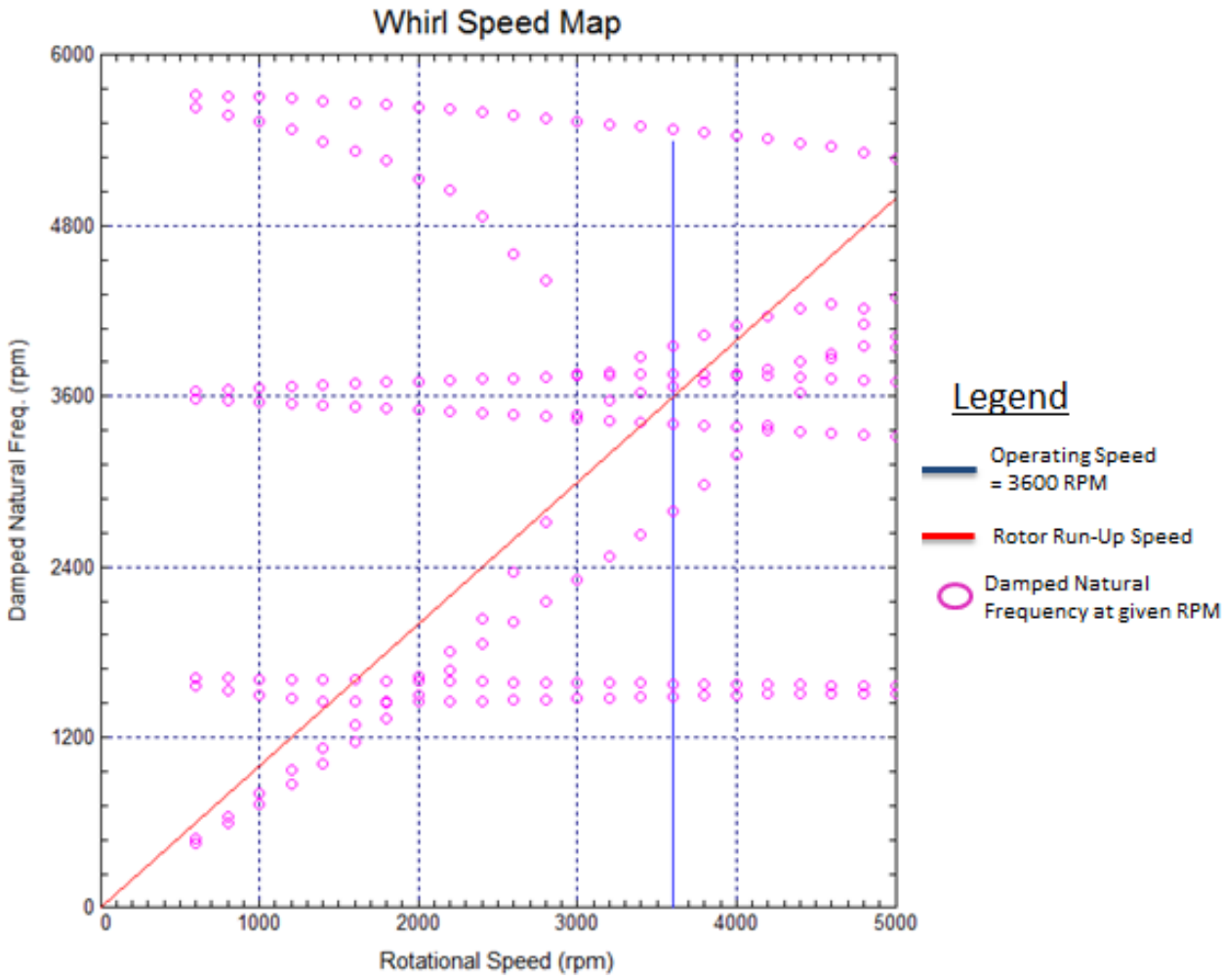

Figure 36 – Rotor-Pressure Dam Bearing Model Whirl Speed Map

Backwards precessional motion is motion in the reverse direction of shaft rotation. In most rotordynamic analyses, only the forward precessional modes are considered for potential synchronous excitation [61]. These forward excitations are created by the unbalance force which contains a vector in the direction of the rotation. While studies have investigated the excitation of backward modes, this study will simply take into account the modes predominated by forward precessional motion.

Another piece in determining which mode shapes are truly important is the log decrement calculation. The log decrement, shown in Equation 3.3, uses the calculated damping of the rotor mode to provide an indication for whether the rotor mode is stable.

$$\delta = \frac{2\pi\zeta}{\sqrt{1-\zeta^2}} \tag{3.3}$$

If this log decrement is greater than 0, then the mode is stable. Modes with log decrement values which are much greater than 0 may not be seen when the rotor is operating, as they are fully damped. Any log decrement value above unity can be considered well damped. Values of the log decrement that are close to 0 or less than 0 are neutrally stable and unstable, respectively. Figure 37 depicts the first six modes of the rotor.

While these six natural frequencies will be passed as the rotor comes to operational speed, only two are expected to be excited such that operation of the rotor is affected. The first rotor mode, occurring at 1491 RPM, is the expected first critical speed. This mode is predominantly forward precessional motion dominated, at 93% forward and 6% backward. Any rotor unbalance will be excited by this natural frequency, and because the log decrement is equal to 0.0154, which is extremely low, this critical speed is not well damped. Mode2 is not expected to be impactful because it is primarily a backwards precessional mode. Mode 3 is highly damped, with a log decrement value of 5.8814, so it should not impact rotor operation. Mode 4 is also primarily a backwards precessional mode and is not expected to be an issue.

While these six natural frequencies will be passed as the rotor comes to operational speed, only two are expected to be excited such that operation of the rotor is affected. The first rotor mode, occurring at 1491 RPM, is the expected first critical speed. This mode is predominantly forward precessional motion dominated, at 93% forward and 6% backward. Any rotor unbalance will be excited

by this natural frequency, and because the log decrement is equal to 0.0154, which is extremely low, this critical speed is not well damped. Mode 2 is not expected to be impactful because it is primarily a backwards precessional mode. Mode 3 is highly damped, with a log decrement value of 5.8814, so it should not impact rotor operation. Mode 4 is also primarily a backwards precessional mode and is not expected to be an issue.

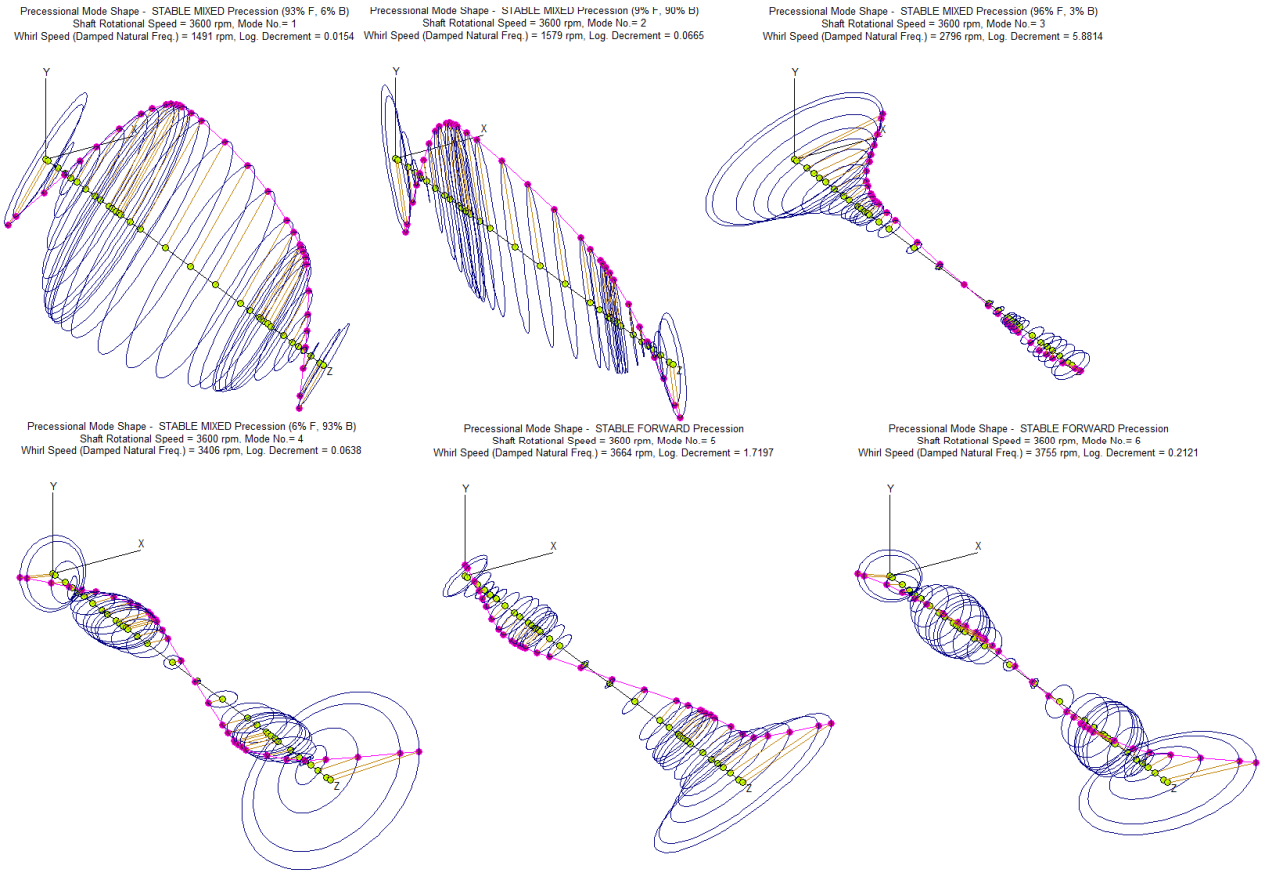

Figure 37 – Rotor-Pressure Dam Bearing Model Precessional Mode Shapes

The next two modes, 5 and 6, are stable forward precessional modes. These modes occur at 3664 and 3755 RPM, respectively, and contain log decrement values of 1.7197 and 0.2121. These calculated values lead to the belief that a 2nd critical speed should occur somewhere above 3600 RPM

just above the operational speed of the rotor. This is close enough to the rotor speed that these natural frequencies may amplify rotor vibration at operational speed. Because mode 6 is less damped, this mode has the most impact on the rotor operation. In order to study this impact, an unbalance response analysis was performed for mode 1 and mode 6.

Using the API procedure as laid out in API RP 684 SP6.8.2 [13], unbalances were placed at the location which exacerbated the mode effects and provided maximum displacement, as taken from SP-3 from the API standard and reproduced in Figure 38. For Mode 1, 70.2 oz-in of unbalance was placed at Station 18 as shown in Figure 28. The linear steady state response of the unbalance was run to 125% operational speed, or 4600 RPM. The effects were then plotted on Bode plots which simulate the bearing proximity probe location readings. The resulting Bode plot is shown in Figure 40 for Mode No. 1. This Bode plot indicates a first critical between 1400-1600 RPM and a second critical between 3600-4000 RPM. Using the corrected amplitude values shown in SP6.8.2.11 of API 684 [13], the amplitudes of the vibration do not appear to exceed the 12 mils of clearance in the bearings. However, operation of the rotor appears to be infringing on the second critical which can lead to unpredictable responses. Calculating the unbalance response for Mode 6 will help get an idea of the effects of running near the second critical speed, as will be seen in Figure 41.

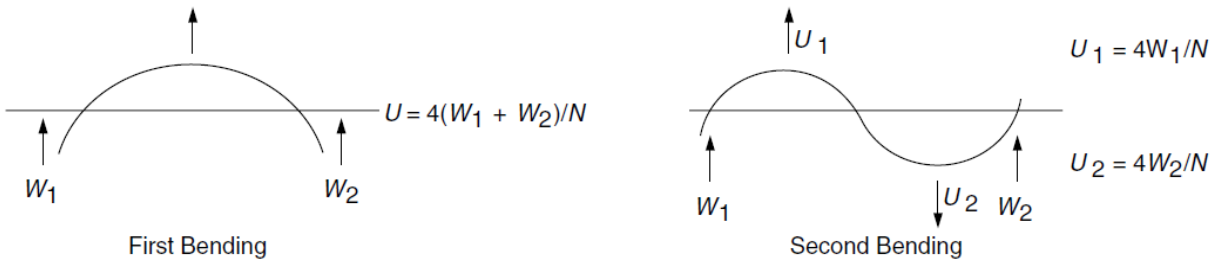

Figure 38 – Unbalance Locations from API 684

For amplifying Mode 6, unbalances of 35.08 oz-in were added to Stations 13 and 24, 180° apart. From Figure 41, adding unbalance at the locations depicted in Figure 38 increased the vibration amplitude of the second critical to 5.9 mils p-p vibration at the EN vibration probe. This effect shows that any unbalance in the end winding/cooling fan location of the rotor can increase the amplitude of the rotor vibration considerably. Since the rotor operational speed is infringing on this second critical speed, balance of the rotor at the centering ring plane is important in ensuring smooth rotor operation. Please note that on the given Bode plots shown in Figures 40 and 41, the location of the vibration measurements are given by the west north (WN), west south (WS), east north (EN), and east south (ES) proximity probes located at the bearings. The west bearing is located on the left of Figure 28 at Station 5. The east bearing is located on the right of Figure 28 at Station 29. Please note that the north proximity probes, WN and EN, are located 45° from the X-axis of the bearing shown in Figure 39. The south proximity probes, WS and ES, are located 135° from the bearing X-axis as shown in Figure 39.

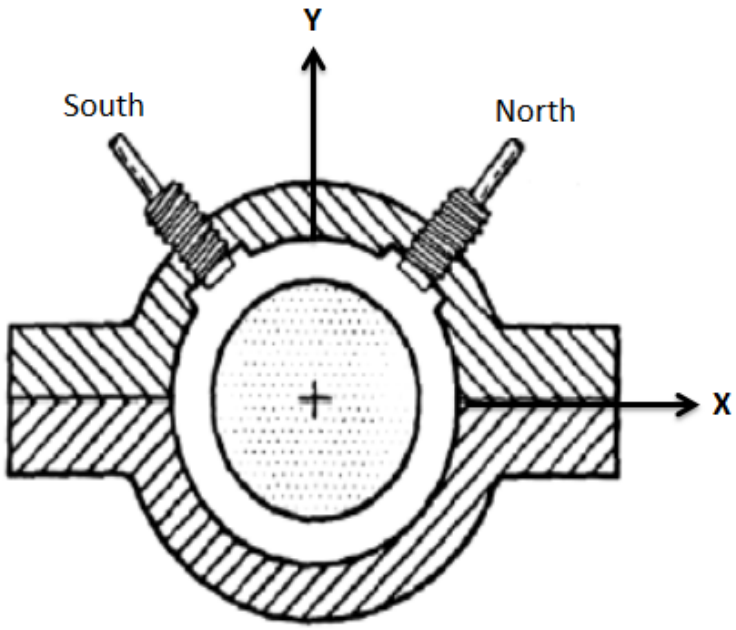

Figure 39 – Proximity Probe Mounting [19]

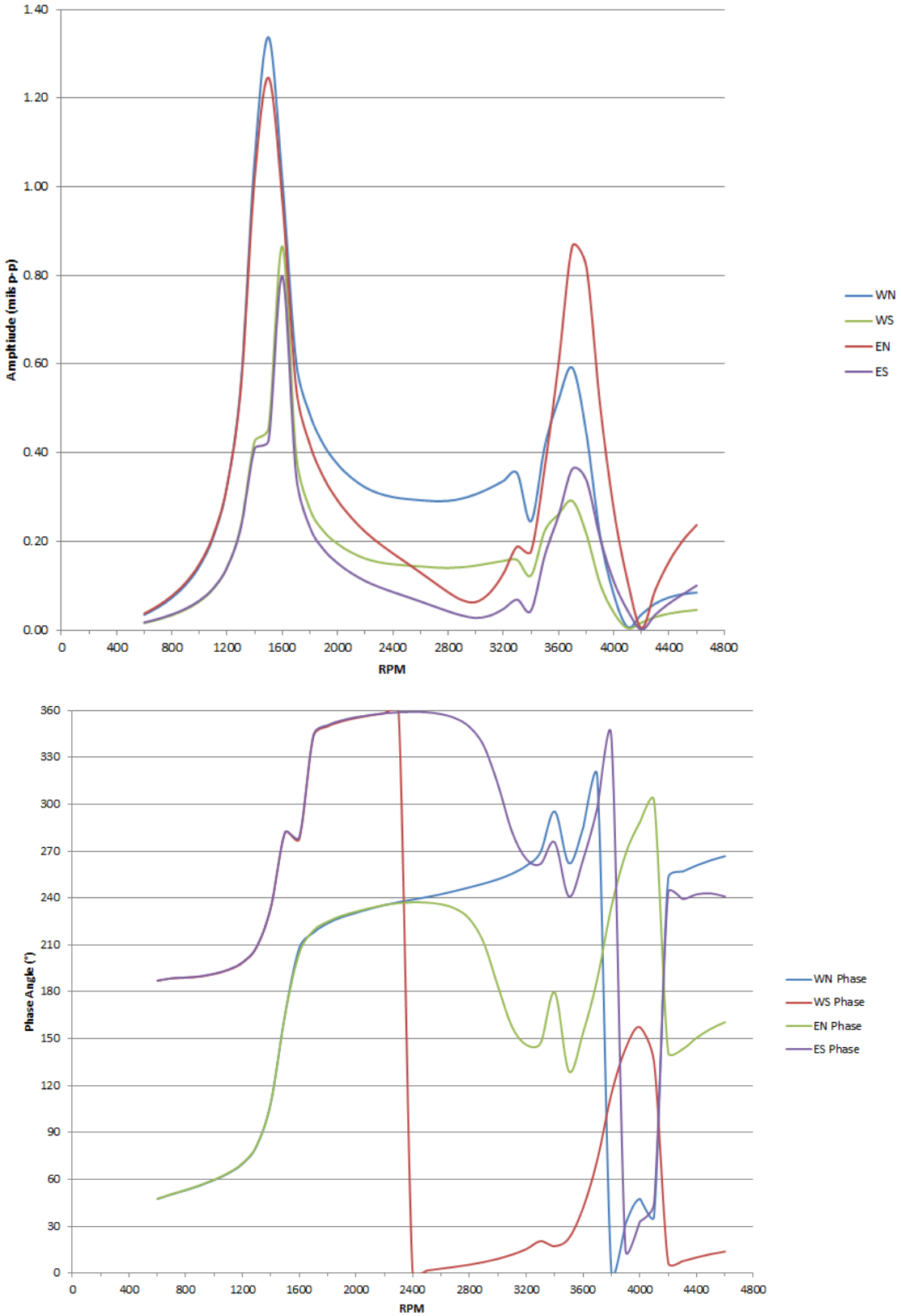

Figure 40 – Rotor-Pressure Dam Model Mode No. 1 Unbalance Response Bode Plot

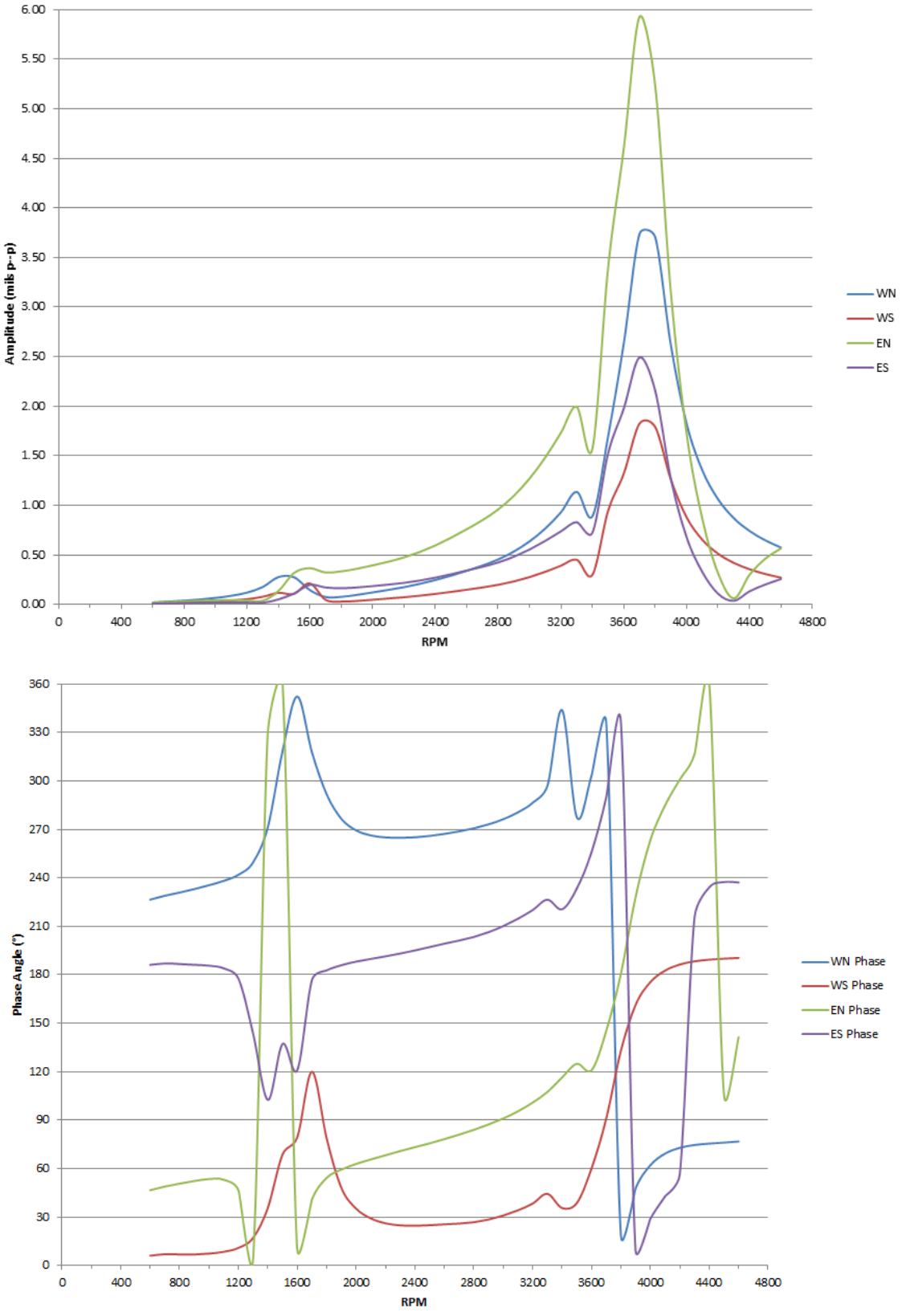

Figure 41 - Rotor-Pressure Dam Model Mode No. 6 Unbalance Response Bode Plot

With the operation of the rotor with pressure dam bearings modeled, the next step is to model the rotor with the sleeve bearing. Only one sleeve bearing spare was available to install in the machine, so the location of the highest vibration amplitude was used to determine where the bearing was place. The east bearing was changed in DyRoBeS© to a sleeve bearing to determine the influence of switching this bearing to determine if this will help vibrations. Section 3.6 will investigate this operation with Chapter 4 showing the actual run data from this switch in bearing types.

3.6 Rotor Model with Sleeve Bearing

Similar rotordynamic analyses were performed in investigating the behavior of the rotor with the sleeve bearing installed in the east bearing. The first investigation was an investigation into the various modes of the rotor. Figures 42, 43, and 44 show the first mode and its corresponding potential and kinetic energy distributions. This mode can be seen to be a flexible rotor mode. The mode occurs at 1565 RPM, slightly higher than the 1547 RPM of the rotor with two pressure dam bearings. The next critical speed, shown in Figures 45, 46, and 47, shows that the predicted second critical speed with the sleeve bearing is closer to the operational speed of 3600 RPM at 3641 RPM than the pressure dam second critical speed of 3708 RPM.

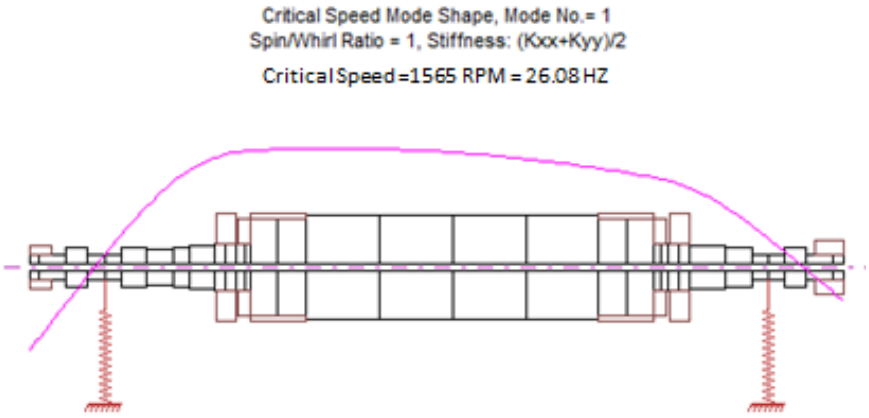

Figure 42 - Rotor-Sleeve Bearing Model Mode No. 1

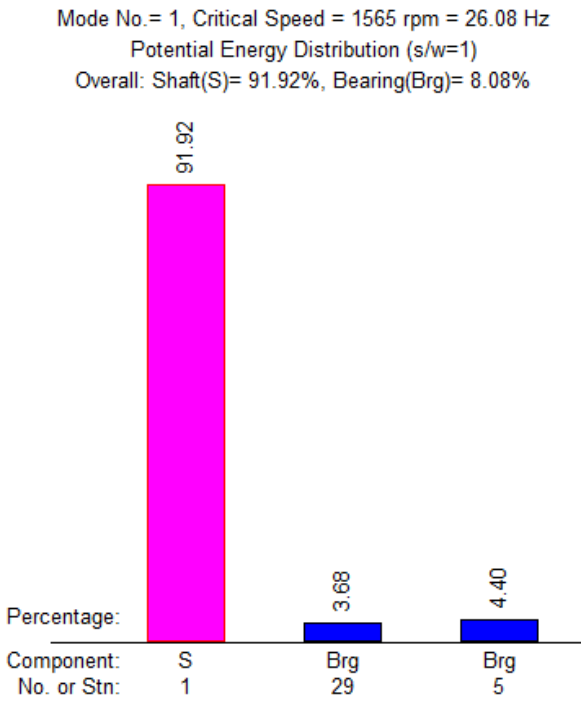

Figure 43 - Rotor-Sleeve Bearing Model Mode Shape No. 1 Potential Energy Distribution

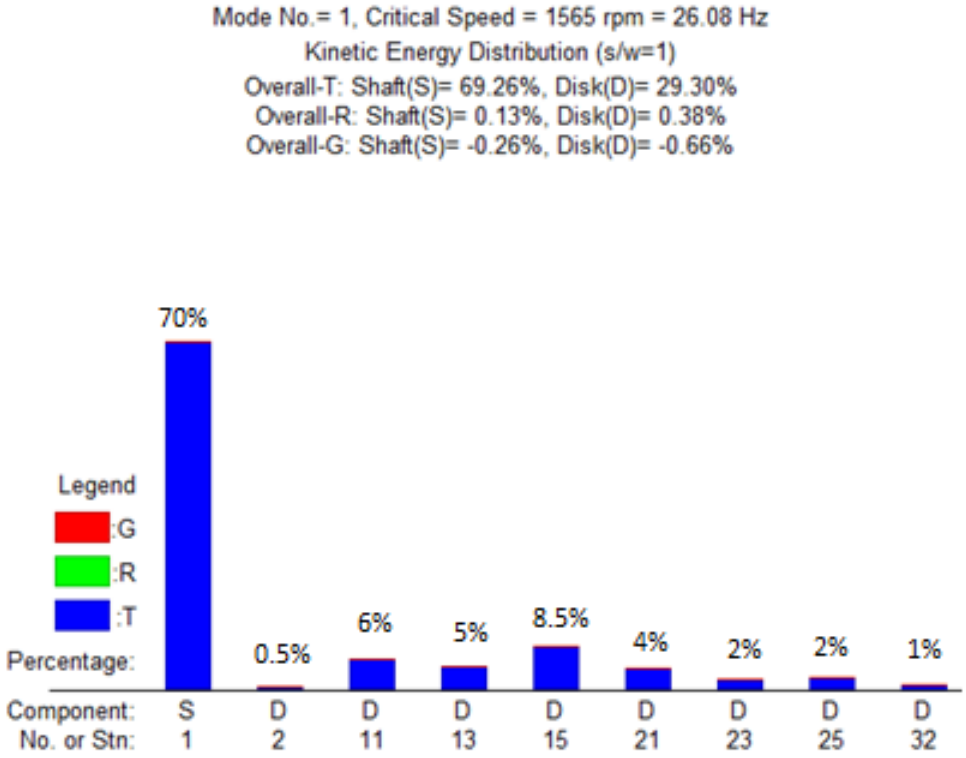

Figure 44 - Rotor-Sleeve Bearing Model Mode Shape No. 1 Kinetic Energy Distribution

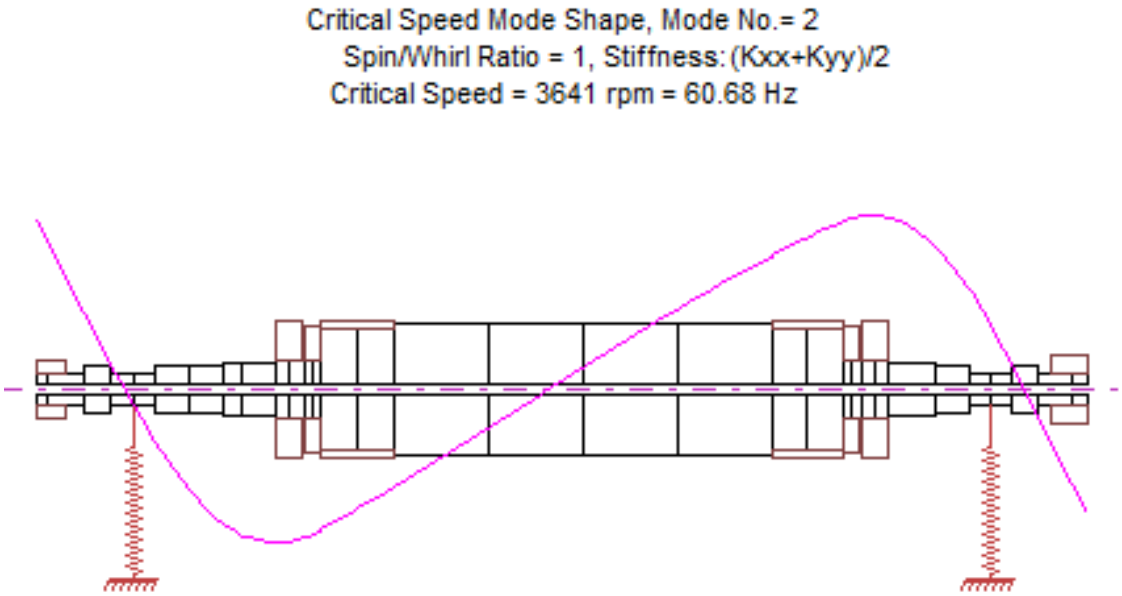

Figure 45 - Rotor-Sleeve Bearing Model Mode No. 2

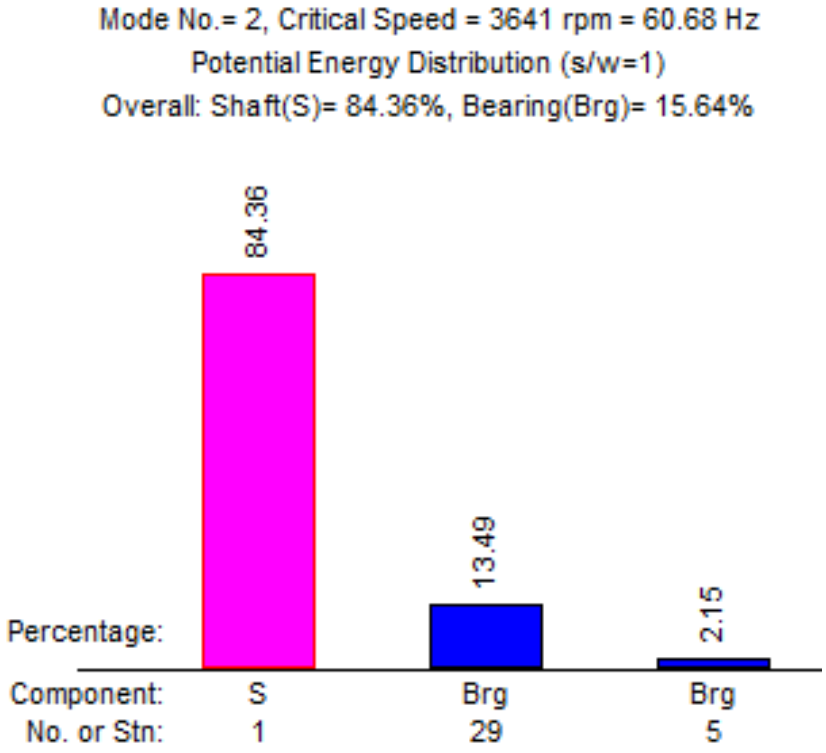

Figure 46 - Rotor-Sleeve Bearing Model Mode Shape No. 2 Potential Energy Distribution

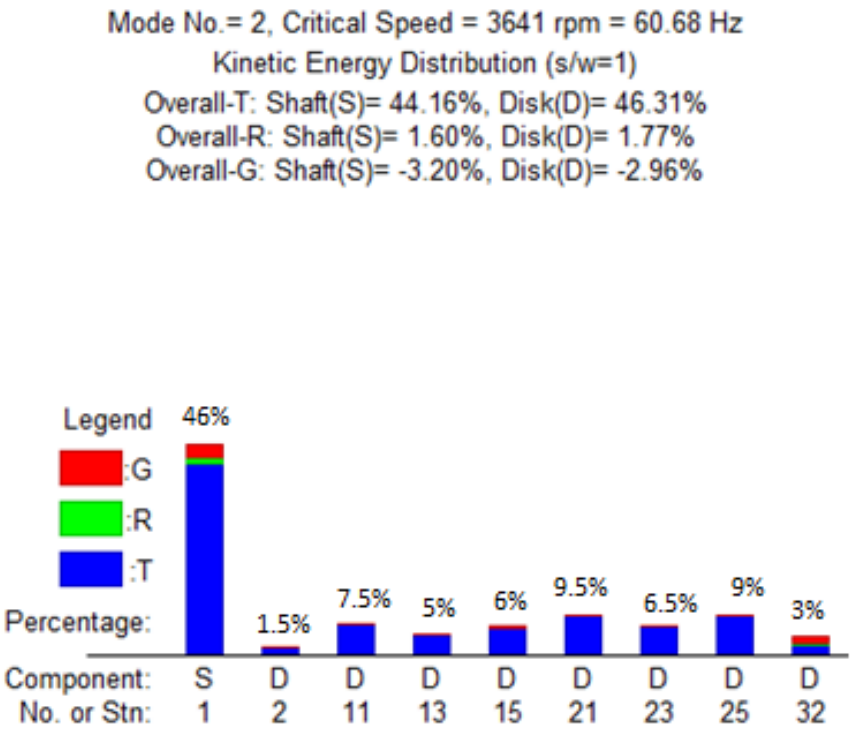

Figure 47 - Rotor-Sleeve Bearing Model Mode Shape No. 2 Kinetic Energy Distribution

For mode 2, the mode is a flexible rotor mode with an increased potential energy distribution in the bearing which was changed at Station 29. The shaft influence is less than that seen in the original two pressure dam model. Also, the influence of the couplings at station 2 and station 32 is much less than the original model, with a corresponding rise in the effects of the modeled disks near the windings on the rotor (cooling fan, retaining ring, centering ring). It is theorized that this is a result of the sleeve bearing being less stiff than the pressure dam bearings, resulting in greater mass translational energy (T) of the shaft and the disks between the bearing stations.

Next, a whirl speed and stability analysis was performed for speeds between 600 and 5000 RPM. The whirl speed map shows the various natural frequencies that the rotor passes as it comes to operating speed. As with the discussion in Section 3.5, not every natural frequency is important relative

to motor operation. A look at the individual mode shapes and their respective precessional motions and log decrement/damping values will determine which ones are expected to require an unbalance response analysis. Figure 48 shows the whirl speed map for the rotor-sleeve bearing system.

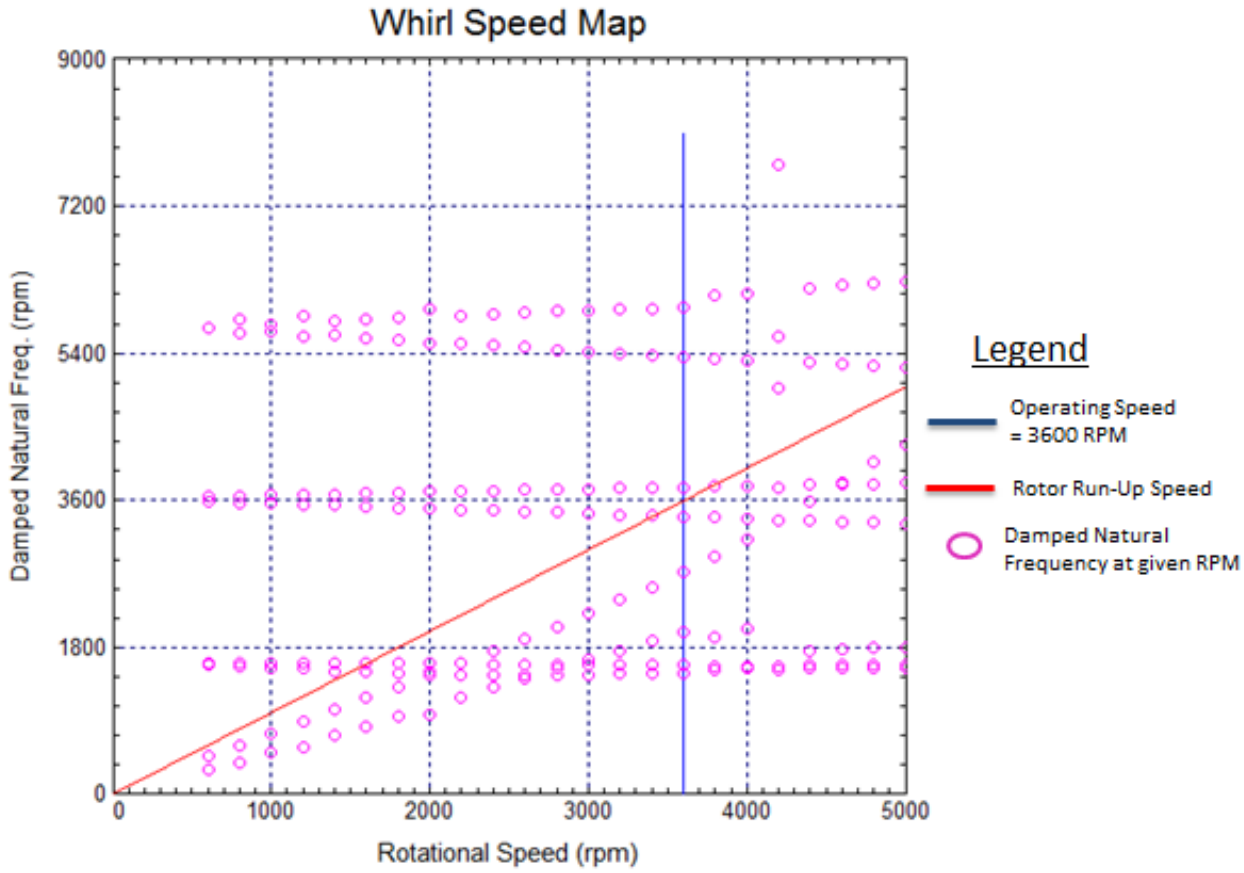

Figure 48 - Rotor-Sleeve Bearing Model Whirl Speed Map

As predicted by the critical speed analysis, the rotor passes through several natural frequencies as it comes up to speed during a start up or shut down. Two modes of particular interest are the ones around the rotor operational speed of 3600 RPM. The mode shapes shown in Figure 49 determine which ones are going to influence the rotor behavior.

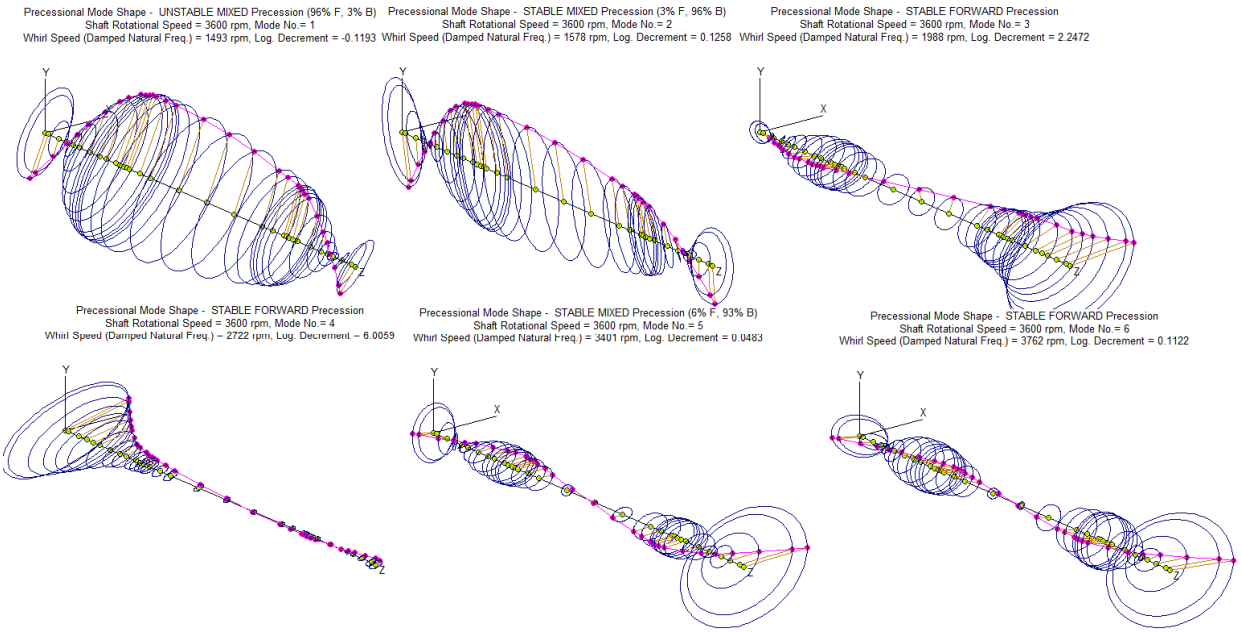

Figure 49 - Rotor-Sleeve Bearing Model Precessional Mode Shapes

As with the pressure dam modes, Mode No. 1 and Mode No. 6 are the mode shapes requiring further analysis. Unlike the previous analysis in Section 3.5, the first mode shape indicates an unstable mode with a negative log decrement of -0.1193. This means that the vibration amplitude may grow rapidly unless the rotor passes through the first critical speed quickly. Mode No. 1 is expected to be seen at 1493 RPM, very close to the pressure dam natural frequency occuring at 1491 RPM, and is the believed first critical mode of the rotor. Mode No. 2 and No. 5 are predominantly a backwards precessional mode, while Mode No. 3 and No. 4 are highly damped.

Mode No. 6, occurring at 3762 RPM, is the expected second critical speed. With a log decrement of 0.1122, the mode is lightly damped and is a stable forward precessional motion mode. This critical speed is slightly higher than the pressure dam mode No. 6 speed of 3755 RPM. The unbalance response test for both modes will determine the linear steady synchronous response. Figures 50 and 51 show the resulting Bode plots for the steady synchronous response of Mode No. 1 and Mode No. 6.

For Mode No. 1, 70.2 oz-in of unbalance was added to Station 18 of the model shown in Figure 28. From the Bode plot in Figure 50, changing the east pressure dam bearing to a sleeve bearing results in a decrease of the vibration amplitude on the east bearings when passing through the critical speeds at around 1600 RPM and 3800 RPM. While the critical speeds occur at the same speed, the east bearing dampens the amplitude of the vibration. Mode No. 6 was studied by applying 35.08 oz-in of unbalance to Stations 13 and 24, 180° apart as detailed in API 684 [13]. From the Bode plot in Figure 51, the unbalance forces excite the second critical speeds vibration amplitude.

The east bearing; however, shows that the sleeve bearing has damped the vibration on the east side by reducing the vibration amplitude detected in the east north vibration probe by half. Unfortunately, from the plot the vibration amplitude in the west has been greatly exacerbated with a maximum amplitude of 7.5 mils p-p. Running the rotor with vibration amplitudes approaching 7.5 mils p-p would greatly reduce the expected lifespan of the rotor. The data from the bearing change showed promise in improving the vibration levels of the rotor, although running near the second critical speed will lead to unpredictable performance. From this data, the bearing change was approved, and while the critical speed may not change dramatically the vibration levels should see some improvement. The following chapter, Chapter 4.0, details the results of the two motor checkout runs, before and after the bearing change.

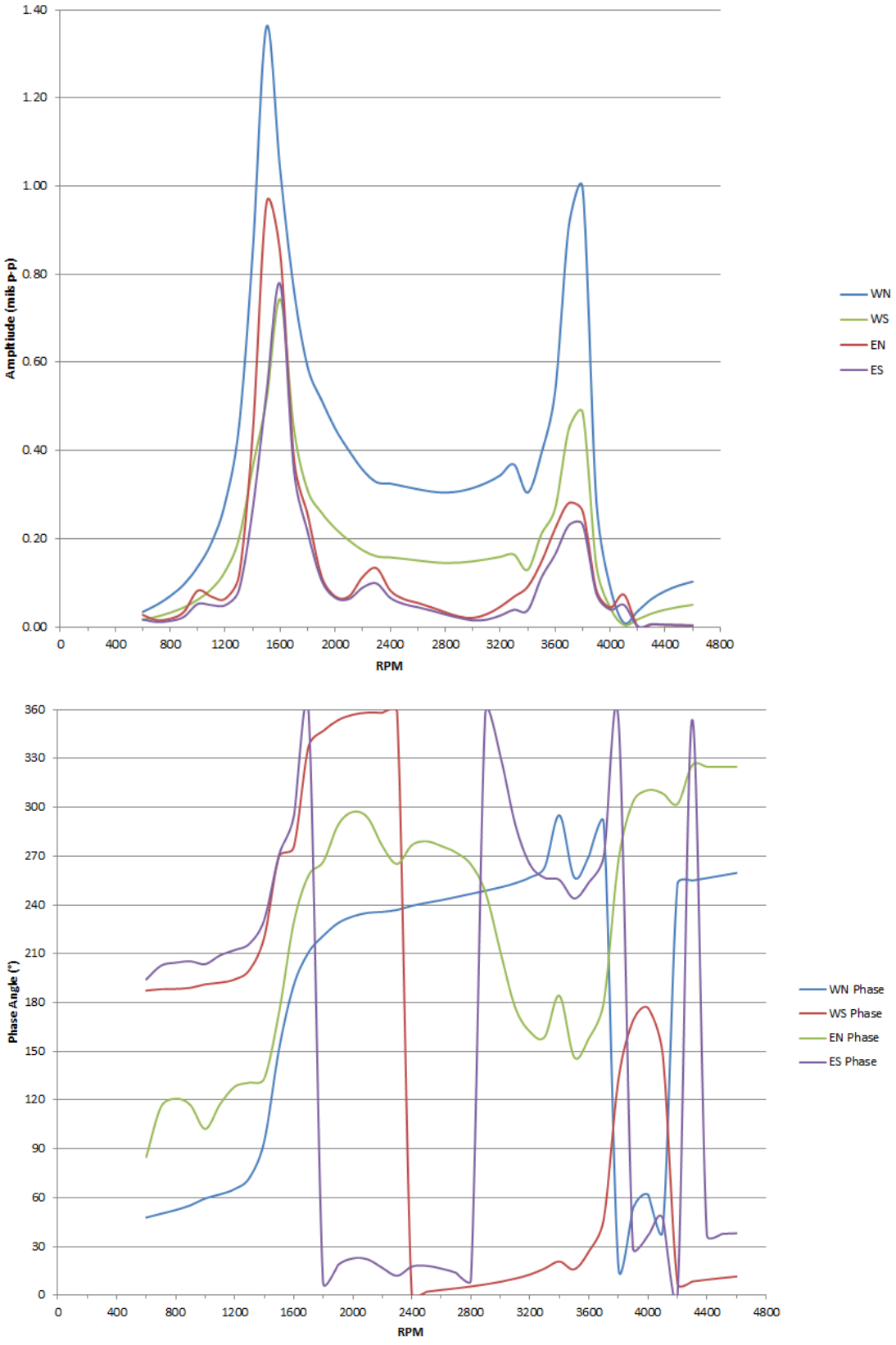

Figure 50 - Rotor-Sleeve Bearing Model Mode No. 1 Unbalance Response Bode Plot

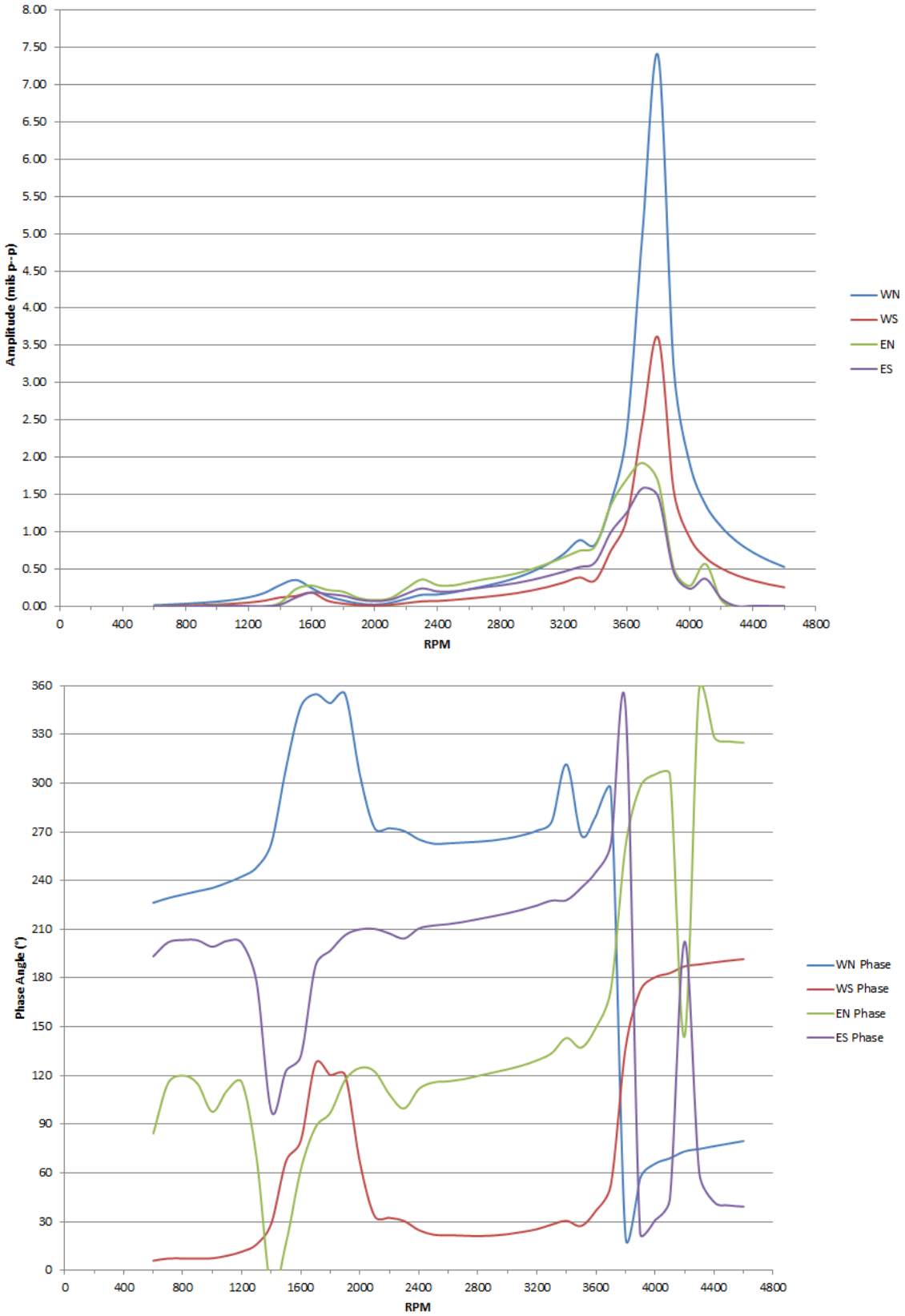

Figure 51 - Rotor-Sleeve Bearing Model Mode No. 6 Unbalance Response Bode Plot

4.0 Experimental Results

4.1 Experimental Set-Up

The VKF motors are 18,500 hp motors that rotate at 3600 RPM. Each rotor has a mass of approximately 15,200 lbm and is supported by two 7 inch diameter by 8 inches length bearings. The rotor is 203 inches long and 165.5 inches from the west bearing centerline to the east bearing centerline. At the bearings, lateral shaft motion is measured using Bentley Nevada 3300 series proximity probes which are installed at the 45° and 135° angle counter clockwise from the horizontal plane, respectively, as shown in Figure 39 of the previous chapter. The bearing housing split at the bearing centerline prevents installing the proximity probes at the bearing centerline, so the proximity probes are rotated 45° away from true horizontal and vertical.Each proximity probe provides vibration amplitude measurement uncertainty within ±1 mil (±0.001 inch). Shaft speed is provided by a Keyphasor™ probe, which is used to monitor a keyway on the shaft that provides a once per turn indication. The proximity probes combined with the Keyphasor™ provides lateral vibration measurements as well as the vibration signal phase.

For this test, the vibration signals were sent to a National Instruments IOtech 600 Series USB Digital Signal Analyzer. The digital signal analyzer was connected to a laptop with National Instruments eZ-TOMAS™ software (Total Online Monitoring and Analysis Software) installed. The eZ-TOMAS™ software takes the signals from each IOtech channel and provides programmable filters for each signal as well as time, spectrum, orbit, waterfall, Bode, polar, trend, and shaft centerline analysis capabilities [59]. Results provided in Section 5.0 of this thesis are taken from eZ-TOMAS™ software.

Bearings were machined at the AEDC Model Shop per approved drawings. Bearings were measured to ensure given tolerances were met. A Roper mechanical gear pump provided oil to the

bearings. Oil flow to the bearings was controlled by a needle valve. Turbine flowmeters measured lube oil flow to the bearings and provided a check that proper lube oil flow was getting to both bearings for each bearing type. Operation of the motor was handled by a PLC based control system. The first of the motor checkout runs is covered in the following section.

4.2 First Run – Pressure Dam Bearings

After the motor refurbishment project rewound the rotor and stator, checkouts were performed to ensure proper rotor-bearing operation. Using the existing pressure dam bearings, vibration measurements were taken to determine the location of critical speeds and system performance at operating speed. Data were logged on a laptop loaded with eZ-TOMAS™ software and full Bode plots, spectrum plots, waterfall plots, and others were kept for further analysis. This section will present the results from this run as well as the analysis of the first run. As will be seen, the rotor vibration levels are much higher than one would expect from a freshly rewound rotor which has undergone balancing in a high speed balancing pit prior to being installed in the VKF plant.

From the Bode plot shown in Figure 52, it can be seen that the first critical speed is located at approximately 1633 RPM, or 27.5 Hz. The rotor model predicted a first critical at 1565 RPM, which is a difference of 2% relative to the rotor operational speed. Please note that the phase angle measurement is constrained to 0 to 360°, so when the angle shifts above 360° it wraps around to 0° as shown near the critical speed. Per the API code [13], this critical speed has a calculated amplification factor of 5.41 with a separation margin of 1967 RPM away from the operating speed of 3600 RPM. At this amplification factor and running below operational speed, the required separation margin is 12.65% of the operating speed, or 455 RPM. Therefore, there is sufficient separation from this critical speed to the operating speed per API requirements detailed in SP6.8 of API RP 684. The spectrum plot of the first critical can be seen in Figure 53.

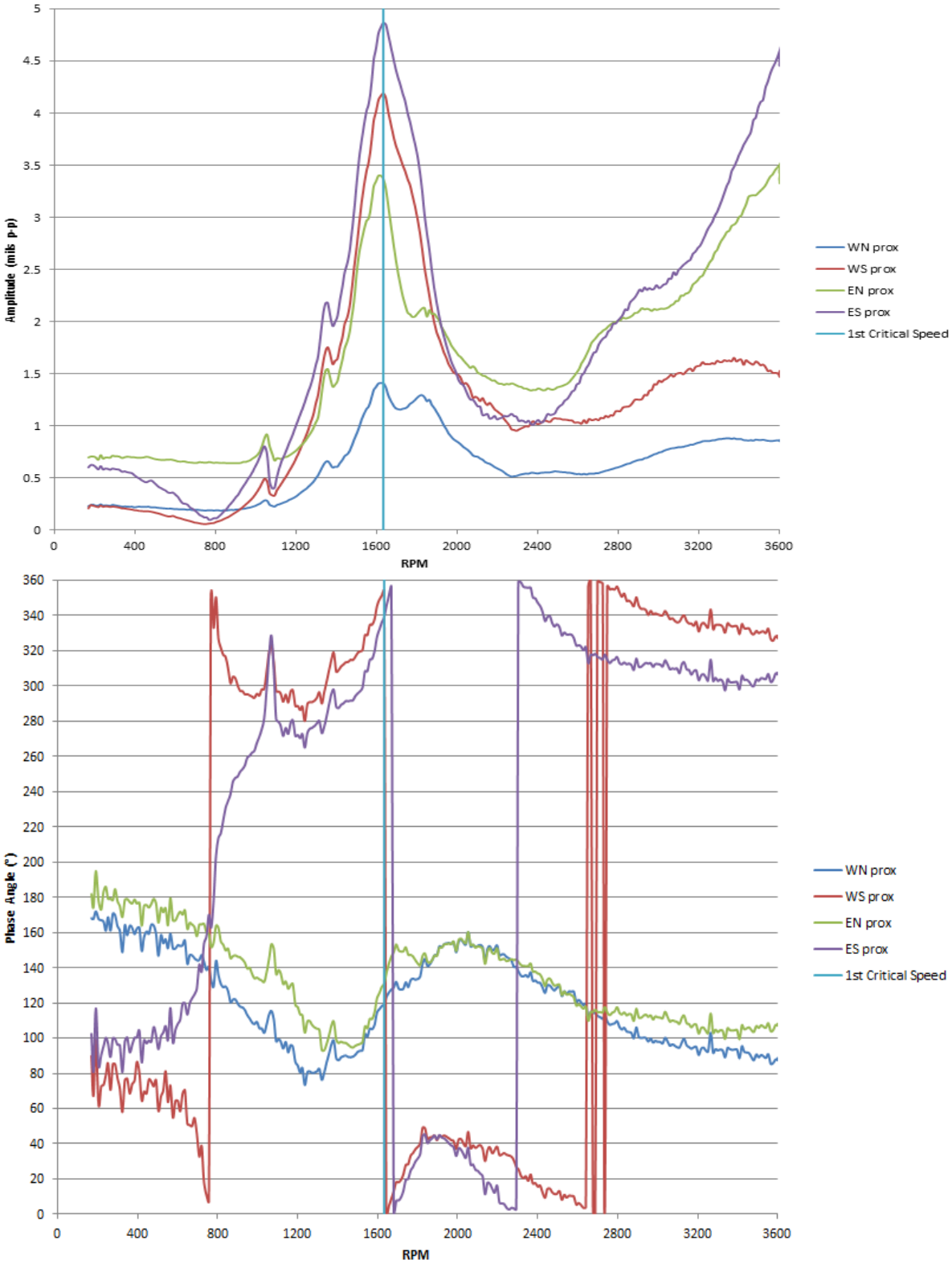

Figure 52 – Motor Checkout Start-Up Bode Plot

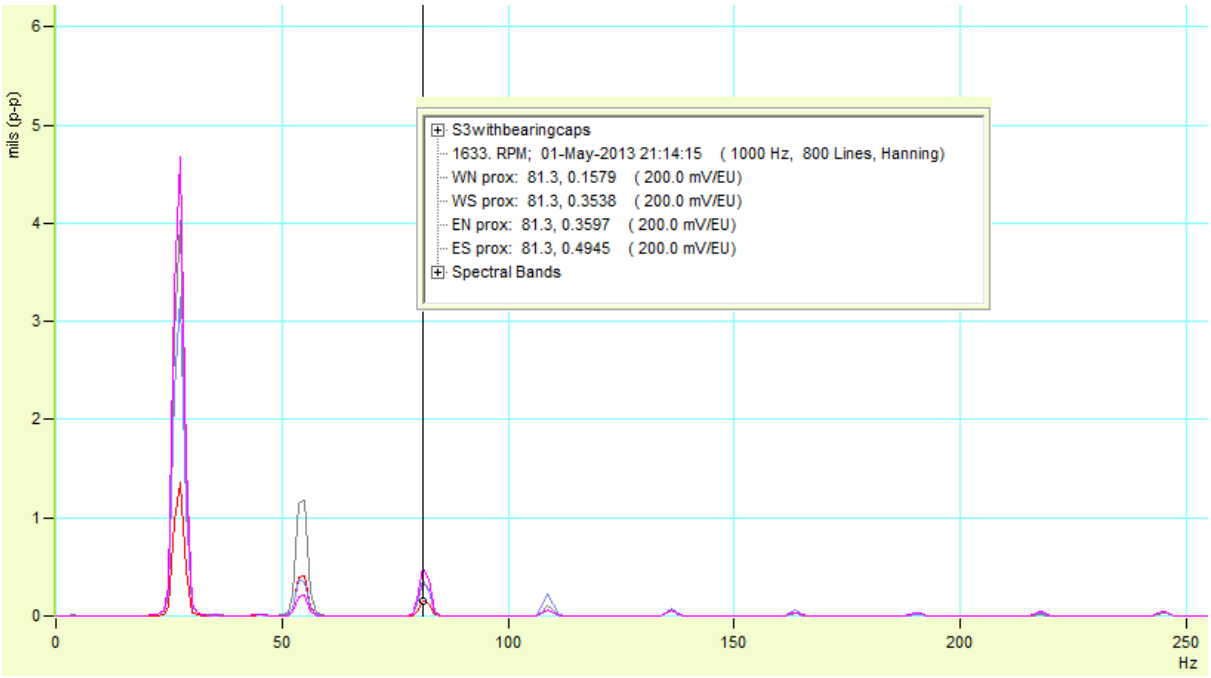

Figure 53 – Motor Checkout 1st Critical Speed Spectrum Plot

As can be seen in Figure 52, as the motor comes up to operating speed, the vibration amplitude slowly begins to climb, which is most pronounced in the east bearing probes, eventually peaking at 4.6 mils peak-to-peak (p-p). As was shown in Chapter 3, the model predicted that the rotor operation was infringing on the second critical speed. One of the primary methods of verifying a critical speed is looking at the harmonic vibration spectra, also known as the 2X and 3X vibration spectra. Excitation of the 2X frequency vibration spectra is occurring in Figure 54. Figure 54 is the waterfall plot for the rotor-bearing system as the 1X (or one times the RPM) spectra passes through the first critical. A waterfall plot shows the frequency of the vibration in hertz on the x-axis and the amplitude in mils p-p on the y-axis. The frequency in hertz (Hz) can be calculated by multiplying the speed of the rotor multipled by 1/60. The z-axis shown is time, so the waterfall plot shows the 1X (operating speed) vibration signature as the rotor comes up to speed and the various harmonic (2X, 3X, etc.) vibration spectra.

From the Bode plot in Figure 52, the vibration increases through the first critical and decreases as the rotor passes through the first critical over the speed range of approximately 1400 RPM-2000 RPM. At approximately 30 Hz, 1800 RPM, the 2X vibration strongly increases. This indicates that at two times the operating speed of 1800 RPM, a natural frequency occurs which excites the rotor. This excitation occurs until approximately 2100 RPM, as shown in Figure 55, before the vibration levels decrease and the excitation ceases.

This indicates there is a critical speed occurring somewhere in the range of 3600 RPM-4200 RPM. While the waterfall figures are simply snapshots in time of a transient event, the data appears to match the predictions coming from the model using the pressure dam bearings. As the rotor comes up to operational speed, the vibration levels increase as the rotor comes up on the second critical speed. This excitation is seen in the spectrum and waterfall plot of Figures 56 and 57, respectively.

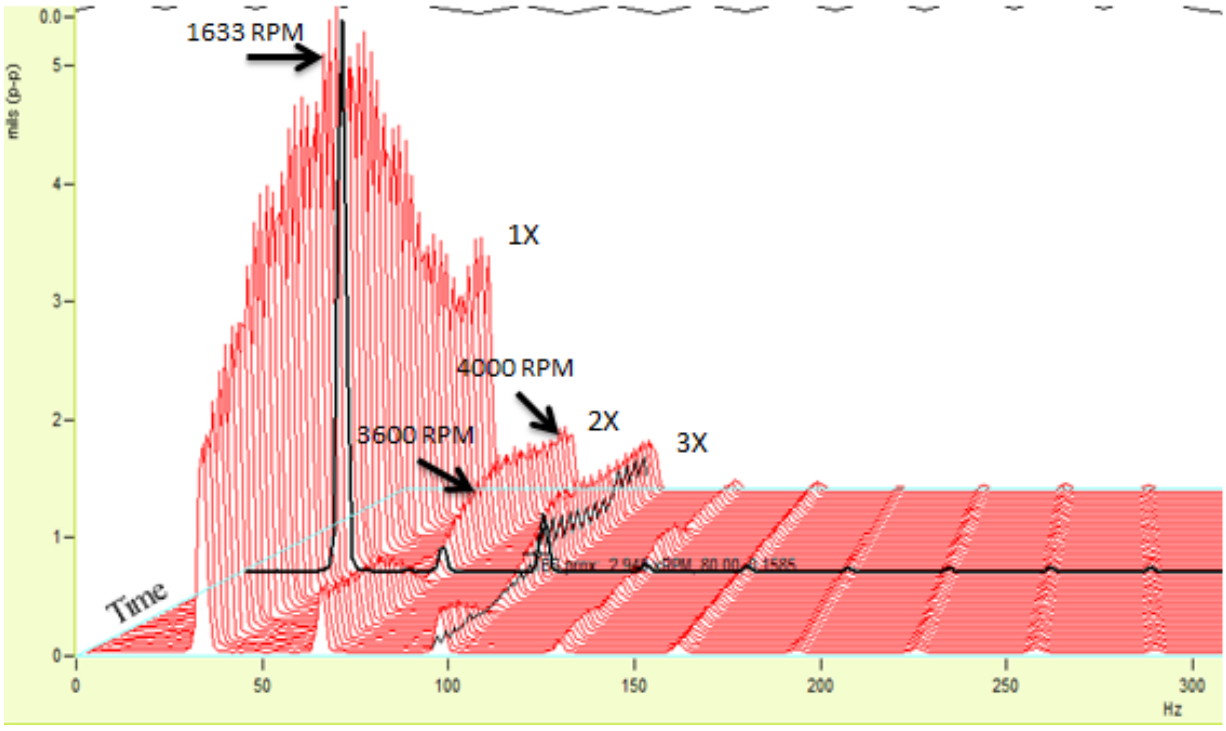

Figure 54 – Motor Checkout Critical Speed Waterfall Plot – ES Prox Probe

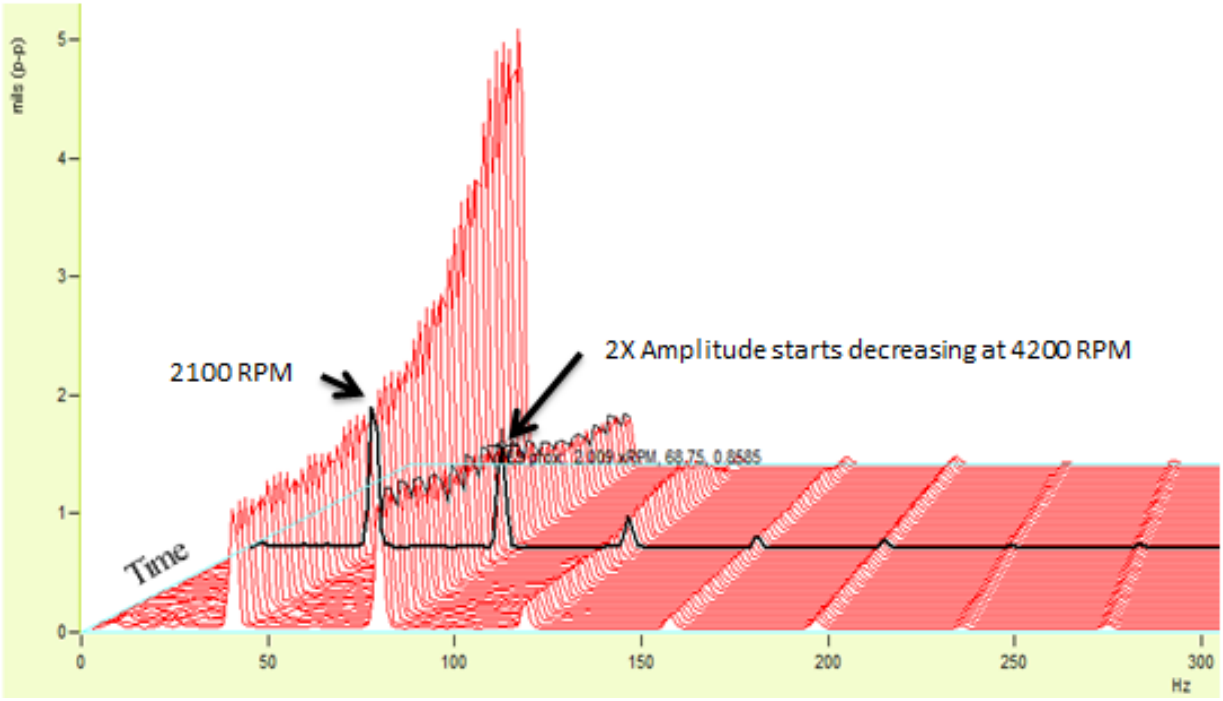

Figure 55 – Motor Checkout 2X Harmonic Waterfall at 2100 RPM – ES Prox Probe

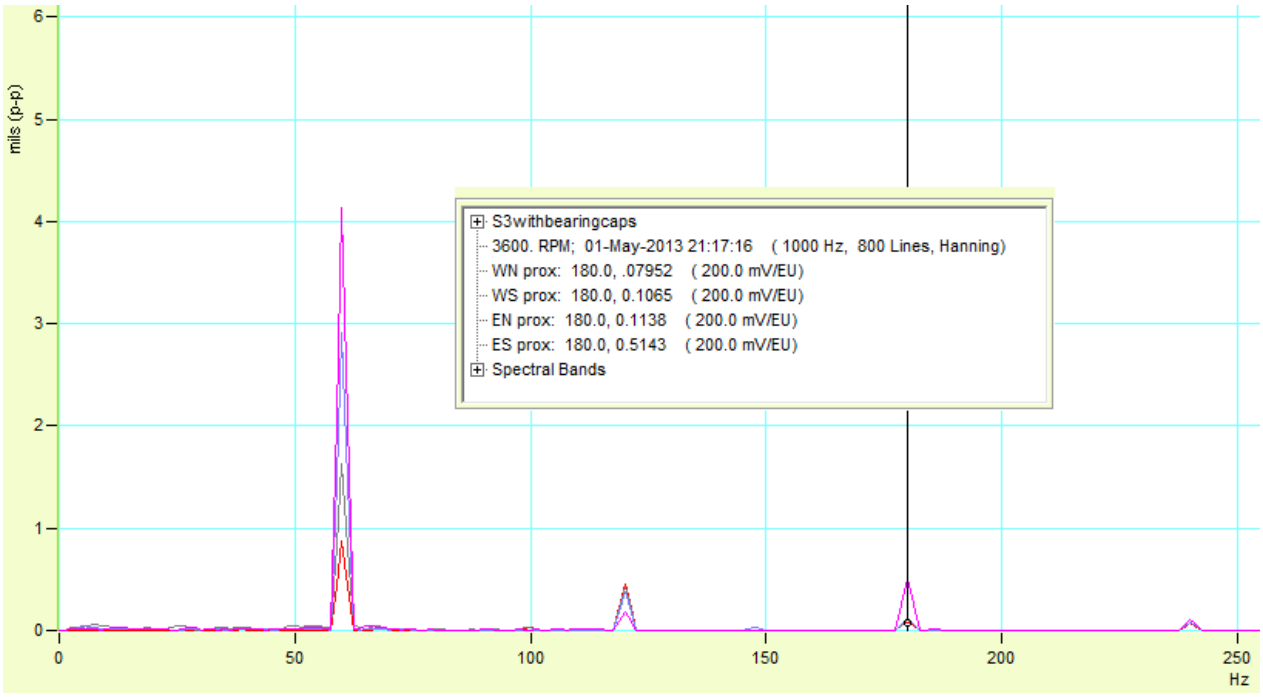

Figure 56 – Motor Checkout Operating Speed Spectrum Plot

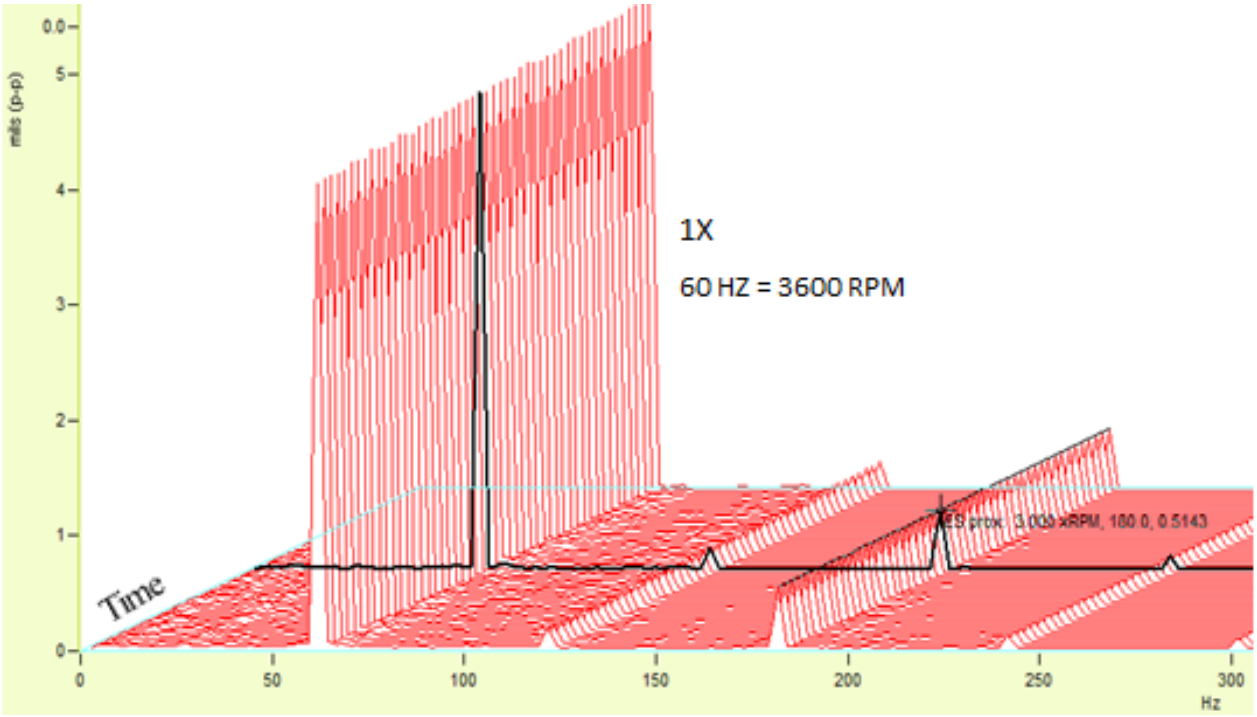

Figure 57 – Motor Checkout Operating Speed Waterfall Plot – ES Prox Probe

Once the checkout was performed and the motor performance checked at various loads, the motor transients from the shut down were also analyzed. The Bode plot for the run down of the motor checkout is presented in Figure 58. As can be seen, from the coast down transient the first critical appears in the form of a split critical speed between the speeds of 1486 and 1338 RPM. Split criticals are common in generator rotors due to the rotors inherent construction. These split criticals are the result of differing horizontal and vertical stiffnesses in the rotor. Due to the windings in the two pole generator core, the stiffness of the rotor is different in the two principal directions [42]. While this effect was not included in the rotor model, the effects of dissimilar stiffnesses can be seen in the rotor data.

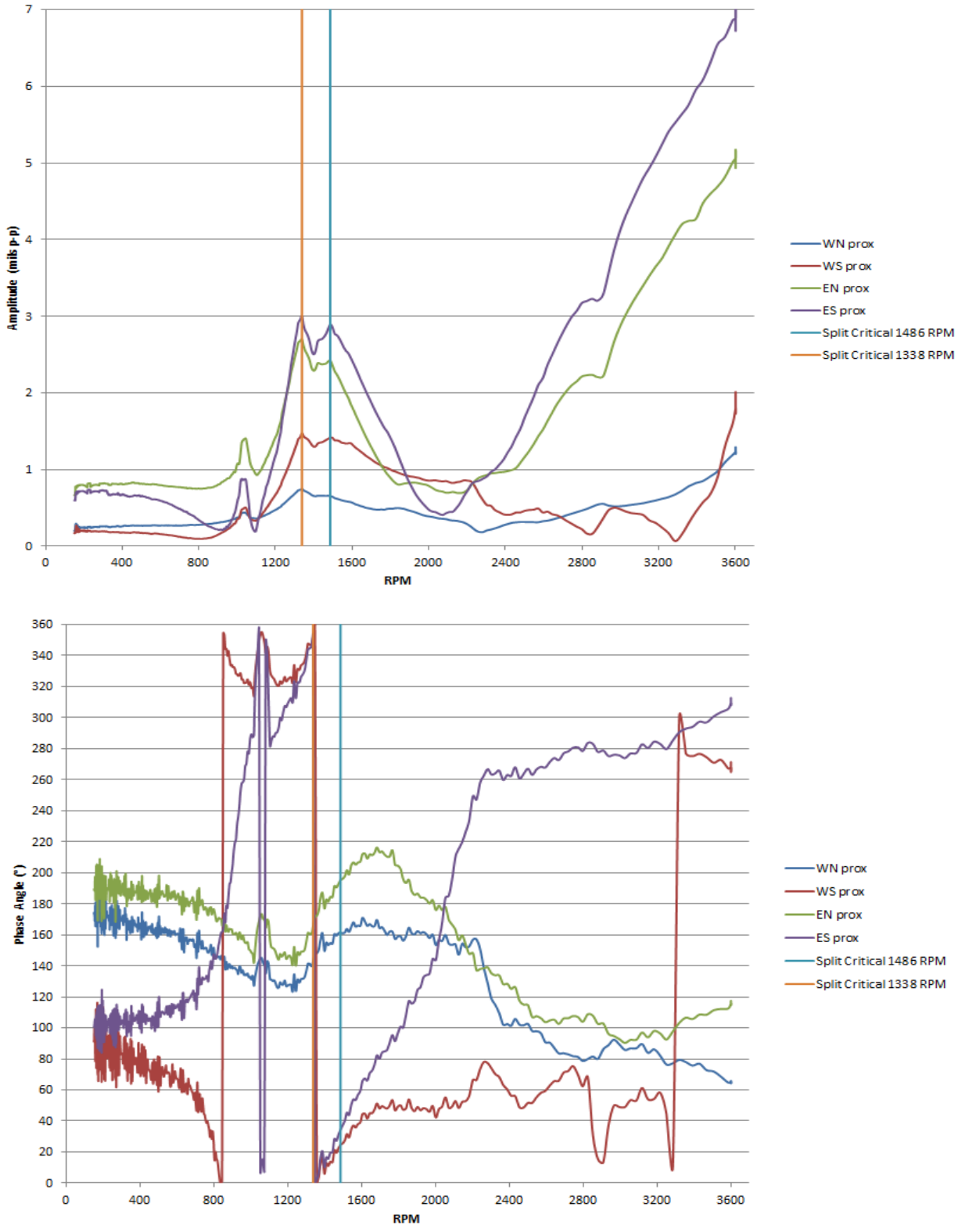

Figure 58 – Motor Checkout Coast Down Bode Plot

From Figure 58, it is seen that the vibration amplitude during the checkout had creeped upwards to 7 mils. Expected operation of a newly would rotor should be less than one mil. As the rotor coasted down from operating speed, the harmonic 2X frequency is excited as shown in Figure 59, the waterfall plot at the 1X frequency of 30 Hz (1800 RPM) . The critical speed still occurs in the region of 3600 RPM-4200 RPM, which was the same as using the run-up data. This furthered speculation that the rotor was running near the second critical, or that there was some other unknown occurring such as a thermal sensitivity issue. Because of these findings, the proposed experiment to shift the critical speed by switching to sleeve bearings was approved and these findings will be presented in Section 4.3.

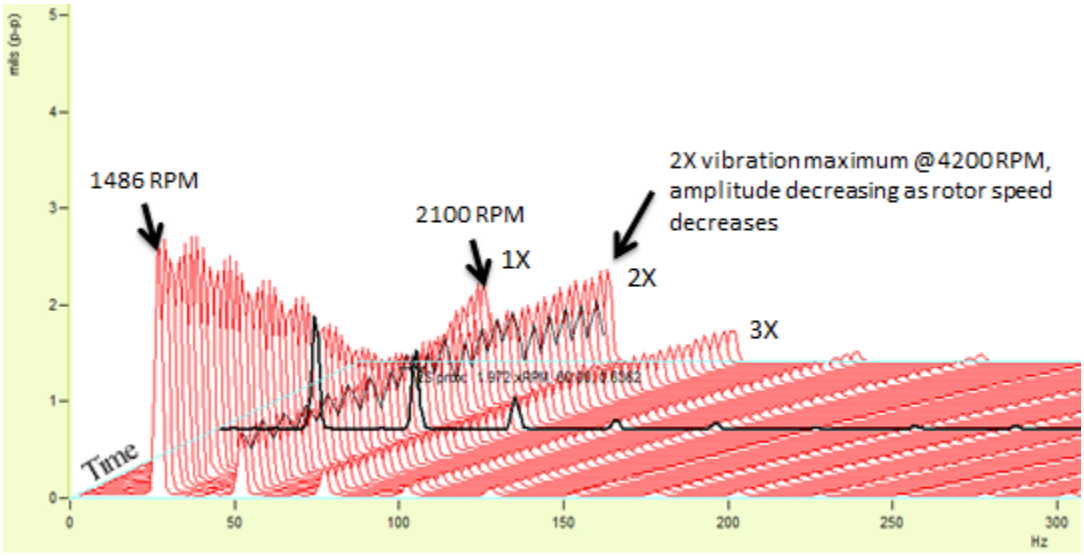

Figure 59 – Motor Checkout Coastdown 1800 RPM Waterfall Plot – ES Prox Probe

4.3 Second Run – Sleeve Bearing Checkout

After the results of the first checkout with the pressure dam bearings, a proposal was made to switch to sleeve bearings, where were the original system design. This proposal was an attempt to provide two main data points. First, the bearings would provide a baseline to build a case for using the

pressure dam bearings if they were in fact necessary, as records for the reasoning behind the shift to pressure dam bearings on the motor were unavailable. Also, it was believed that a sleeve bearing built to meet original specifications could shift the critical speed away from running speed. Because there was only one spare bearing shell available, it was determined to change the east bearing first, as that bearing showed the highest vibration amplitudes in the pressure dam bearing checkouts. The bearing clearance for the new bearing was machined the same as the pressure dam bearing, or 0.012 inches diametral clearance. The results from this particular motor bearing checkout are presented in the following pages.

First to be presented from the sleeve bearing checkout is the system start-up. In Figure 60, the Bode plot shows that the first critical speed is located at approximately 1680 RPM, or 28 Hz, slightly higher than 1633 RPM pressure dam bearing critical. The critical speed has a calculated amplification factor of 5.79 with a separation margin of 1920 RPM away from the operating speed of 3600 RPM. At this amplification factor and running below operational speed, the required separation margin is 13.04% of the operating speed, or 469 RPM. Therefore, there is sufficient separation from this critical speed to the operating speed per API requirements detailed in SP6.8 of API RP 684.

Figures 61 and 62 present the spectrum and waterfall plot from the first critical speed. From the Bode plot in Figure 60, the critical speeds' amplitudes on the east bearing are considerably more damped, as vibration ampltitudes that approached 5 mils at the first critical speed with the pressure dam bearings did not exceed 1 mil. The west bearing vibration amplitudes from each probe are within half a mil of each other from the pressure dam checkout. The east proximity probes were reading lower than the pressure dam bearings at the critical, by comparing Figure 52 and 60 . From the Bode plot, the sleeve bearing has had the positive effect of reducing the vibration amplitude in the east bearing.

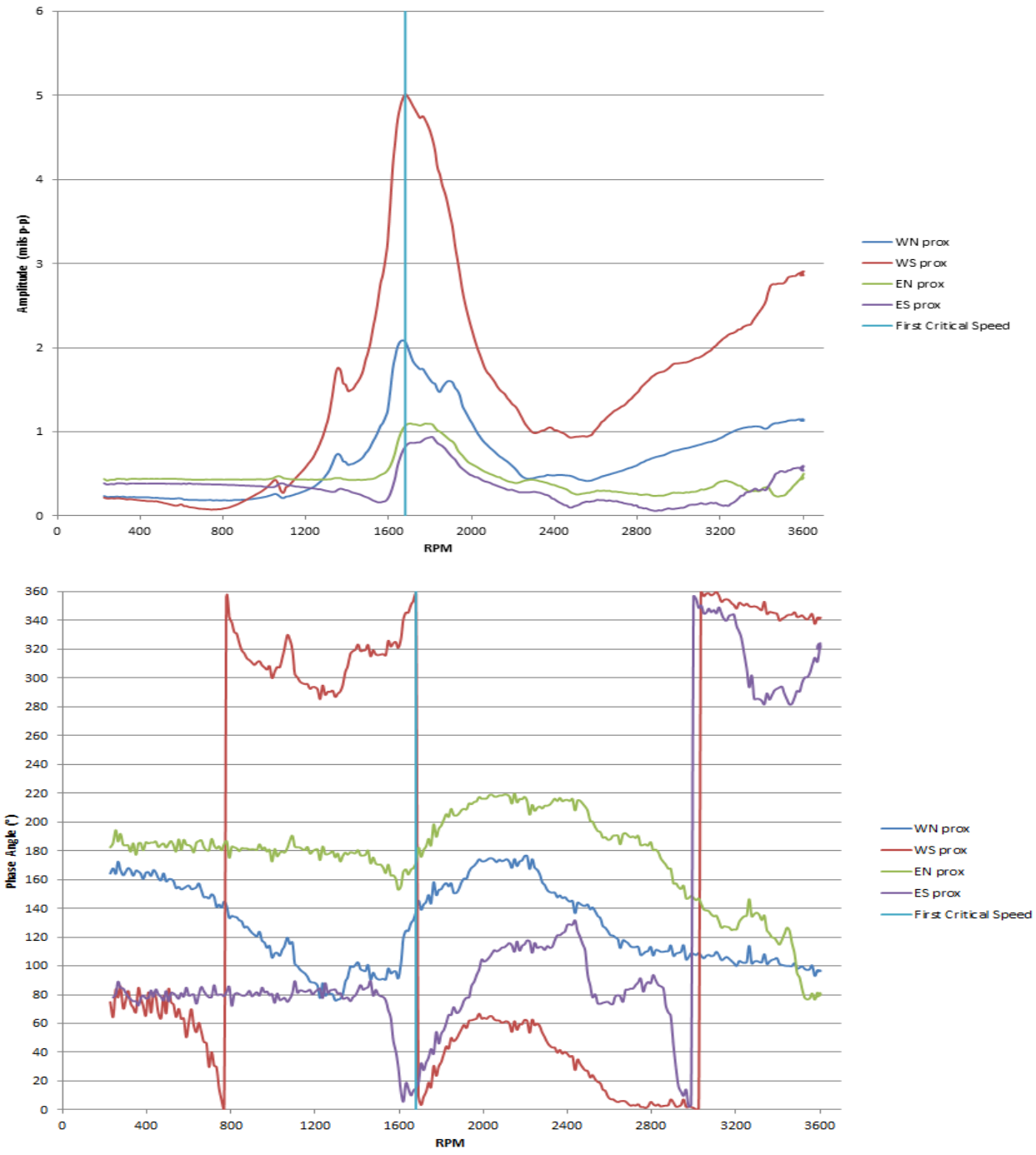

Figure 60 – Sleeve Bearing Checkout Start-Up Bode Plot

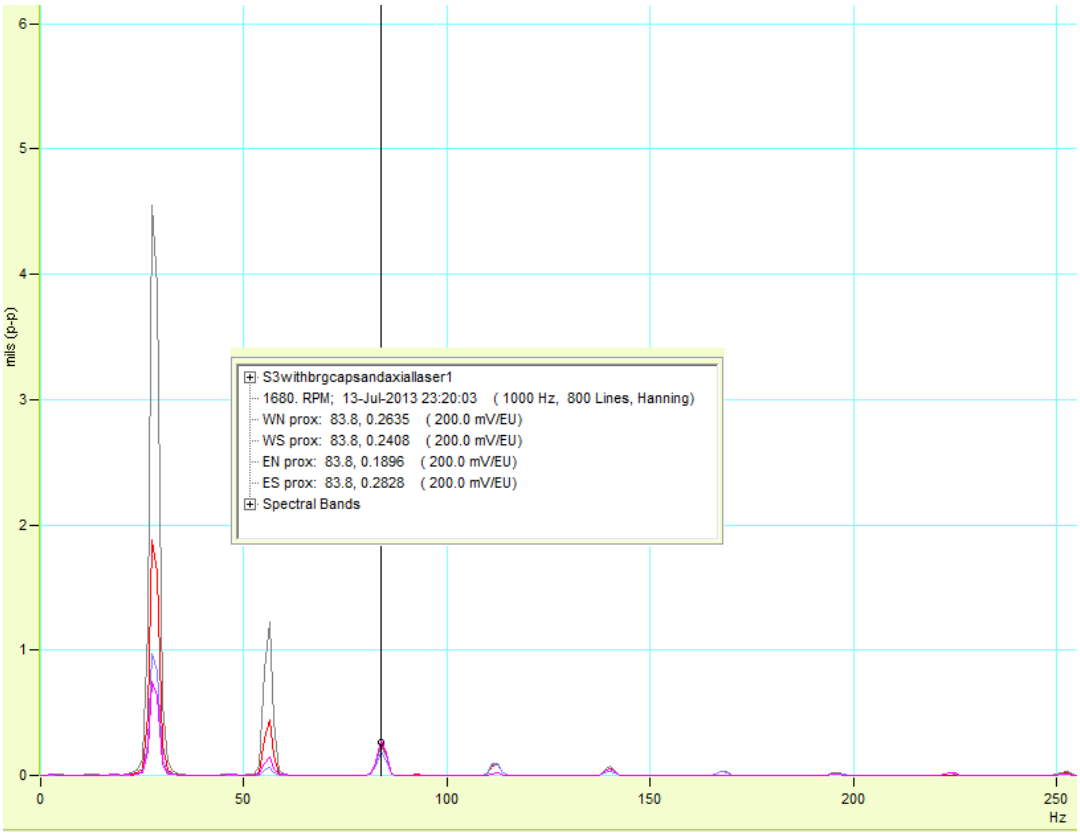

Figure 61 – Sleeve Bearing Checkout First Critical Speed Spectrum Plot

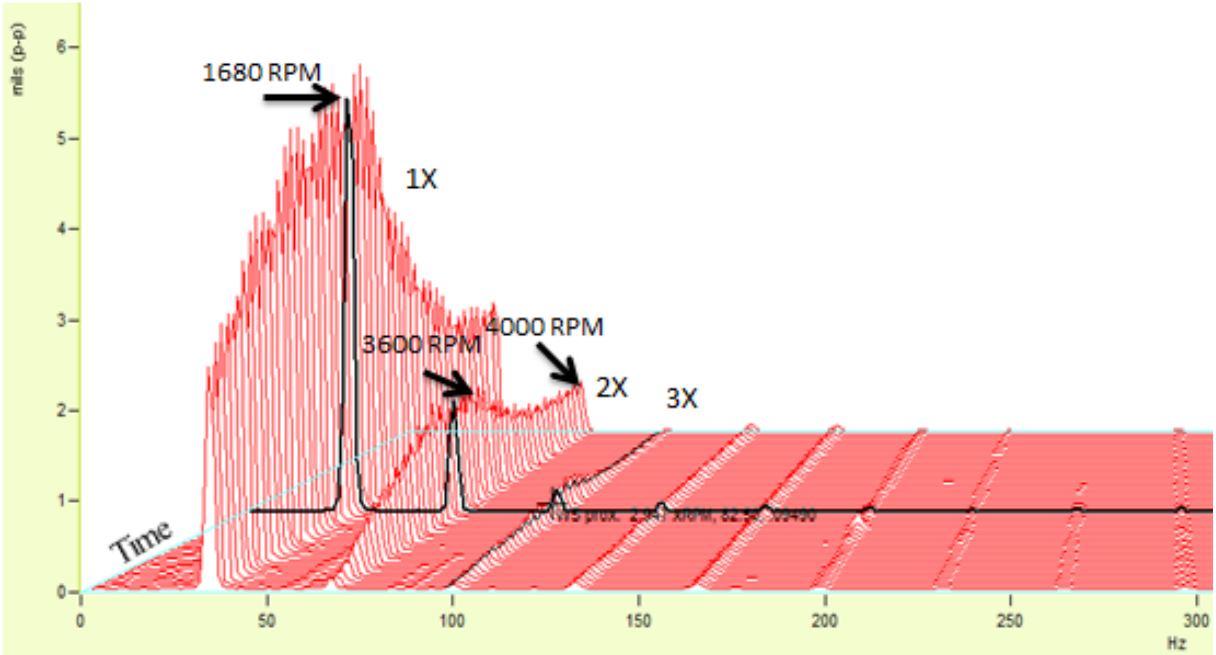

Figure 62 – Sleeve Bearing Checkout Critical Speed Waterfall Plot – WS Prox

Figure 62 depicts the waterfall plot for the west south proximity probe, which had the highest amplitude during the motor checkout. The 2X spectra was excited as the rotor passes through the 1800-2100 RPM speed range, which also indicates a second critical speed in the same location as with the pressure dam bearing run between 3600-4200 RPM. The maximum excitation occurs at around 3600 RPM, right at the operating speed of the machine. At operating speed; however, the maximum amplitude of the rotor vibration is considerably less, as the bearing change dampened the vibration. The amplitudes of the east vibration probes were around 1 mil at the critical speed, which saw a reduction in over 3 mils p-p vibration amplitude in each bearing probe.

At operating speed, the effect was even more pronounced. From the Bode plot, Figure 60, the highest amplitude vibration was seen at the west south vibration probe and reached less than 3 mils peak-to-peak. Figures 63 and 64 present the spectrum plot and waterfall plot at operating speed. The waterfall plot confirms the reduced vibration amplitudes at running speed.

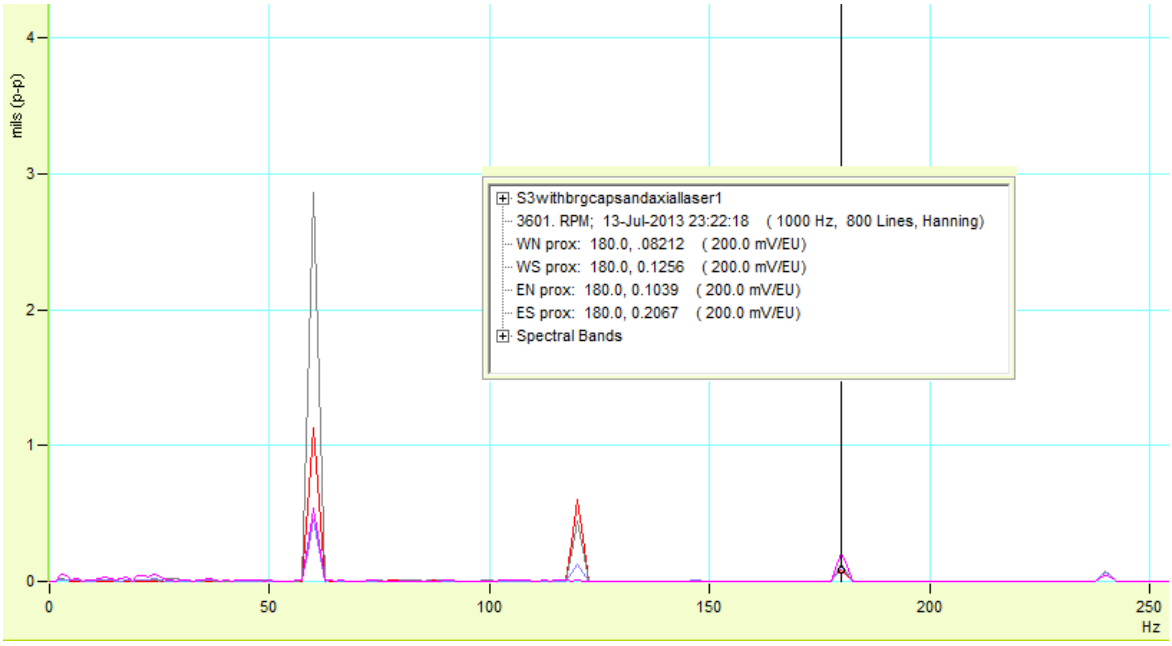

Figure 63 – Sleeve Bearing Checkout Operating Speed Spectrum Plot

The performance of the rotor-bearing system during coast-down was also investigated during the journal bearing checkout. Bode plots, spectrum plots, and waterfall plots were created from this data and are shown in Figures 65, 66, 67, and 68. These plots show that the east vibration values over the course of the checkout had begun to drift upward before finally settling at 2.8 mils p-p. The west south vibration probe amplitude had decreased, from almost 3 mils p-p to 2.2 mils p-p. Vibration amplitudes shifting as the rotor warms up during the system checkout can be indication of thermal sensitivity [5] or that as the copper windings warm up, the overall stiffness of the rotor decreases which could shift the rotor closer to the second critical speed.

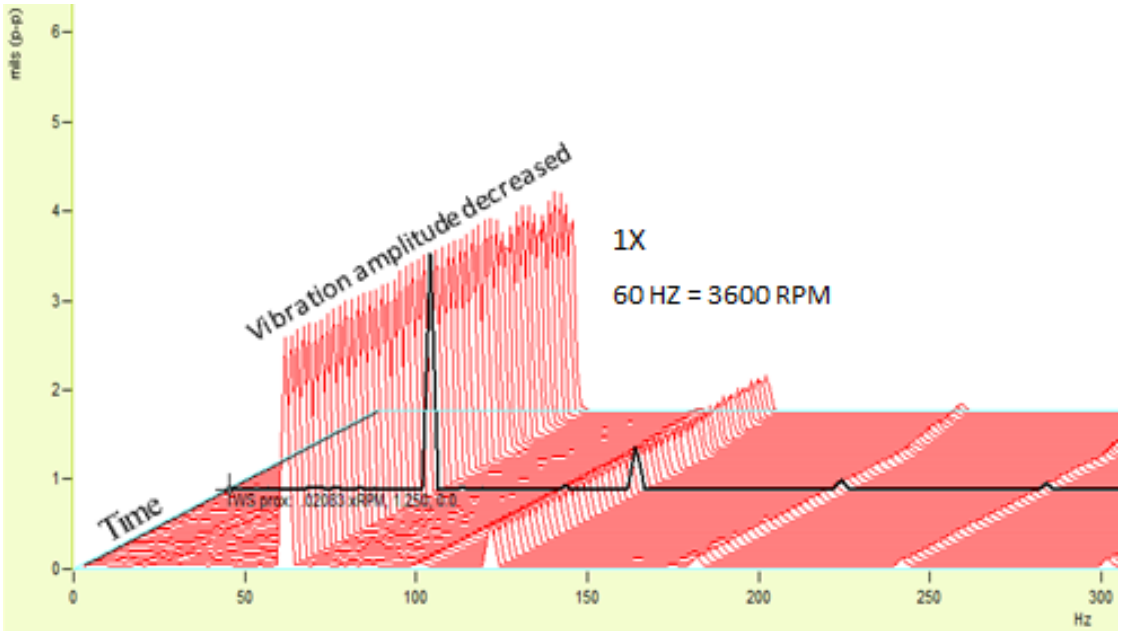

Figure 64 – Sleeve Bearing Checkout Operating Speed Waterfall Plot – WS Prox

The spectrum plot and waterfall plots, Figures 66, 67, and 68, show the coast down vibrations at the operating speed of 3600 RPM. It does not appear that the critical speed has been shifted away from operational speed by the switch from pressure dam to sleeve bearings. As in the pressure dam bearing

checkout and the sleeve bearing run-up, the 2X harmonic is excited as the rotor coasts down through the first critical speed in the range of 1600-2000 RPM. This excitation is shown by Figure 67. The excitation of this harmonic spectra points to a nearby second critical speed close to the operational speed of the rotor. While each of the four probes showed the 2X harmonic excitation, the west south (WS) probe was chosen for Figure 67 as the higher vibration amplitudes provided the best indication of the harmonic excitation which was occurring. The excitated 2X spectra actually indicates that the change in bearing type actually shifted the critical speed closer to operational speed; however, the vibration amplitudes are lower at the critical.

After the experiment is performed, the data imply that there is a second critical speed near the operational speed of the rotor, as did the rotor-bearing model results shown in Chapter 3.0. Chapter 5.0 will finalize these conclusions and compare the results from the rotor model performed in DyRoBeS©. From the rotor performance checkouts, the determination was made to stick with the journal bearings until a better alternative could be found. The vibration amplitudes were less across the board after installing the sleeve bearing in the east bearing pedestal. A spare bearing shell will be babbited and machined to install a sleeve bearing in the west bearing pedestal and future checkouts will confirm the rotor-bearing system operation with two sleeve bearings.

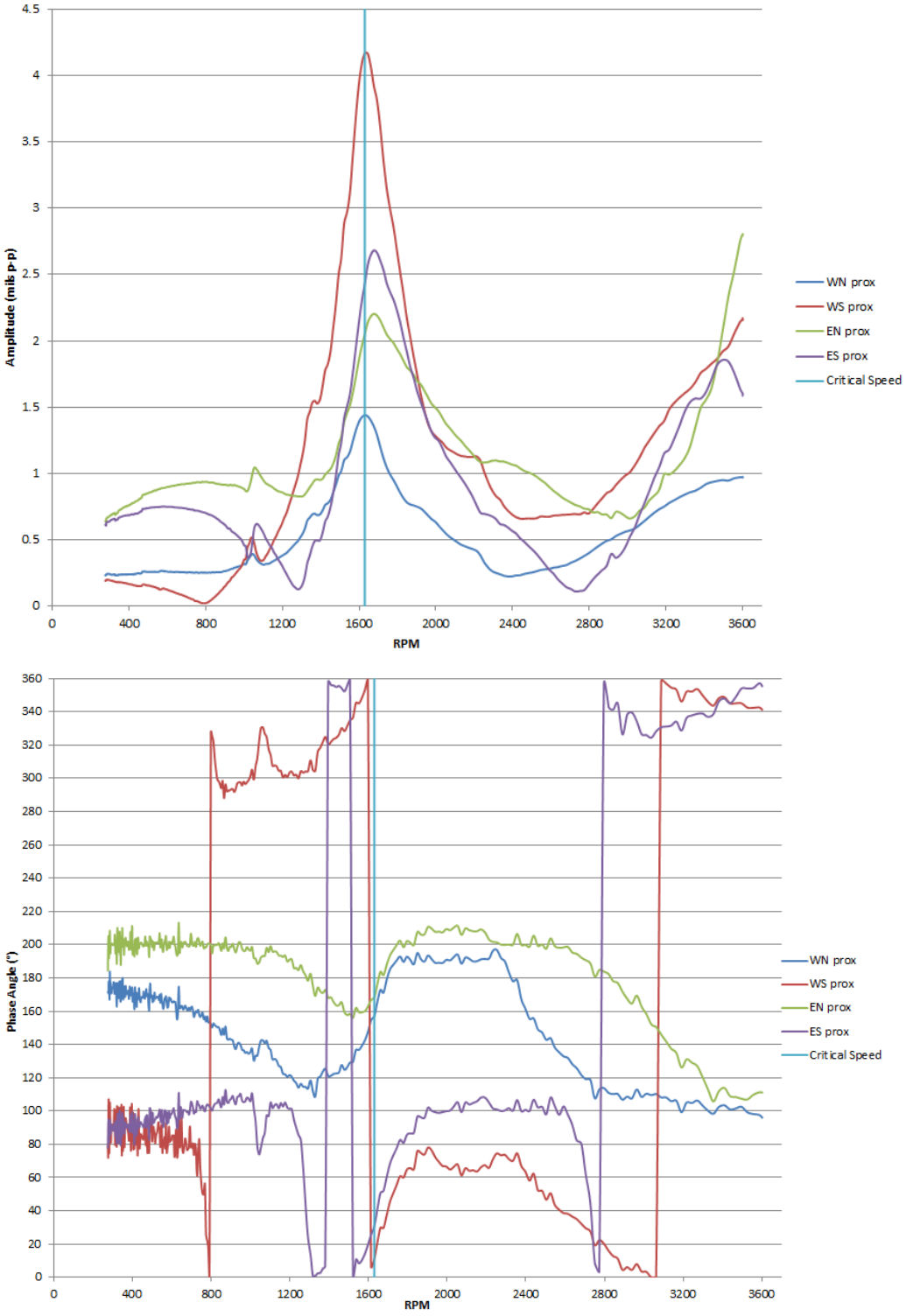

Figure 65 – Sleeve Bearing Checkout Coastdown Bode Plot

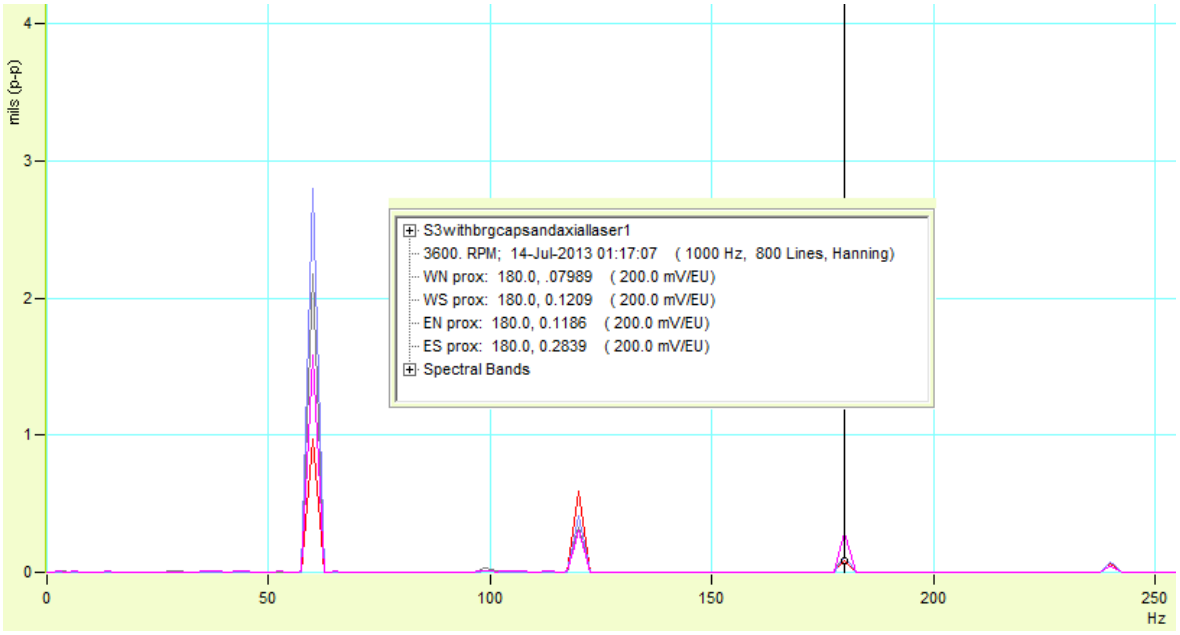

Figure 66– Sleeve Bearing Checkout Coastdown 3600 RPM Spectrum Plot

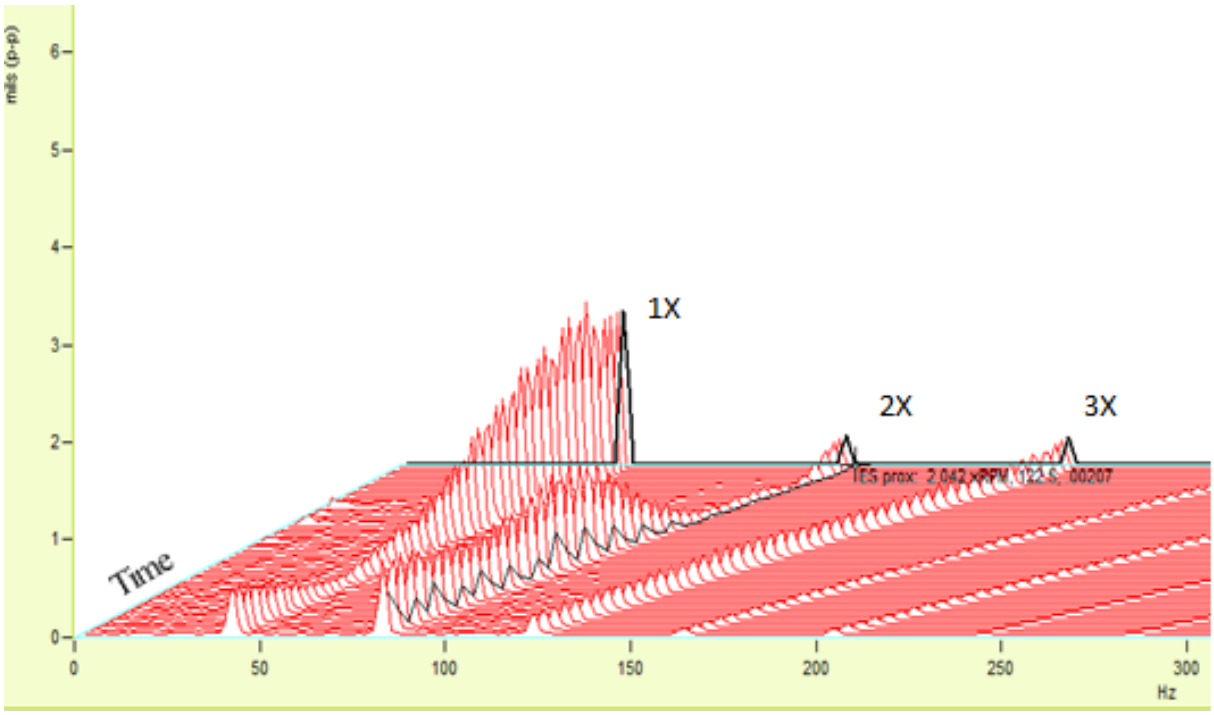

Figure 67 – Sleeve Bearing Checkout Coastdown Waterfall Plot 3600 RPM – ES Prox

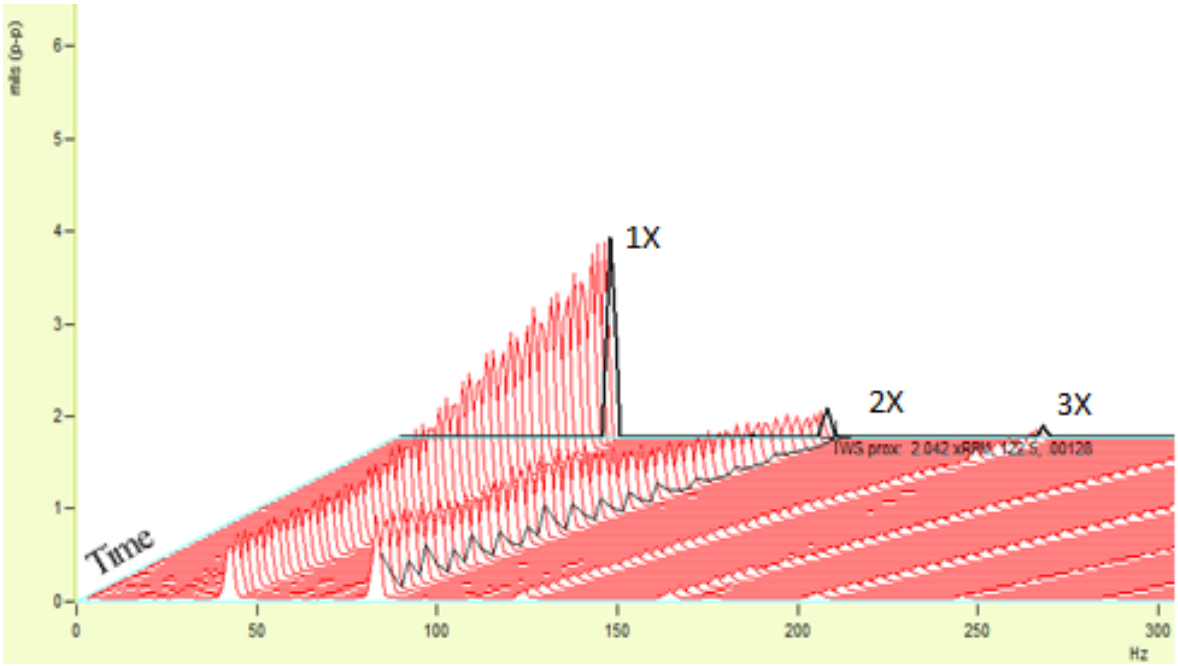

Figure 68 – Sleeve Bearing Checkout Coastdown Waterfall Plot 3600 RPM – WS Prox

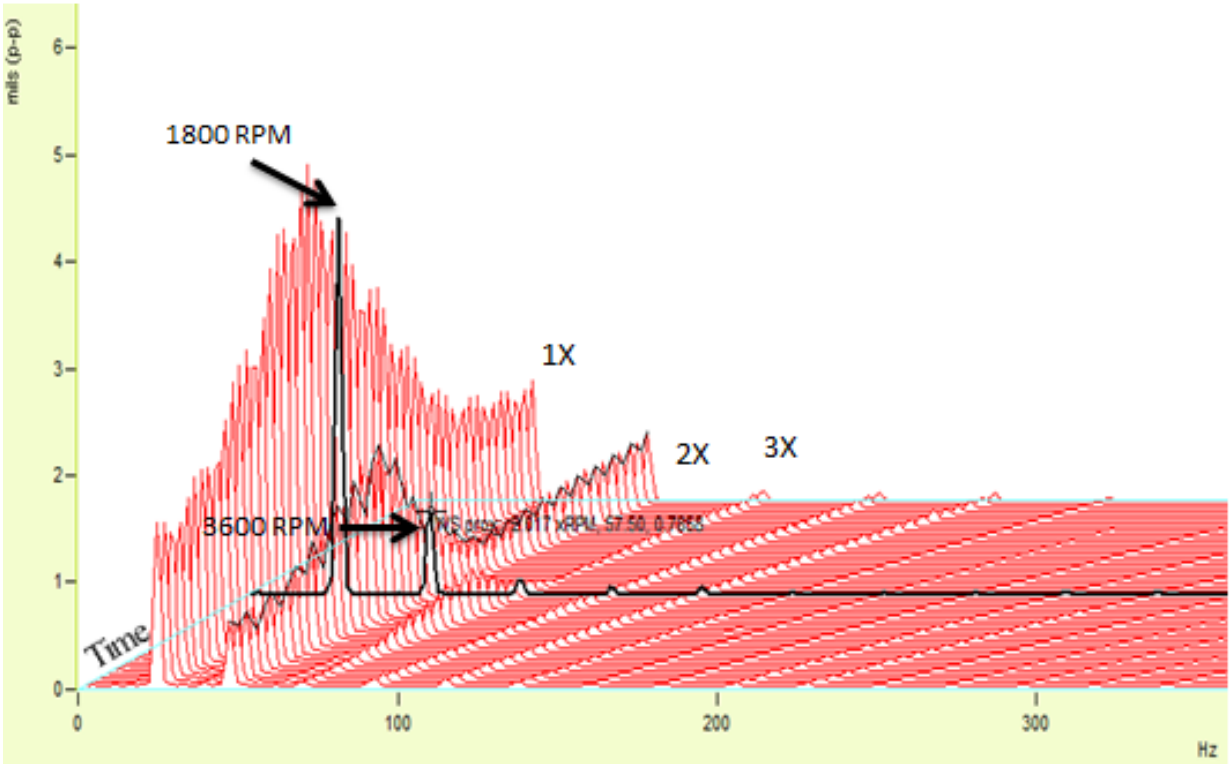

Figure 69 – Sleeve Bearing Coastdown First Critical Speed Waterfall Plot 1800 RPM – WS Prox

5.0 Conclusions

5.1 Comparative Analysis of Model and Experimental Data

From the results shown in Chapter 3.0 and Chapter 4.0, both models predict the first critical speed to occur between 1500-1700 RPM. As the experimental data is only taken up to 3600 RPM, the exact location of the second critical speed is unknown, but from the model an estimate of around 3700-3800 RPM is to be expected. Data showing the excitation of the 2X vibration spectra would indicate a critical speed in the range of 3800-4200 RPM, however. The switch from a pressure dam to sleeve bearing in the east bearing location did not greatly affect the location of these natural frequencies. The harmonic resonances indicated by the vibration spectra do seem to confirm the models prediction of a second critical speed near the motor operational speed.

While the vibration amplitudes shown in the model differ than that taken in the field, that is because the actual unbalance and unbalance locations of the rotor is not precise or calculable. The methods used from the API RP 684 [13] simply intends to represent the worst case unbalance for a rotor fresh from the shop. Comparing Figure 40 to Figure 52, or Figure 50 to Figure 60, the response at the first critical is worse in the field than predicted from the model unbalance response. Since real data for the second critical is not given, it is unknown whether the actual second critical response would match the predicted amplitude of the model.

Regardless, the effects of the second critical speed are already infringing upon the operation of the rotor at 3600 RPM, and the change in bearings does nothing to impact that result. From this test, the sleeve bearing will be kept in the east bearing housing and another sleeve bearing will be installed in the west bearing housing. The sleeve bearing is successful in dampening the vibration amplitude in the east bearing. This result is confirmed in both experimental and model data.

5.2 Future Work

While the model results appear to closely align with experimental data, several known deficiencies exist in the model that should be used to further refine the model for future efforts. First, foundational effects, or flexible bearing supports, can be used to more accurately predict the location of lateral critical speeds. Second, due to the inherent construction of the rotor, the rotor contains differing horizontal and vertical stiffnesses. These differing stiffnesses were seen in the coast down tests performed in Section 4.2, as the split critical speeds were apparent.

To truly represent the effects of the different stiffnesses, a finite element analysis of the rotor with the core and rotor end windings including retaining rings and centering rings will be required. The copper windings effects on the stiffness of the rotor were neglected in this analysis but should be included in the finite element analysis. Also, one of the primary influences of the second critical amplitude is the kinetic energy resulting from the couplings. Future work will attempt to balance out the second critical amplitude by using the coupling as a balance plane. Other balance planes will require removing the rotor from the stator and balancing in a high-speed pit to access the balance planes at the centering rings.

Finally, this study did not accomplish it's original task, i.e., shifting the critical speed away from running speed. Something more drastic may be required to accomplish this goal, and future studies will investigate these options. Tilting-pad bearings may be studied to determine if they can successfully shift the second critical speed. Stiffening the bearing supports, which will be included in future work, may succeed in doing this. Otherwise, performing a redesign of the rotor including, but not limited to, reducing the bearing length, stiffening the rotor, or adding rotor mass may be required.

5.3 Final Discussion

This study has confirmed prior studies performed regarding the operation of VKF motors near the second critical speed. Using DyRoBeS© software, the rotor was modeled and several lateral rotordynamic analyses were performed. Using these results, the bearing change was performed and data recorded before and after the bearing was changed. The results of the motor checkouts confirmed what the model indicated, namely, that while the bearing switch may successfully reduce vibration amplitude, it does not shift the rotor operation away from the critical speed.

An expected separation margin of 10-15% (360-540 RPM) from the critical is typical for most rotor designs [13]. Data indicated that the critical speed was occurring in the 3800-4200 RPM range, proven by looking at the 2X vibration spectra. If the second critical speed is occurring at 3800 RPM, the separation margin of the actual system is only 6%. If the second critical speed is occurring at 4200 RPM, the separation margin is 16%. Due to data that indicates that the rotor is already infringing on and seeing the effects of operation near the second critical speed, the conclusion is that the rotor-bearing system is operating too close to the second critical speed.

With that being said, the sleeve bearing will be kept and another sleeve bearing installed in the west bearing location due to the lower vibration amplitudes. Further work such as that detailed in Section 5.2 will attempt to determine other methods of shifting the critical speed away from the operating speed. In the meantime, the effects of the second critical speed will be a constant nuisance in the operation of the motor. As the rotor ages, the stiffness of the rotor-bearing system will change. The resulting critical speed may shift slightly, resulting in the critical speed occurring at the operating speed of the rotor. Therefore, to ensure reliable operation of the motor, further work is necessary. Continued investigations into other possible changes will be made and implemented if the model indicates a promising path.

Rotordynamic analyses have greatly improved over the past 160 years. Tools exist currently that did not when these motors were designed in the 1950's. Using these tools allow the analyst to gain in hours knowledge of a machine that only testing provided in the past. Considering the many years of service these machines have provided thus far as an integral part of furthering aerodynamic knowledge at the von Karman Gas Dynamic Facility wind tunnels, maintaining these machines so they provide reliable service is vitally important. Any improvements which can be made in accomplishing this goal are worth pursuing, as this study achieved.

Bibliography

[1] "The Von Karman Gas Dynamics Facility Wind Tunnels". *Arnold Air Force Base*. http://www.arnold.af.mil/library/factsheets/factsheet.asp?id=12974. Accessed: 12 Jan 2014.

[2] "G10 FR4 Materials". *CrossNail Laminates and Plastics*. http://www.g10fr4.com/index.htm. Accessed: 15 Jan 2014.

[3] "Turbogenerator Rewinds a Specialty". *National Electric Coil*. http://www.national-electric-coil.com/TGRtr.html#Rewind. Accessed: 15 Jan 2014.

[4] "How to make a Frame 5 generator "new" in 15 easy steps". *Combined Cycle Journal*. http://www.ccj-online.com/3q-2012/how-to-make-a-frame-5-generator-new-in-15-easy-steps/. Accessed: 16 Jan 2014.

[5] Moore, B. and Hollandsworth, D. "Generator Rotor Thermal Sensitivity: Causes and Cures". Proceedings of the Iris Rotating Machinery Conference, June 2010.

[6] "Features: DyRoBeS© 4-in-1 Advantage." *Rodyn Vibration Analysis, Inc.* http://rodyn.com/dyrobes/features/. Accessed: 16 Jan 2014.

[7] Rankine, W.J. "On the Centrifugal Force of Rotating Shafts". *Engineer*. Vol. 27. 1869. P. 249

[8] Vance, J.M. "Rotordynamics and the KGB." *Vavco*. http://www.vavco.com/KGB_2011.pdf. Accessed: 21 Jan 2014.

[9] Dunkerley, S. "On the Whirling of Vibration of Shafts." *Phil. Trans. Roy. Soc.* Series A, Vol. 185. 1894. p. 279. https://archive.org/details/philtrans08637228. Accessed: 21 Jan 2014.

[10] Foppel, A. "Vorlesungen uber die technishe Mechanik." *Der Civilingenieur*, Vol. 4. 1895. P. 216.

[11] Kerr, W. "On the Whirling Speeds of Loaded Shafts." *Engineer*. 18 Feb 1916. Print.

[12] Jeffcott, H.H. “On the Lateral Vibration of Loaded Shafts in the Neighbourhood of a Whirling Speed.” *Philosophical Magazine*. June 1919: 304-314. Print.

[13] *API Standards Paragraphs Rotordynamic Tutorial: Lateral Critical Speeds, Unbalance Response, Stability, Train Torsionals, and Rotor Balancing*. API Recommended Practice 684. 2005. Accessed: 24 Jan 2014.

[14] Chen, W.J., and Gunter, E.J. *Introduction to Dynamics of Rotor-Bearing Systems*. Eigen Technologies, Inc. 2005.

[15] Stodola, A. *Steam Turbines with an Appendix on Gas Turbines and the Future of Heat Engines*. D. Van Nostrand Company. New York, New York. 1924.

[16] Kimball, A.L. Jr. “Internal Friction Theory of Shaft Whirling” General Electric Review, Vol 27. 1924: 244-251. Print.

[17] Newkirk, B.L. and Taylor, H.D. “Shaft Whipping due to Oil Action in Journal Bearings.” *General Electric Review*. 28:559-568, 1925.

[18] Smith, D.M. “The motion of a rotor carried by a flexible shaft in flexible bearings.” *Proceedings of the Royal Society (London) A*, 142:92-118. 1933.

[19] Muszynska, A. *Rotordynamics.* CRC Press. Boca Raton, Florida. 2005.

[20] Prohl, M.A., “A General Method for Calculating Critical Speeds of Flexible Rotors.” *Journal of Applied Mechanics.* September 1945:A-142-A-148.

[21] Myklestad, N.O., “A New Method of Calculating Natural Modes of Uncoupled Bending Vibration of Airplane Wings and Other Types of Beams.” *Journal of the Aeronautical Sciences*. April 1944: 153-162.

[22] Vance, J.M. *Rotordynamics of Turbomachinery.* John Wiley & Sons. New York, New York. 1988.

[23] Lund, J.W. “Spring and Damping Coefficients for the Tilting Pad Journal Bearing.” *ASLE Transactions,* 7, 1964: 342-352.

[24] Lund, J.W. “Rotor-Bearing Dynamics Design Technology Part III: Design Handbook for Fluid Film Type Bearings.” Air Force Aero Propulsion Laboratory, Wright Patterson AFB, OH. Technical Report AFAPL-TR-65-45. AD466932. May 1965.

[25] Lund, J.W. *Self-Excited, Stationary Whirl Orbits of a Journal in a Sleeve Bearing*. Dissertation. Rensselaer Polytechnic Institute. 1966.

[26] Lund, J.W. and Orcutt, F.K. “Calculation and Experiments on the Unbalance Response of a Flexible Rotor.” *Trans. ASME, J. Eng. Ind.*, 89(4), 1967: 785-795.

[27] Lund, J.W. “Stability and Damped Critical Speed of a Flexible Rotor in Fluid-Film Bearings.” *Trans. ASME, J. Eng. Ind.,* 96(2), 1974:509-517.

[28] Lund, J.W. “Review of the Concept of Dynamic Coefficients for Fluid Film Journal Bearings.” *Journal of Tribology*, 109, 1987:37-41.

[29] Gunter, E.J. “Dynamic Stability of Rotor-Bearing Systems.” NASA paper No. SP-113,29. 1966.

[30] Gunter, E.J. and Choudhury, P.D. “Rigid Rotor Dynamics.” NASA paper CR-1391. 1969.

[31] Gunter, E.J. “Rotor-Bearing Stability.” *Proceedings from the 1st Turbomachinery Symposium at College Station, TX, 1972*. College Station, TX. 1972.

[32] Gunter, E.J., Barrett, L.E., and Allaire, P.E. “Balancing of Flexible Multi-Mass Flexible Rotors.” *Proceedings from the 5th Turbomachinery Symposium at College Station, TX, 1976*. College Station, TX. 1976.

[33] Gunter, E.J. “Optimum Bearing and Support Damping for Unbalance Response and Stability of Rotating Machinery.” *Trans. ASME, J. Eng. Pow.*, 100, 1978: 89-94.

[34] Gunter, E. J., Barrett, L.E., and Choy, K.C. “Dynamic Analysis of Flexible Rotor-Bearing Systems Using a Modal Approach.” NASA paper CR-157781. 1978.

[35] Ruhl, R.L., and Booker, J.F. “A Finite Element Model for Distributed Parameter Turborotor Systems.” *Trans. ASME, J. Eng. Ind.,* 94(1), 1972: 126-132.

[36] Nelson, F.C. and McVaugh, J.M. “The Dynamics of Rotor Bearing Systems Using Finite Elements.” *Trans. ASME, J. Eng. Ind.,* 98(2), 1976:593-600.

[37] Nicholas, J.C. *A Finite-Element Dynamic Analysis of Pressure Dam and Tilting Pad Bearings*. Dissertation. University of Virginia. 1977.

[38] Nicholas, J.C., and Moll, R.W. ”Shifting Critical Speeds Out of the Operating Range by Switching From Tilting Pad to Sleeve Bearings.” *Proceedings from the 22nd Turbomachinery Symposium at College Station, TX, 1993.* College Station, TX, 1993.

[39] Nicholas, J.C., “Stabilizing Turbomachinery with Pressure Dam Bearings.” *Encyclopedia of Fluid Mechanics, Vol. 2: Dynamics of Single-Fluid Flows and Mixing*. Gulf Publishing Company. Houston, TX. 1994.

[40] Nicholas, J.C. “Hydrodynamic Journal Bearings – Types, Characteristics, and Applications.” Rotating Machinery, Inc. 1996.

[41] Nicholas, J.C. Whalen, J.K., and Franklin, S.D. “Improving Critical Speed Calculations Using Flexible Bearing Support FRF Compliance Data.” *Proceedings from the 15th Turbomachinery Symposium at College Station, TX, 1985.* College Station, TX, 1985.

[42] Rao, J.S. *Rotordynamics*. John Wiley & Son, Inc., New York, NY. 1991.

[43] Childs, D. *Turbomachinery Rotordynamics: Phenomena, Modeling, & Analysis*. John Wiley & Sons, New York, NY, 1993.

[44] *Turbomachinery Laboratory*. Texas A&M Engineering Experiment Station, 2013. Web. 2 Feb 2014. http://turbolab.tamu.edu/.

[45] *Rotor Dynamics Lab*. Virginia Tech, 2013. Web. 2 Feb 2014. http://www.rotorlab.me.vt.edu/.

[46] Allaire, P.E., and Flack, R.D. "Design of Journal Bearings for Rotating Machinery." *Proceedings from the 10th Annual Turbomachinery Symposium at College Station, TX, 1981*. College Station, TX. 1981.

[47] Leader, M.E. "Understanding Journal Bearings." *Proceedings from the 25th Annual Vibration Institute Meeting at Willowbrook, IL, 2001.* Willowbrook, IL,2001.

[48] Zeidan, F.Y., and Herbage, B.S. "Fluid Film Bearing Fundamentals and Failure Analysis." *Proceedings from the 20th Turbomachinery Symposium at College Station, TX, 1991.* College Station, TX, 1991.

[49] He, M., Cloud, C.H., and Byrne, J.M., "Fundamentals of Fluid Film Journal Bearing Operation and Modeling." *Proceedings from the 34th Turbomachinery Symposium at College Station, TX, 2005.* College Station TX, 2005.

[50] San Andrès, L. "Hydrodynamic Fluid Film Bearings and Their Effect on the Stability of Rotating Machinery." *Design and Analysis of High Speed Pumps* (pp.10-1 – 10.36). Educational Notes RTO-EN-AVT-143, Paper 10. Neuilly-sur-Seine, France.

[51] Kirk, R.G., and Guo, Z. "Instability Boundary for Rotor-Hydrodynamic Bearing Systems, Part 1: Jeffcott Rotor with External Damping." *Trans. ASME, J. Vib. Aco.*, 125(4). 2003: 417-422.

[52] Kirk, R.G., and Guo, Z. "Instability Boundary for Rotor-Hydrodynamic Bearing Systems, Part 2: Rotor with External Flexible Damped Support." *Trans. ASME, J. Vib. Aco.*, 125(4). 2003: 423-426.

[53] Kirk, R.G. "Lund's Elliptic Orbit Forced Response Analysis: The Keystone of Modern Rotating

Machinery Analysis." *Trans. ASME, J. Vib. Aco.*, 125(4). 2003: 455-461.

[54] Mirro, J. "Practical Applications of Rotordynamics, Bearing Design, Mechanical Analysis, and Vibration Diagnostics to Design Problems of Rotating Machinery in Operation." *Proceedings from the 18th Turbomachinery Symposium at College Station, TX, 1989*. College Station, TX, 1989.

[55] Greybeal, T.D. "The Nature of Vibration in Electric Machinery." *Electrical Engineering*, 63. 1944: 712-718.

[56] Jordan, M.A. "What are Orbit plots, anyway?". *Orbit*, Dec 1993: 8-15.

[57] Harnoy, A. "Bearing Design in Machinery: Engineering Tribology and Lubrication." *Marcel Dekker, Inc.* New York, New York. 2003.

[58] Ding, W. *Self-Excited Vibration: Theory, Paradigms, and Research Methods*. Tsinghau University Press, Beijing, China. 2012.

[59] "IOtech eZ-Series" *National Instruments*. http://sine.ni.com/nips/cds/view/p/lang/en/nid/208342. Accessed: 16 Feb 2014.

[60] "Machinery Fault Diagnosis" *Ludeca*, *Inc*. 2011. http://www.ludeca.com/brochures/Ludeca_Machinery-Fault-Diagnosis-Guide.pdf. Accessed: 28 Feb. 2014

[61] Greenhill, L.M., and Cornejo, G.A. "Critical Speeds Resulting from Unbalance Excitation of Backward Whirl Modes" *ASME Design Engineering Technical Conferences Vol. 3 – Part B*, 84(2), 1995: 991-999.

[62] Quarteroni, A., Sacco, R., and Saleri, F. *Numerical Mathematics*. Springer Berlin Heidelberg, Heidelberg, Baden-Württemberg. 2007.

Appendices

Appendix I: Bearing Equations of Motion and Finite Element Solution

Bearing Equations of Motion

The continuity equation is derived from the conservation of mass principle. For an incompressible fluid, the continuity equation is as follows for steady state operation, with a note that for all equations, all variables are held constant except the one being used in the differentiation:

$$\frac{\partial u}{\partial x}+\frac{\partial v}{\partial y}+\frac{\partial w}{\partial z}=0 \tag{I.1}$$

Because hydrodynamic lubrication involves thin-film flow, the fluid inertia and body forces are very small compared to the viscous forces. Therefore, the inertial forces and body forces X, Y, and Z can be disregarded. For a Newtonian, incompressible fluid with constant viscosity in Cartesian coordinates, the Navier-Stokes equations with the inertial terms neglected are

$$\frac{\partial p}{\partial x}=\mu(\frac{\partial^2 u}{\partial x^2}+\frac{\partial^2 u}{\partial y^2}+\frac{\partial^2 u}{\partial z^2}) \tag{I.2}$$

$$\frac{\partial p}{\partial y}=\mu(\frac{\partial^2 v}{\partial x^2}+\frac{\partial^2 v}{\partial y^2}+\frac{\partial^2 v}{\partial z^2}) \tag{I.3}$$

$$\frac{\partial p}{\partial y}=\mu(\frac{\partial^2 w}{\partial x^2}+\frac{\partial^2 w}{\partial y^2}+\frac{\partial^2 w}{\partial z^2}) \tag{I.4}$$

Combining these equations with the continuity equation yields the Reynolds equation, the governing equation for pressure distribution in a fluid film bearing. The Reynolds equation for journal bearings with incompressible turbulent flow is

$$\frac{\partial}{\partial x}\left(G_x\frac{h^3}{\mu}\frac{\partial p}{\partial x}\right)+\frac{\partial}{\partial y}\left(G_y\frac{h^3}{\mu}\frac{\partial p}{\partial y}\right)=\frac{U}{2}\frac{\partial h}{\partial x} \tag{I.5}$$

The U component is the surface velocity. G_x and G_y are the turbulent flow coefficients, which are equal to 1/12 for laminar flow coefficients and for turbulent flow regimes [14].

$$\frac{1}{G_x} = 12 + 0.0136Re^{0.9} \quad \text{(I.6)}$$

$$\frac{1}{G_y} = 12 + 0.0043Re^{0.96} \quad \text{(I.7)}$$

The viscous shearing created by the rotating journal acting on the film generates heat. Including temperature effects in the bearing model is essential for ensuring the model is accurate. The temperature effects can be solved from the governing energy equation, derived from the conservation of energy principle. Due to the small film thickness, the energy equation for a typical bearing analysis is simplified. The three dimensional energy equation for laminar flow in a bearing is

$$\rho C_p \left(u\frac{\partial T}{\partial x} + v\frac{\partial T}{\partial y} + w\frac{\partial T}{\partial z}\right) = [\frac{\partial}{\partial x}\left(\kappa\frac{\partial T}{\partial x}\right) + \frac{\partial}{\partial y}\left(\kappa\frac{\partial T}{\partial y}\right) + \frac{\partial}{\partial z}\left(\kappa\frac{\partial T}{\partial z}\right)] + \mu[\left(\frac{\partial u}{\partial y}\right)^2 + \left(\frac{\partial w}{\partial y}\right)^2] \quad \text{(I.8)}$$

As shown from this equation, the steady-state temperature is determined by three terms. The first term on the left hand side of the equation is the heat convection term which describes the heat transfer due to the lubricant's motion. The second term, the first on the right-hand side, is the heat conduction term. This determines the heat transfer between the lubricant and the surrounding surfaces. The third and final term is the heat dissipation term. The dissipation term describes the internal heat generation due to viscous shearing, and is proportional to the lubricant viscosity. Dimensional analysis on the three terms shows that the convection term is much larger than the conduction term. This shows that the film itself is a heat source; although some of the heat is conducted away through the solid surfaces, most of it is carried away by the oil [49].

In most algorithms, the Navier-Stokes equations are solved using an assumed lubricant viscosity. After the pressure distribution is calculated, the velocity components are derived and the energy equation is solved to give the temperature distribution. From the temperature distribution, a viscosity is calculated and the process is iterated until the difference between iterations is sufficiently small. After

the steady state journal position is established, the dynamic coefficients of the bearing can be calculated. By perturbing the journal position, stiffness coefficients can be calculated by using the force variation at the new journal position. Damping coefficients can be calculated in the same manner using velocity perturbations. Since a fixed geometry bearing only has two degrees of freedom, the journal translation in the X and Y direction, there are eight dynamic coefficients. Figure 70 shows these coefficients as modeled using a basic sleeve bearing [49].

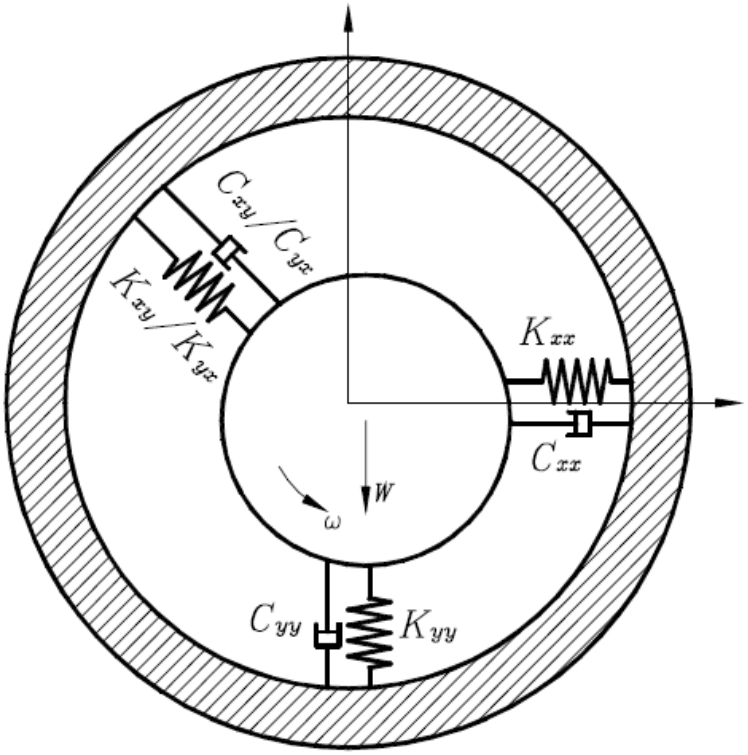

Figure 70 – Journal Bearing Fluid Film Model

Continuing the process, the bearing forces acting on the rotor can be expressed by the following Taylor's expansion, with the static forces at x_0 and y_0 equal to the external load of the rotor:

$$\begin{Bmatrix} F_x \\ F_y \end{Bmatrix} = \begin{Bmatrix} -W_x \\ -W_y \end{Bmatrix} - \begin{bmatrix} k_{xx} & k_{xy} \\ k_{yx} & k_{yy} \end{bmatrix} \begin{Bmatrix} x \\ y \end{Bmatrix} - \begin{bmatrix} c_{xx} & c_{xy} \\ c_{yx} & c_{yy} \end{bmatrix} \begin{Bmatrix} \dot{x} \\ \dot{y} \end{Bmatrix} \quad \text{(I.9)}$$

The cross-coupled damping coefficients, c_{xy} and c_{yx}, are equal. Under dynamic conditions, the journal center oscillates around the static equilibrium position as shown in the freebody diagram shown sketched in Figure 71 [14]. Please note that Figure 71 uses Lund's axis convention, wherein the Y axis is horizontal and the X-axis is vertical. This notation is not used for this paper except where noted.

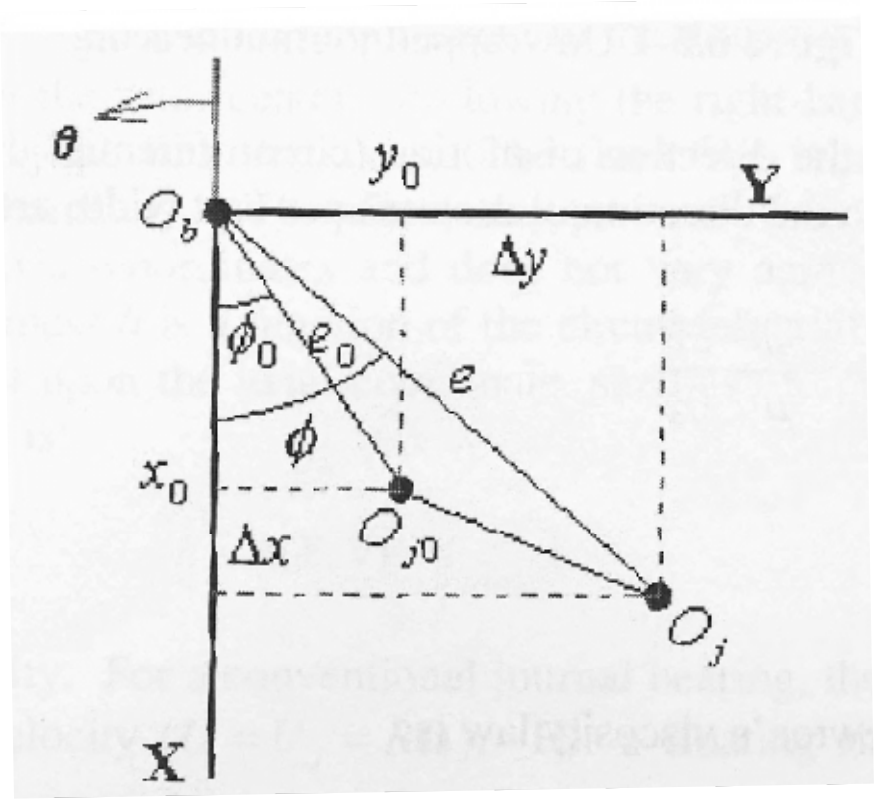

Figure 71 – Journal Static and Dynamic Position

Assuming these oscillations or vibrations are small, the film thickness and pressure equations become (with Equation I.10 showing the original film thickness equation for a sleeve bearing and the Eqs I.11 and I.12 showing the perturbed film thickness/pressure equations):

$$h = C + ecos(\theta_h - \varphi) = C + xcos\theta + ysin\theta \tag{I.10}$$

$$h = h_0 + \Delta h = h_0 + \left(\Delta x + z\Delta\theta_y\right)cos\theta + (\Delta y - z\Delta\theta_x)sin\theta \tag{I.11}$$

$$p = p_0 + p_x\Delta x + p_y\Delta y + p_{\dot{x}}\Delta\dot{x} + p_{\theta_x}\Delta\theta_x + p_{\theta_y}\Delta\theta_y + p_{\dot{\theta}_x}\Delta\dot{\theta_x} + p_{\dot{\theta}_y}\Delta\dot{\theta_y} \tag{I.12}$$

In equation I.10, θ is the angle from the line of centers between the bearing center and the journal center to where the film thickness h is being measured. The various p coefficients are the differentials of the pressure with respect to changes in x, y, θ_x, θ_y, $\dot{x}$, $\dot{y}$, $\dot{\theta}_x$, and $\dot{\theta}_y$. Each derivative is evaluated at the static equilibrium condition. As shown in Equation I.9, the fluid film forces can be written as a function of the stiffness and damping coefficients. To obtain these coefficients, you can integrate the pressure distribution to solve for the fluid film forces,

$$\begin{Bmatrix} F_x \\ F_y \end{Bmatrix} = \sum_{i=1}^{Npad} \int_0^L \int_{\theta_1}^{\theta_2} P \begin{Bmatrix} cos\theta \\ sin\theta \end{Bmatrix} dxdy \tag{I.13}$$

In this equation θ_1 and θ_2 are the leading and trailing edge of the pressure film. Npad is the number of individual pads; for a sleeve bearing, that number is equal to one. The pressure dam bearing has two pads, the upper and lower pad. By substituting the perturbed pressure equation into the fluid film force equation, the bearing dynamic coefficients can be calculated by relating them to the pressure derivatives.

$$\begin{Bmatrix} k_{xx} \\ k_{yx} \end{Bmatrix} = \sum_{i=1}^{Npad} \int_0^L \int_{\theta_1}^{\theta_2} -P_x \begin{Bmatrix} cos\theta \\ sin\theta \end{Bmatrix} dxdy \tag{I.14}$$

$$\begin{Bmatrix} k_{xy} \\ k_{yy} \end{Bmatrix} = \sum_{i=1}^{Npad} \int_0^L \int_{\theta_1}^{\theta_2} -P_y \begin{Bmatrix} cos\theta \\ sin\theta \end{Bmatrix} dxdy \tag{I.15}$$

$$\begin{Bmatrix} c_{xx} \\ c_{yx} \end{Bmatrix} = \sum_{i=1}^{Npad} \int_0^L \int_{\theta_1}^{\theta_2} -P_{\dot{x}} \begin{Bmatrix} cos\theta \\ sin\theta \end{Bmatrix} dxdy \tag{I.16}$$

$$\begin{Bmatrix} C_{xy} \\ c_{yy} \end{Bmatrix} = \sum_{i=1}^{Npad} \int_0^L \int_{\theta_1}^{\theta_2} -P_{\dot{y}} \begin{Bmatrix} cos\theta \\ sin\theta \end{Bmatrix} dxdy \tag{I.17}$$

Subsituting the perturbed pressure and film thickness expressions into the Reynolds equations yields five second-order partial differential equations with the requisite boundary conditions.

$$\frac{\partial}{\partial x}\left(G_x \frac{h_0^3}{\mu}\frac{\partial p_i}{\partial x} + f_i\right) + \frac{\partial}{\partial y}\left(G_y \frac{h_0^3}{\mu}\frac{\partial p_i}{\partial y} + g_i\right) = 0, i = 0, \Delta x, \Delta y, \Delta \dot{x}, \Delta \dot{y} \tag{I.18}$$

where

$$f_0 = -\frac{Uh_0}{2}, g_0 = 0 \tag{I.19}$$

$$f_{\Delta x} = \left(3\frac{G_x}{\mu}h_0^2\frac{\partial p_0}{\partial x} - \frac{U}{2}\right)cos\theta, g_{\Delta x} = \left(3\frac{G_y}{\mu}h_0^2\frac{\partial p_0}{\partial y}\right)cos\theta \tag{I.20}$$

$$f_{\Delta y} = \left(3\frac{G_x}{\mu}h_0^2\frac{d\partial_0}{\partial x} - \frac{U}{2}\right)sin\theta, g_{\Delta y} = \left(3\frac{G_y}{\mu}h_0^2\frac{\partial p_0}{\partial y}\right)sin\theta \tag{I.21}$$

$$f_{\Delta \dot{x}} = -R_b sin\theta, g_{\Delta \dot{x}} = 0 \tag{I.22}$$

$$f_{\Delta \dot{y}} = R_b cos\theta,\ g_{\Delta \dot{y}} = 0 \tag{I.23}$$

These five equations can be solved using a finite element approach, which will be described in the following section. The software DyRoBeS© uses the finite element approach to solve for the required bearing coefficients. It is desireable because the finite element method does not require the derivatives of the film thickness, so bearings with clearance discontinuities such as the pressure dam bearing used in this study can be solved. Also, turbulence effects can be included in the finite element method.

Bearing Finite Element Method

Bearings have been analyzed using a finite element approach since 1977, when Nicholas used the method to solve for pressure dam and tilt pad bearings [37]. The finite element method is a method of solving partial differential equations by numerical approximations. The system is discretized into

smaller parts, known as the mesh. Within each element, interpolation models are built which provide approximate expressions for the unknowns, such as the pressure distribution or temperature distribution. Equilibrium principles in variational form are applied to the various approximations within each element, forming elemental equilibrium equations. These equations are assembled into the global equilibrium equation, which is then solved using computer algorithms. These steps, with emphasis implicitly on the methods used in the DyRoBeS© software, will be described in the following paragraphs.

For sleeve or pressure dam bearings, the discretization of elements and the creation of meshes is not overly complex. The bearing is essentially unwrapped, and global coordinates x and y are used to describe the pressure distribution. The circumferential coordinate $x=R_b\theta$ ranges from 0 to 2π in the direction of shaft rotation. At 0 and 2π, a cyclic boundary condition is applied. The axial coordinate y ranges from 0 to L, the bearing length. Figure 72 [14] shows a general bearing grid for a typical sleeve bearing.

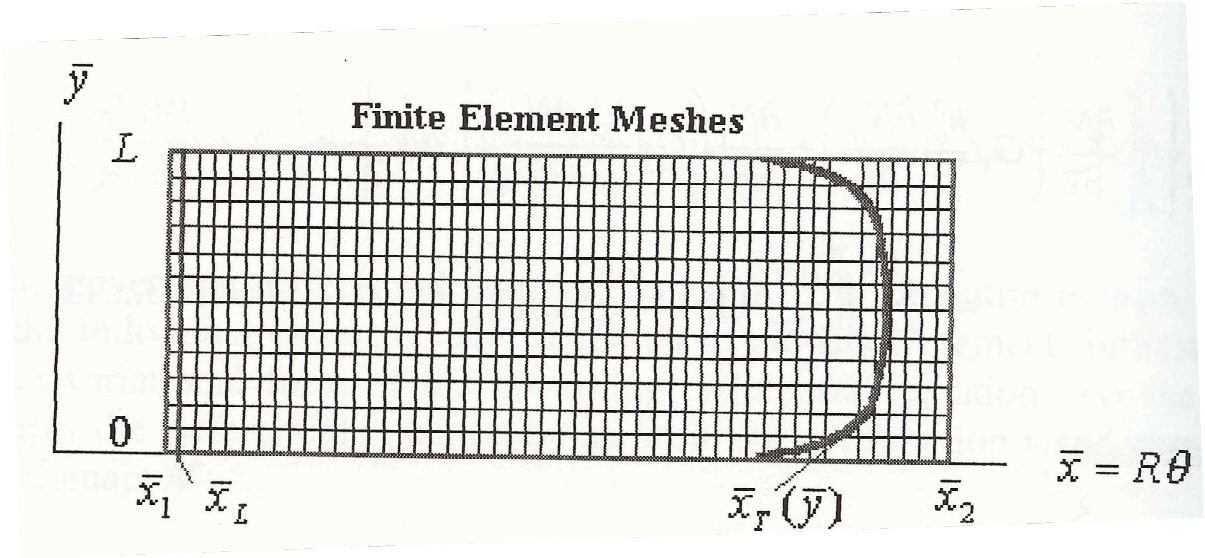

Figure 72 – Finite Element Mesh for Sleeve Bearing

Due to the simple geometry of the bearing, a rectangular element is often used. Each element contains four nodes, each numbered with the global coordinates x and y. For solving the pressure distributions of the bearing, pressure gradients at each node of each element are required for the solutions of perturbed pressures and calculation of the stiffness coefficients. Therefore, each node contains three degrees of freedom: the pressure at each node, and the pressure gradients in the x and y direction. For each finite element of four nodes, that results in 12 degrees of freedom, as shown in Figure 73 [14].

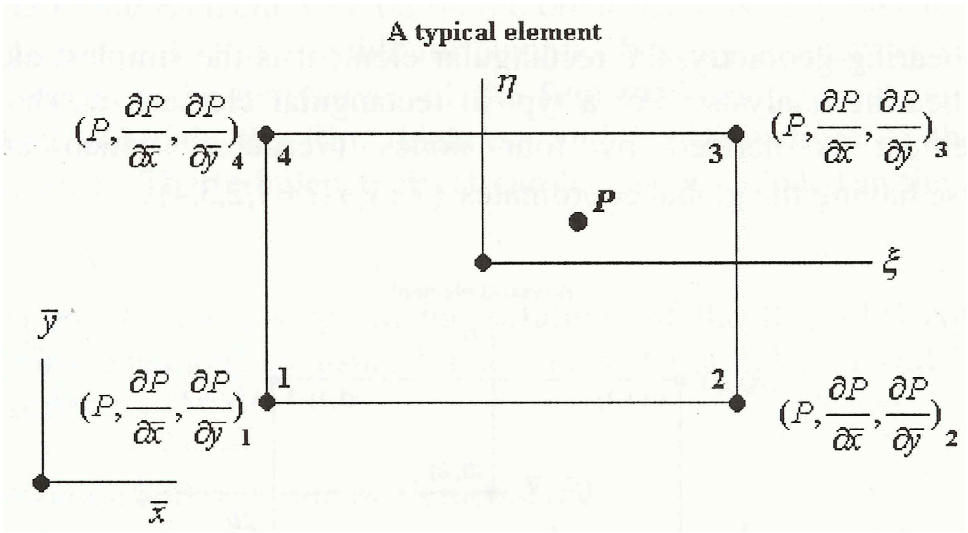

Figure 73 – Typical Finite Element in Bearing Model

Note that in Figure 73, the variables η and ξ are used to define a non-dimensional normalized coordinate system with the origin at the center of the element. The equations which define the relationship between the two coordinate systems are

$$\xi = \frac{x - x_c}{a}, \eta = \frac{y - y_c}{b} \tag{I.24}$$

where a and b is half the length of the horizontal and vertical side, respectively, as shown in Figure 73. It should be noted that it is desirable to create finer meshes at locations where the load is at or where

discontinuities occur, such as at the pressure dam step, while coarser meshes are acceptable for locations where pressure and load gradients are low and the bearing is unloaded.

The pressure distribution in the interior of an element is approximated using the following equation [14]:

$$P(x,y) = P(\xi,\eta) = \sum_{i=1}^{4}(N_i P_i + N_{4+i}\frac{\partial p_i}{\partial x} + N_{8+i}\frac{\partial p_i}{\partial y}) \quad \text{(I.25)}$$

where

$$N_i = \frac{1}{8}(\xi_0 + 1)(\eta_0 + 1)(2 + \xi_0 + \eta_0 - \xi^2 - \eta^2) \quad \text{(I.26)}$$

$$N_{4+i} = \frac{a}{8}\xi_i(\xi_0 + 1)^2(\xi_0 - 1)(\eta_0 + 1) \quad \text{(I.27)}$$

$$N_{8+i} = \frac{b}{8}\eta_i(\xi_0 + 1)(\eta_0 + 1)^2(\eta_0 - 1) \quad \text{(I.28)}$$

$$\xi_0 = \xi\xi_i,\ \eta_0 = \eta\eta_i \quad \text{(I.29)}$$

This can also be written in vector form,

$$P(x,y) = \sum_{j=1}^{12} N_j u_j \quad \text{(I.30)}$$

In vector form, u_j are the unknown nodal variables, i.e. the pressures and pressure gradients at each node. These are the variables which will be determined using the variational formulations shown next for obtaining the approximate element equations. DyRoBeS© uses Galerkin's method [14] to solve for bearing coefficients, as will be shown.

The five differential equations to be solved have the same form, as was shown in equation I.18. Since the equation is valid over the entire domain, it is also considered valid over each specific individual element. Therefore, the first step is constructing the variational form of the differential equation over

the element. As shown in the work by Chen and Gunter [14], the first step is to multiply the differential equation by an arbitrary test function v and integrate over the element domain, A^e:

$$\int v[\frac{\partial}{\partial x}\left(G_x \frac{h_0^3}{\mu}\frac{\partial p_i}{\partial x} + f_i\right) + \frac{\partial}{\partial y}\left(G_y \frac{h_0^3}{\mu}\frac{\partial p_i}{\partial y} + g_i\right)]\, dA^e = 0 \tag{I.31}$$

Using integration by parts and the gradient and divergence theorems, the integral can be written as

$$\int_{A^e} -\left\{\frac{\partial v}{\partial x}\left[\frac{\partial}{\partial x}\left(G_x \frac{h_0^3}{\mu}\frac{\partial p_i}{\partial x} + f_i\right) + \frac{\partial}{\partial y}\left(G_y \frac{h_0^3}{\mu}\frac{\partial p_i}{\partial y} + g_i\right)\right]\right\} dA^e \; + \tag{I.32}$$

$$\oint_{\Gamma^e}\left\{n_x\left(G_x \frac{h_0^3}{\mu}\frac{\partial p_i}{\partial x} + f_i\right) + n_y\left(G_y \frac{h_0^3}{\mu}\frac{\partial p_i}{\partial y} + g_i\right)\right\} ds = 0$$

For this equation, the arbitrary test function is chosen to be the interpolation function N_i. Placing the pressure distributions and test functions into variational form:

$$P_k(x,y) = \sum_{j=1}^{12} N_j u_{k,j}, \;\; \frac{\partial p_i}{\partial x} = \sum_{j=1}^{12} \frac{\partial N_j}{\partial x} u_{k,j}, \;\; \frac{\partial p_i}{\partial y} = \sum_{j=1}^{12} \frac{\partial N_j}{\partial y} u_{k,j} \tag{I.33}$$

$$\sum_{j=1}^{12}\left\{\int_{A^e}[\frac{\partial N_j}{\partial x}\left(G_x \frac{h_0^3}{\mu}\frac{\partial N_j}{\partial x}\right) + \frac{\partial N_i}{\partial y}\left(G_y \frac{h_0^3}{\mu}\frac{\partial N_j}{\partial y}\right)]\, dA^e\right\} u_{i,j} = -\sum_{j=1}^{12}\int_{A^e}[\frac{\partial N_i}{\partial x}(f_k) + \frac{\partial N_i}{\partial y}(g_k)]dA^e \tag{I.34}$$

This equation can be written simply in matrix form,

$$K^e u_k^e = F^e \tag{I.35}$$

The numerical integration is performed in the local coordinates and Gauss-Legendre quadratures are used in the element matrix and load vector. Each element equation holds for any element in the finite element mesh. Each element and its element equation can be assembled to form the global equation.The assembly equations can be shown in matrix form as:

$$\boldsymbol{Ku} = \boldsymbol{F} \tag{I.36}$$

This assembled equation requires the prerequisite boundary conditions in order to solve. For most bearings, similar boundary conditions apply. At the boundary along the axial direction (length) of the bearing, the pressure is assumed to be ambient, or zero. If the bearing is symmetric along the centerplane, the boundary condition at the centerplane can be shown that the pressure gradient at y=L/2 is zero. With regards to circumferential boundaries, cyclic boundary condition can be applied at x_1=0 and x_2=2π, that the pressure is equal to zero. For internal boundaries, like that seen in the pressure dam bearing, a special boundary condition must be applied at the oil film discontinuity. For the finite element approach, two nodes are assigned for the same physical node, as shown in Figure 74 [14]. Node i has thickness h_i and is a node for element I, while Node j has a film thickness of h_j and is a node for element J. While the pressure continuity is maintained across the step, the pressure gradients are different on either side of the step.

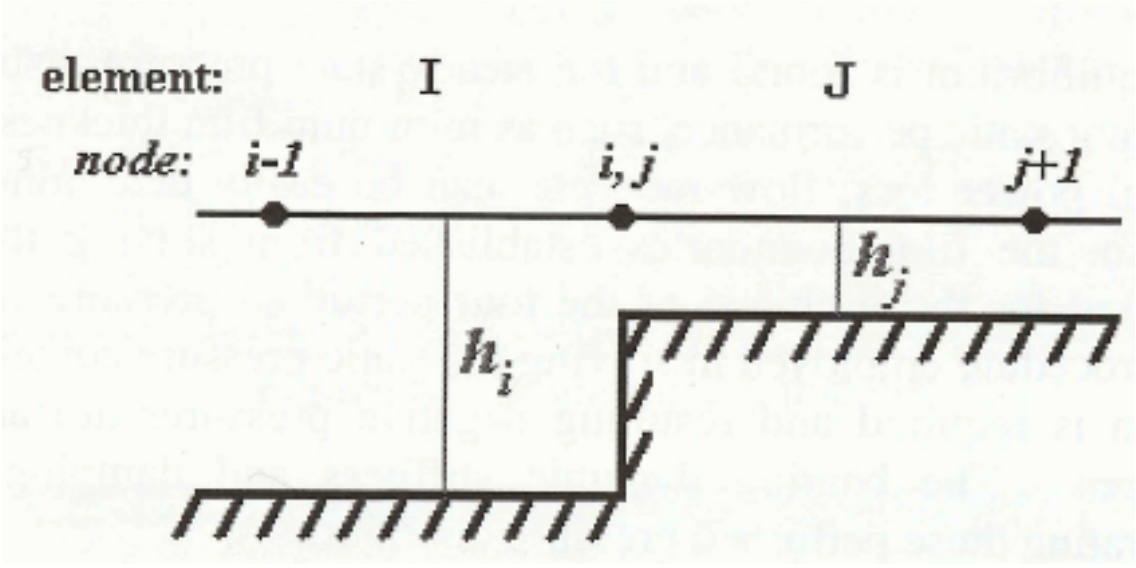

Figure 74 – Boundary Condition for Film Discontinuity

From the global equations with boundary conditions, the steady state pressure distribution P_0 can be calculated. The static forces on the journal are calculated from this pressure distribution. At static equilibrium, the forces acting on the journal are balanced, so the Reynolds equation is iteratively solved to determine the static equilibrium position. From this, the bearing static performance can be calculated.The film boundaries established from the bearing static performance are used in the solution of the four perturbed pressure equations. Integrating these equations leads to the bearing dynamic and damping coefficients.

Appendix II: Rotor-Bearing System Analysis

As discussed in Chapter 3, the rotor can be divided into multiple elements. Each element can be expressed by eight end-point displacements by specifying a spatial shape function shown by:

$$\begin{Bmatrix} x(s,t) \\ y(s,t) \\ \theta_x(s,t) \\ \theta_y(s,t) \end{Bmatrix} = \begin{bmatrix} \boldsymbol{\Psi}_T(s) \\ \boldsymbol{\Psi}_R(s) \end{bmatrix}_{4x8} \boldsymbol{q}^e(t)_{8x1} \tag{II.1}$$

where

$$\boldsymbol{q}^e = \left(x_1, y_1, \theta_{x1}, \theta_{y1} \middle| x_2, y_2, \theta_{x2}, \theta_{y2}\right)^T \tag{II.2}$$

The primary method used by DyRoBeS© to specify the shape functions is the Timoshenko Beam Theory [14]. According to Timoshenko Beam Theory, the translation of the element is described by an x and y displacement, with each displacement consisting of two parts: bending and shear deformation. The rotation of the element is described by two rotational angles, θ_x and θ_y. As shown in the text by Chen and Gunter [14], these shape functions can be shown to be equal to:

$$\boldsymbol{\Psi} = \begin{bmatrix} \boldsymbol{\Psi}_T(s) \\ \boldsymbol{\Psi}_R(s) \end{bmatrix} = \begin{bmatrix} N_1 & 0 & 0 & N_2 & N_3 & 0 & 0 & N_4 \\ 0 & N_1 & -N_2 & 0 & 0 & N_3 & -N_4 & 0 \\ 0 & -N_{r1} & N_{r2} & 0 & 0 & -N_{r3} & N_{r4} & 0 \\ N_{r1} & 0 & 0 & N_{r2} & N_{r3} & 0 & 0 & N_{r4} \end{bmatrix} \tag{II.3}$$

where N_i are the translational interpolation functions and N_{ri} are the rotational interpolation functions

$$N_i = \frac{1}{1+\Phi}(\alpha_i + \Phi\beta_i), i = 1,2,3,4 \tag{II.4}$$

$$\alpha_1 = 1 - 3\xi^2 + 2\xi^3, \beta_1 = 1 - \xi$$

$$\alpha_2 = L(\xi - 2\xi^2 + \xi^3), \beta_2 = \frac{L}{2}(\xi - \xi^2)$$

$$\alpha_3 = 3\xi^2 - 2\xi^3, \beta_3 = \xi$$

$$\alpha_4 = L(-\xi^2 + \xi^3), \beta_4 = \frac{L}{2}(-\xi + \xi^2)$$

$$N_{ri} = \frac{1}{1+\Phi}(\alpha_i + \Phi\beta_i), i = 1,2,3,4 \quad \text{(II.5)}$$

$$\alpha_1 = \frac{1}{L}(-6\xi + 6\xi^2), \beta_1 = 0$$

$$\alpha_2 = 1 - 4\xi + 3\xi^2, \beta_2 = 1 - \xi$$

$$\alpha_3 = \frac{1}{L}(6\xi - 6\xi^2), \beta_3 = 0$$

$$\alpha_4 = -2\xi + 3\xi^2, \beta_4 = \xi$$

and

$$\xi = \frac{s}{L}, \Phi = \frac{12EI}{kAGL^2} \quad \text{(II.6)}$$

Φ is known as the transverse shear effect parameter. This variable includes E, which is the Young's Modulus of the material, G, which is the shear modulus, I, the area moment of inertia, A, the cross sectional area of the element, and L, the element length. The symbol k represents the shape factor for the given element. For a cylindrical element, which will be the only one represented in this study, k is equal to

$$k = \frac{6(1+\nu)}{(7+6\nu)} \quad \text{(II.7)}$$

The Poissons ratio, ν, is the ratio of the transverse strain to axial strain which is a given for a specific material.

From these shape factors derived using Timoshenko Beam Theory,the kinetic and potential energy of the rotor element can be obtained, leading to the equation of motion for a given eight degree of freedom rotor element. The kinetic energy of a finite element is calculated by integrating the differential energy for an infinitesimal rotor element over the entire length of the element,

$$KE = \frac{1}{2}\int_0^L \left\{ m^e(\dot{x}^2 + \dot{y}^2) + I_d^e\left(\dot{\theta}_x{}^2 + \dot{\theta}_y{}^2\right) + \omega I_p^e(\dot{\theta}_x\theta_y - \theta_x\dot{\theta}_y)\right\} ds + \frac{1}{2}\omega^2 \int_0^L I_p^e ds \quad \text{(II.8)}$$

where m^e, I_p, and I_e are the mass, diametral, and polar moment of inertia per unit length. The shape functions can be substituted into this equation to form the matrix equation,

$$KE = \frac{1}{2}\dot{\boldsymbol{q}}^T(\boldsymbol{M}_T^e + \boldsymbol{M}_R^e)\dot{\boldsymbol{q}} + \boldsymbol{q}^T\omega\boldsymbol{g}^e\dot{\boldsymbol{q}} \quad \text{(II.9)}$$

where the element translational mass matrix, rotational inertia matrix, and gyroscopic matrix, respectively, are shown to be,

$$\boldsymbol{M}_T^e = \int_0^L \rho A \boldsymbol{\Psi}_T^T \boldsymbol{\Psi}_T \, ds \quad \text{(II.10)}$$

$$\boldsymbol{M}_R^e = \int_0^L \rho I \boldsymbol{\Psi}_R^T \boldsymbol{\Psi}_R \, ds \quad \text{(II.11)}$$

$$\boldsymbol{g}^e = -\frac{1}{2}\boldsymbol{G}^e = -\frac{1}{2}\int_0^L 2\rho I \boldsymbol{\Psi}_R^T \begin{bmatrix} 0 & 1 \\ -1 & 0 \end{bmatrix} \boldsymbol{\Psi}_R \, ds \quad \text{(II.12)}$$

The potential energy of the shaft represents the strain energy resulting from the elastic bending of the shaft from bending moments, shear energy caused by shear forces, and any work done from a constant axial load [14]. The potential energy is calculated in a similar method to kinetic energy by integrating an infinitesimal rotor element potential energy from each of the three aforementioned sources of strain energy over the length of the element. By substituting in the shape functions given in prior pages, the resulting potential energy is

$$PE = \frac{1}{2}\boldsymbol{q}^T\left(\boldsymbol{K}_b + \boldsymbol{K}_\beta + \boldsymbol{K}_a\right)\boldsymbol{q} \quad \text{(II.13)}$$

where each of the given **K** values represents the bending, shear, and axial force stiffness matrices

$$\boldsymbol{K}_b = \int_0^L EI(\boldsymbol{\Psi}_R')^T(\boldsymbol{\Psi}_R') \, ds \quad \text{(II.14)}$$

$$\boldsymbol{K}_{\beta} = \int_0^L kGA\left(\boldsymbol{\Psi}_T' + \begin{bmatrix} 0 & -1 \\ 1 & 0 \end{bmatrix}\boldsymbol{\Psi}_R\right)^T\left(\boldsymbol{\Psi}_T' + \begin{bmatrix} 0 & -1 \\ 1 & 0 \end{bmatrix}\boldsymbol{\Psi}_R\right) ds \tag{II.15}$$

$$\boldsymbol{K}_a = \int_0^L P(\boldsymbol{\Psi}_T')^T(\boldsymbol{\Psi}_T')\, ds \tag{II.16}$$

From the kinetic and potential energy equations, the resulting equation of motion for a cylindrical element can be determined. This equation assumes a constant cross-sectional area A and area moment of inertia, I, which is true for a cylindrical element.The equation of motion resulting from the energy equations are

$$(\boldsymbol{M}_T^e + \boldsymbol{M}_R^e)\ddot{\boldsymbol{q}}^e + \omega\boldsymbol{G}^e\dot{\boldsymbol{q}}^e + \boldsymbol{K}^e\boldsymbol{q}^e = \boldsymbol{Q}^e \tag{II.17}$$

Note that the individual elemental matrices **M**, **G**, and **K**, which have been repeatedly used in the previous text, are more fully defined in Appendix III.

Each element equation of motion is then assembled into a larger system equation of motion for the rotor-bearing system. Introducing the bearing stiffness and damping matrices into the system equation of motion results in the rotor-bearing system equation of motion,

$$\boldsymbol{M}\ddot{\boldsymbol{q}}(t) + (\boldsymbol{C}_b + \omega\boldsymbol{G})\dot{\boldsymbol{q}}(t) + (\boldsymbol{K}_s + \boldsymbol{K}_b)\boldsymbol{q}(t) = \boldsymbol{Q}(\dot{\boldsymbol{q}}, \boldsymbol{q}, \omega, t) \tag{II.18}$$

where **q** is the system displacement vector, showing the resulting vibration levels. Note this equation assumes a constant angular velocity. For a variable rotating speed, with □ as the angular displacement,

$$\boldsymbol{M}\ddot{\boldsymbol{q}}(t) + (\boldsymbol{C}_b + \dot{\varphi}\boldsymbol{G})\dot{\boldsymbol{q}}(t) + [(\boldsymbol{K}_s + \boldsymbol{K}_b) + \ddot{\varphi}\boldsymbol{G}]\boldsymbol{q}(t)$$

$$= \dot{\varphi}^2\boldsymbol{Q}_1(\varphi) + \ddot{\varphi}\boldsymbol{Q}_2(\varphi) + \boldsymbol{Q}_3(\dot{\boldsymbol{q}}, \boldsymbol{q}, \omega, t) \tag{11.19}$$

From equation II.18 to II.19, two main items are introduced, the circulatory matrix $\dot{\phi}$**G** and forcing function $\ddot{\varphi}\mathbf{Q}_2$. The circulatory matrix results from shear stress from the fluid film bearings. It is directly proportional to the viscosity of the oil film. It can be shown that if this force is much greater

than the stiffness and damping coefficients, oil whirl and whip will result [57]. The forcing functions are a result of any imbalance, misalignment, bowed rotor, or other harmonic forces which are used to study the response of a given rotor system to various effects.

From these equations of motion, the behavior of the dynamic rotor-bearing system can be described, including the critical speeds, stability analysis, steady state response, and transient response. The primary goal of this study is to determine the critical speeds of the rotor with two different bearing types, sleeve and pressure dam. The critical speeds for a rotor-bearing system can be found by reducing the problem to an eigenvalue problem and solving. From the API RP 684 [13], it is shown that damping typically has little effect on the frequency of the critical speeds, so an undamped analysis can be performed. Assuming the undamped rotor system has isotropic supports, the critical speed problem is solved using a reduced eigenvalue equation reduced to two planes of motion (XZ), that is,

$$\left(\boldsymbol{K}_{xz} - {\Omega_i}^2 \boldsymbol{M}_{xz}\right)\boldsymbol{y}_i = 0 \tag{II.20}$$

In this equation, $\mathbf{y}_i$ is the eigenvector or mode shape, while Ω_i are the related eigenvalues (i.e. natural frequencies or critical speeds). The stiffness and inertia matrices **K** and **M** can be assembled from the appropriate components including shaft elements, disks, bearings, or flexible supports.

$$\boldsymbol{K}_{xz} = \sum_{XZ} \boldsymbol{K}^e + \sum_{XZ} \boldsymbol{K}^d + \sum_{XZ} \boldsymbol{K}^b + \sum_{XZ} \boldsymbol{K}^f \tag{II.21}$$

$$\boldsymbol{M}_{xz} = \sum_{XZ}[{\boldsymbol{M}_T}^e + (1-2\gamma){\boldsymbol{M}_R}^e] + \sum_{XZ}[\left({\boldsymbol{M}_T}^d + {\boldsymbol{M}_R}^d\right) - \gamma\widehat{\boldsymbol{G}}^d] + \sum_{XZ} \boldsymbol{M}^f \tag{II.22}$$

$$\gamma = \frac{\omega}{\Omega} \tag{II.23}$$

It is desirable to have a separation of at least 10% from the critical speed [13]. For a given rotor, the primary method of changing the stiffness of the system is the bearing type. Changing the bearing from pressure dam to sleeve will change the stiffness and shift the overall critical speed of the rotating

system. The paper by Nicholas [38] showed that switching from a tilting pad to a sleeve bearing can shift the critical speed and reduce the overall vibration level in the system. Other than critical speed analysis, it is desireable to determine the rotor response to steady state synchronous excitations such as a mass unbalance. Unbalance in a rotating assembly creates forces which are discrete and located on different planes. The force has a magnitude of mass times eccentricity. The unbalance force can be represented by the matrix

$$\begin{Bmatrix} F_{u,x} \\ F_{u,y} \\ M_{u,x} \\ M_{u,y} \end{Bmatrix} = \begin{Bmatrix} me_m\omega^2\cos(\omega t + \phi_u) \\ me_m\omega^2\sin(\omega t + \phi_u) \\ 0 \\ 0 \end{Bmatrix} \tag{II.24}$$

The excitation forces can be input into the equation of motion, II.18. The steady state response can be represented by the following linear algebra equations

$$\begin{bmatrix} \boldsymbol{K} - \omega^2\boldsymbol{M} & \omega\boldsymbol{C} \\ -\omega\boldsymbol{C} & \boldsymbol{K} - \omega^2\boldsymbol{M} \end{bmatrix} \begin{Bmatrix} \boldsymbol{q}_c \\ \boldsymbol{q}_s \end{Bmatrix} = \begin{Bmatrix} \boldsymbol{Q}_c \\ \boldsymbol{Q}_s \end{Bmatrix} \tag{II.25}$$

These responses are then calculated and represented in Bode or Polar plots. These plots are presented in Section 3.5 and 3.6.

Transient responses are necessary to determine rotor motion for startups, shut downs, or any number of sudden excitations. The response of the rotor-bearing system to transients can be found by using a direct numerical integration method. DyRoBeS© offers several methods, including Newmark-β and Wilson-θ, but the primary one chosen for this study was the 4th order Runge-Kutta method. The Runge-Kutta method is used to solve the initial value problem, first-order, ordinary differential equation

$$\dot{\boldsymbol{x}} = f(\boldsymbol{x}, t) = \begin{Bmatrix} \boldsymbol{Q} \\ 0 \end{Bmatrix} - \begin{bmatrix} \boldsymbol{M}^{-1}\boldsymbol{C} & \boldsymbol{M}^{-1}\boldsymbol{K} \\ -\boldsymbol{I} & 0 \end{bmatrix} \begin{Bmatrix} \dot{\boldsymbol{q}} \\ \boldsymbol{q} \end{Bmatrix} \tag{II.26}$$

where

$$\dot{\boldsymbol{x}} = \begin{Bmatrix} \ddot{\boldsymbol{q}} \\ \dot{\boldsymbol{q}} \end{Bmatrix}, \boldsymbol{x} = \begin{Bmatrix} \dot{\boldsymbol{q}} \\ \boldsymbol{q} \end{Bmatrix} \tag{II.27}$$

This method is described in Appendix IV.

From the steps provided in Appendix I and II, a complete rotor-bearing system analysis can be performed. After modeling the two required bearings and building the finite-element model of the rotor, the rotor-bearing system performance can be analyzed which includes the critical speed locations, steady state synchronous reponses, and transient responses. The system model was built using the DyRoBeS© software package and is described in Chapter 3.0.

Appendix III: Elemental Matrices

From the work by Chen and Gunter [14], the matrices described in Appendix II will be shown in the following pages. Elemental mass and stiffness matrices in a single plane are required for the analysis of isotropic systems. The shaft element is assumed isotropic and axisymmetric about the z-axis (i.e the axis of rotation). The material is assumed to be homogenous. Matrices for two planes of motion can be obtained by extending the matrices of a single plane of motion [14]. Because the gyroscopic matrix **G** couples two planes, the full 8x8 matrix is given. First, the translational mass matrix is presented.

$$\boldsymbol{M}^{e}_{T,XZ} = \begin{bmatrix} m_{11} & & & \\ m_{41} & m_{44} & Sym & \\ m_{51} & m_{54} & m_{55} & \\ m_{81} & m_{84} & m_{85} & m_{88} \end{bmatrix} \tag{III.1}$$

where

$$m_{11} = \frac{\rho AL}{420(1+\Phi)^2}(156 + 294 * \Phi + 140 * \Phi^2) \tag{III.2}$$

$$m_{41} = \frac{\rho AL}{420(1+\Phi)^2}(22 + 38.5 * \Phi + 17.5 * \Phi^2) \tag{III.3}$$

$$m_{51} = \frac{\rho AL}{420(1+\Phi)^2}(54 + 126 * \Phi + 70 * \Phi^2) \tag{III.4}$$

$$m_{81} = \frac{\rho AL}{420(1+\Phi)^2}(-13 - 31.5 * \Phi - 17.5 * \Phi^2) \tag{III.5}$$

$$m_{44} = \frac{\rho AL}{420(1+\Phi)^2}(4 + 7 * \Phi + 3.5 * \Phi^2) \tag{III.6}$$

$$m_{84} = \frac{\rho AL}{420(1+\Phi)^2}(-3 - 7 * \Phi - 3.5 * \Phi^2) \tag{III.7}$$

$$m_{54} = -m_{81}, m_{55} = m_{11}, m_{85} = -m_{41}, m_{88} = m_{44} \tag{III.8}$$

Next, the rotatory mass matrix is presented, taken from the work by Chen and Gunter [14].

$$\boldsymbol{M}^{e}_{R,XZ} = \begin{bmatrix} n_{11} & & & \\ n_{41} & n_{44} & Sym & \\ n_{51} & n_{54} & n_{55} & \\ n_{81} & n_{84} & n_{85} & n_{88} \end{bmatrix} \tag{III.9}$$

where

$$n_{11} = \frac{\rho I}{30L(1+\Phi)^2}(36) \tag{III.10}$$

$$n_{41} = \frac{\rho I}{30L(1+\Phi)^2}(3 - 15 * \Phi)L \tag{III.11}$$

$$n_{44} = \frac{\rho I}{30L(1+\Phi)^2}(4 + 15 * \Phi + 10 * \Phi^2)L^2 \tag{III.12}$$

$$n_{84} = \frac{\rho I}{30L(1+\Phi)^2}(-1 - 5 * \Phi + 5 * \Phi^2)L^2 \tag{III.13}$$

$$n_{51} = -n_{11}, n_{81} = m_{41}, n_{54} = -n_{41}, n_{85} = -n_{41}, n_{88} = n_{44} \tag{III.14}$$

Next are the stiffness matrices, **K**. The stiffness matrix due to shaft bending and shear effects is first.

$$\boldsymbol{K}^{e}_{XZ} = \frac{EI}{L^3(1+\Phi)} \begin{bmatrix} 12 & & & \\ 6L & (4+\Phi) & Sym & \\ -12 & -6L & 12 & \\ 6L & (2-\Phi)L^2 & -6L & (4+\Phi)L^2 \end{bmatrix} \tag{III.15}$$

The stiffness matrix due to an axial load, P, is as follows [14].

$$\boldsymbol{K}^{e}_{XZ,a} = \begin{bmatrix} k_{11} & & & \\ k_{41} & k_{44} & Sym & \\ k_{51} & k_{54} & k_{55} & \\ k_{81} & k_{84} & k_{85} & k_{88} \end{bmatrix} \tag{III.16}$$

$$k_{11} = \frac{P}{30L(1+\Phi)^2}(36 + 60 * \Phi + 30 * \Phi^2) \tag{III.17}$$

$$k_{41} = \frac{P}{30L(1+\Phi)^2}(3L) \tag{III.18}$$

$$k_{44} = \frac{P}{30L(1+\Phi)^2}(4 + 5 * \Phi + 2.5 * \Phi^2)L^2 \quad \text{(III.19)}$$

$$k_{84} = \frac{P}{30L(1+\Phi)^2}(-1 - 5 * \Phi - 2.5 * \Phi^2)L^2 \quad \text{(III.20)}$$

$$k_{51} = -k_{11}, k_{81} = k_{41}, k_{54} = -k_{41}, k_{85} = -k_{41}, k_{88} = k_{44} \quad \text{(III.21)}$$

Finally, the gyroscopic matrix **G** is shown. Note **G** is a complete 8x8 matrix.

$$\boldsymbol{G}^e = \begin{bmatrix} 0 & & & & & & & \\ g_{21} & 0 & & & & Skew\ Sym & & \\ g_{31} & 0 & 0 & & & & & \\ 0 & g_{42} & g_{43} & 0 & & & & \\ 0 & g_{52} & g_{53} & 0 & 0 & & & \\ g_{61} & 0 & 0 & g_{64} & g_{65} & 0 & & \\ g_{71} & 0 & 0 & g_{74} & g_{75} & 0 & 0 & \\ 0 & g_{82} & g_{82} & 0 & 0 & g_{86} & g_{87} & 0 \end{bmatrix} \quad \text{(III.22)}$$

$$g_{11} = -2n_{11} = \frac{\rho I}{15L(1+\Phi)^2}(36) \quad \text{(III.23)}$$

$$g_{31} = 2n_{41} = \frac{\rho I}{15L(1+\Phi)^2}(3 - 15 * \Phi)L \quad \text{(III.24)}$$

$$g_{43} = -2n_{44} = \frac{\rho I}{15L(1+\Phi)^2}(4 + 15 * \Phi + 10 * \Phi^2)L^2 \quad \text{(III.25)}$$

$$g_{83} = -2n_{84} = \frac{\rho I}{30L(1+\Phi)^2}(-1 - 5 * \Phi + 5 * \Phi^2)L^2 \quad \text{(III.26)}$$

$$g_{61} = -g_{21},\ g_{71} = g_{31},\ g_{42} = g_{31},\ g_{52} = g_{21},\ g_{82} = g_{31} \quad \text{(III.27)}$$

$$g_{53} = g_{31},\ g_{64} = g_{31},\ g_{74} = -g_{83},\ g_{65} = -g_{21},\ g_{75} = -g_{31}$$

$$g_{86} = -g_{31},\ g_{87} = g_{43}$$

Note the coefficients are closely related to those in the rotatory mass matrix. These equations were taken from Appendix B of the work by Chen and Gunter [14]. Finally, the conversion matrix from one plane of motion to two planes of motion is given in matrix **A.** A 4x4 symmetric matrix is used to

represent one plane of motion. The 8x8 complete matrix **A** is the full matrix for both planes. Substitute **M** or **K** for **A** as required if modeling the motion in both planes.

$$\boldsymbol{A} = \begin{bmatrix} a_{11} & & & & & & & \\ 0 & a_{22} & & & & & Sym & \\ 0 & a_{32} & a_{33} & & & & & \\ a_{41} & 0 & 0 & a_{44} & & & & \\ a_{51} & 0 & 0 & a_{54} & a_{55} & & & \\ 0 & a_{62} & a_{63} & 0 & 0 & a_{66} & & \\ 0 & a_{72} & a_{73} & 0 & 0 & a_{76} & a_{77} & \\ a_{81} & 0 & 0 & a_{84} & a_{85} & 0 & 0 & a_{88} \end{bmatrix} \tag{III.28}$$

The coefficients in the Y-Z plane are given by those in the X-Z plane [14]:

$$a_{22} = a_{11},\ a_{33} = a_{44},\ a_{66} = a_{55},\ a_{77} = a_{88} \tag{III.29}$$

$$a_{32} = -a_{41},\ a_{62} = a_{51},\ a_{72} = -a_{81}$$

$$a_{63} = -g_{54},\ a_{73} = a_{84}, a_{76} = -a_{85}$$

Finally, due to its use in many of the previous equations, the transverse shear effect parameter Φ will be repeated here as it was in Appendix II.

$$\Phi = \frac{12EI}{kAGL^2} \tag{III.30}$$

where k is the shape factor, a function of the Poisson's ratio ν of the material. For solid shafts,

$$k = \frac{6(1+\upsilon)}{(7+6\upsilon)} \tag{III.31}$$

and for thin-walled tubes

$$k = \frac{2(1+\upsilon)}{(4+3\upsilon)} \tag{III.32}$$

Appendix IV: Runge-Kutta Method

The Runge-Kutta Method is a method of numerically integrating ordinary differential equations to form approximate solutions of these ODE problems. Runge-Kutta methods are a family of iterative methods for solving ordinary differential equations. The following will present the most common, known as the classical Runge-Kutta method or RK4 [62]. For an initial value problem defined as follows,

$$\dot{y} = f(t, y), y(t_0) = y_0 \tag{IV.1}$$

where y is an unknown function of time t that is being approximated, and $\dot{y}$ is the rate at which y changes, which is a function of t and y. At the initial time t_0, the function equals y_0. Using the Runge-Kutta method, the value y_{n+1} is calculated using the present value, y_n, and a weighted average of four increments, w_n. These weighted increments are functions of the step-size h.The weighted increment functions can vary depending on the form of Runge-Kutta being used, but for this example the solution is presented as follows,

$$y_{n+1} = y_n + \frac{1}{6}h(w_1 + 2w_2 + 2w_3 + w_4) \tag{IV.2}$$

where

$$t_{n+1} = t_n + h \tag{IV.3}$$

$$w_1 = f(t_n, y_n) \tag{IV.4}$$

$$w_2 = f(t_n + \frac{1}{2}h, y_n + \frac{h}{2}w_1) \tag{IV.5}$$

$$w_3 = f(t_n + \frac{1}{2}h, y_n + \frac{h}{2}w_2) \tag{IV.6}$$

$$w_4 = f(t_n + \frac{1}{2}h, y_n + hw_3) \tag{IV.7}$$

This method can be expanded for systems of ordinary differential equations with an equal number of individual initial conditions for each ordinary differential equation in the system. DyRoBeS© uses this method to numerically solve transient rotordynamic problems solving systems of finite element equations as shown in Appendix II. For a further look at the various types of Runge-Kutta methods and other methods of numerically solving differential equations, the author refers the reader to the work by Quarteroni, Sacco, and Saleri [62].

Appendix V: Bearing Characteristics

Pressure Dam Bearing Performance at Operating Temperature

RPM	Eccentricity/ Clearance	Attitude Angle (°)	Min. Film Thickness/Clearance	Maximum Pressure (psi)	Power Input (HP)	Frictional Power Loss (HP)
600	0.784	33	0.216	653.47	1.65	1.158
800	0.756	35	0.244	627.53	2.61	1.521
1000	0.734	37	0.266	610.32	3.75	1.876
1200	0.716	38	0.284	598.8	4.99	2.229
1400	0.7	39	0.3	590.77	6.35	2.578
1600	0.687	40	0.313	585.59	7.84	2.926
1800	0.676	41	0.324	582.05	9.46	3.272
2000	0.667	42	0.333	579.99	11.13	3.622
2200	0.658	43	0.342	578.88	12.97	3.969
2400	0.65	43	0.35	578.41	14.89	4.318
2600	0.643	44	0.357	578.96	16.91	4.669
2800	0.637	45	0.363	580.71	19.05	5.024
3000	0.632	45	0.368	582.68	21.28	5.381
3200	0.627	46	0.373	585.27	23.62	5.741
3400	0.623	46	0.377	588.61	26.1	6.106
3600	0.618	46	0.382	591.64	28.77	6.463
3800	0.614	47	0.386	595.51	31.45	6.833
4000	0.611	47	0.389	599.82	34.25	7.207

RPM	Heat Input (BTU)	Inlet Oil Temp (°F)	Operating Oil Film Temp (°F)	Max Oil Film Temp (°F)	Critical Journal Mass (lbf-s^2/in)	Instability Whirl Ratio
600	0	100	112	147	1.28E+07	0.192
800	0	100	115	150	6020	0.211
1000	0	100	117	155	1366	0.36
1200	0	100	119	159	830.4	0.388
1400	0	100	121	161	722.1	0.357
1600	0	100	123	165	464.9	0.393
1800	0	100	125	169	324.3	0.423
2000	0	100	127	171	281.1	0.41
2200	0	100	128	174	208.7	0.437
2400	0	100	130	177	184.6	0.428
2600	0	100	131	179	165	0.42
2800	0	100	133	182	129.1	0.445
3000	0	100	134	184	116.8	0.439
3200	0	100	136	186	106.4	0.433

RPM	Heat Input (BTU)	Inlet Oil Temp (°F)	Operating Oil Film Temp (°F)	Max Oil Film Temp (°F)	Critical Journal Mass (lbf-s^2/in)	Instability Whirl Ratio
3400	0	100	137	190	87.08	0.456
3600	0	100	138	192	80.3	0.451
3800	0	100	140	194	74.26	0.447
4000	0	100	141	196	69.01	0.443

RPM	Sommerfeld Number	Kxx (lbf/in)	Kxy (lbf/in)	Kyx (lbf/in)	Kyy (lbf/in)
600	0.161	2.35E+06	-5.05E+05	-5.93E+06	8.75E+06
800	0.201	2.34E+06	-4.00E+05	-5.69E+06	7.90E+06
1000	0.238	2.48E+06	-1.81E+05	-5.71E+06	7.15E+06
1200	0.27	2.53E+06	-7.18E+04	-5.67E+06	6.72E+06
1400	0.3	2.49E+06	-7.63E+04	-5.55E+06	6.52E+06
1600	0.327	2.57E+06	3.52E+04	-5.59E+06	6.24E+06
1800	0.353	2.65E+06	1.51E+05	-5.64E+06	5.99E+06
2000	0.374	2.64E+06	1.48E+05	-5.61E+06	5.92E+06
2200	0.397	2.74E+06	2.67E+05	-5.70E+06	5.73E+06
2400	0.417	2.74E+06	2.65E+05	-5.69E+06	5.69E+06
2600	0.436	2.75E+06	2.64E+05	-5.69E+06	5.66E+06
2800	0.454	2.86E+06	3.87E+05	-5.80E+06	5.52E+06
3000	0.471	2.87E+06	3.86E+05	-5.82E+06	5.51E+06
3200	0.487	2.89E+06	3.84E+05	-5.85E+06	5.51E+06
3400	0.502	3.01E+06	5.14E+05	-5.98E+06	5.40E+06
3600	0.519	3.03E+06	5.14E+05	-6.01E+06	5.40E+06
3800	0.533	3.06E+06	5.12E+05	-6.05E+06	5.42E+06
4000	0.547	3.08E+06	5.10E+05	-6.10E+06	5.45E+06

RPM	Cxx (lbf-s/in)	Cxy (lbf-s/in)	Cyx (lbf-s/in)	Cyy (lbf-s/in)
600	2.86E+04	-4.33E+04	-4.33E+04	1.65E+05
800	2.24E+04	-3.11E+04	-3.11E+04	1.17E+05
1000	2.12E+04	-2.74E+04	-2.74E+04	9.47E+04
1200	1.90E+04	-2.33E+04	-2.33E+04	7.82E+04
1400	1.60E+04	-1.88E+04	-1.88E+04	6.50E+04
1600	1.52E+04	-1.72E+04	-1.72E+04	5.73E+04
1800	1.47E+04	-1.61E+04	-1.61E+04	5.16E+04
2000	1.32E+04	-1.41E+04	-1.41E+04	4.59E+04
2200	1.31E+04	-1.36E+04	-1.36E+04	4.25E+04
2400	1.20E+04	-1.22E+04	-1.22E+04	3.87E+04
2600	1.11E+04	-1.11E+04	-1.11E+04	3.56E+04

RPM	Cxx (lbf-s/in)	Cxy (lbf-s/in)	Cyx (lbf-s/in)	Cyy (lbf-s/in)
2800	1.13E+04	-1.10E+04	-1.10E+04	3.38E+04
3000	1.06E+04	-1.02E+04	-1.02E+04	3.15E+04
3200	9.97E+03	-9.44E+03	-9.44E+03	2.96E+04
3400	1.02E+04	-9.54E+03	-9.54E+03	2.85E+04
3600	9.73E+03	-8.95E+03	-8.95E+03	2.70E+04
3800	9.30E+03	-8.46E+03	-8.46E+03	2.57E+04
4000	8.92E+03	-8.03E+03	-8.02E+03	2.45E+04

Sleeve Bearing Performance at Operating Temperature

RPM	Eccentricity/ Clearance	Attitude Angle (°)	Min. Film Thickness/Clearance	Maximum Pressure (psi)	Power Input (HP)	Frictional Power Loss (HP)
600	0.487	59	0.513	293.41	1.44	0.994
800	0.465	66	0.535	297.07	2.3	1.216
1000	0.396	63	0.604	275.81	3.19	1.367
1200	0.396	70	0.604	284.89	4.24	1.557
1400	0.349	65	0.651	269.1	5.33	1.684
1600	0.332	66	0.668	266.85	6.5	1.848
1800	0.317	67	0.683	264.99	7.76	2.001
2000	0.327	73	0.673	274.84	9.05	2.158
2200	0.299	68	0.701	263.15	10.36	2.273
2400	0.29	69	0.71	262.12	11.76	2.421
2600	0.28	69	0.72	261.14	13.21	2.55
2800	0.273	70	0.727	260.3	14.76	2.689
3000	0.267	70	0.733	259.7	16.35	2.829
3200	0.262	71	0.738	259.15	18	2.967
3400	0.257	71	0.743	258.66	19.72	3.102
3600	0.253	71	0.747	258.3	21.43	3.245
3800	0.267	77	0.733	267.89	23.14	3.39
4000	0.262	77	0.738	267.38	25.1	3.507

RPM	Heat Input (BTU)	Inlet Oil Temp (°F)	Operating Oil Film Temp (°F)	Max Oil Film Temp (°F)	Critical Journal Mass (lbf-s^2/in)	Instability Whirl Ratio
600	0	100	112	124	2381	0.427
800	0	100	116	139	1217	0.486
1000	0	100	120	135	679.5	0.488
1200	0	100	123	149	512.3	0.486
1400	0	100	127	144	341.9	0.491

RPM	Heat Input (BTU)	Inlet Oil Temp (°F)	Operating Oil Film Temp (°F)	Max Oil Film Temp (°F)	Critical Journal Mass (lbf-s^2/in)	Instability Whirl Ratio
1600	0	100	130	148	262.6	0.491
1800	0	100	133	151	208	0.491
2000	0	100	136	166	174.6	0.488
2200	0	100	139	159	137.1	0.495
2400	0	100	142	162	115.4	0.495
2600	0	100	144	165	98.72	0.496
2800	0	100	147	169	85.29	0.496
3000	0	100	149	171	74.43	0.496
3200	0	100	152	174	65.53	0.496
3400	0	100	154	177	58.14	0.496
3600	0	100	157	180	51.94	0.496
3800	0	100	159	197	46.59	0.491
4000	0	100	161	200	41.95	0.491

RPM	Sommerfeld Number	Kxx (lbf/in)	Kxy (lbf/in)	Kyx (lbf/in)	Kyy (lbf/in)
600	0.16	2.02E+06	7.50E+05	-3.74E+06	2.72E+06
800	0.192	1.38E+06	7.21E+06	-5.42E+06	2.18E+06
1000	0.218	2.36E+06	2.02E+06	-4.27E+06	1.94E+06
1200	0.242	1.14E+06	7.93E+06	-6.28E+06	2.32E+06
1400	0.258	2.37E+06	2.37E+06	-4.59E+06	1.81E+06
1600	0.275	2.36E+06	2.45E+06	-4.72E+06	1.80E+06
1800	0.29	2.35E+06	2.54E+06	-4.85E+06	1.80E+06
2000	0.305	9.45E+05	9.01E+06	-7.59E+06	2.45E+06
2200	0.31	2.41E+06	2.90E+06	-5.09E+06	1.67E+06
2400	0.319	2.41E+06	2.96E+06	-5.19E+06	1.67E+06
2600	0.331	2.46E+06	3.36E+06	-5.33E+06	1.58E+06
2800	0.339	2.46E+06	3.43E+06	-5.43E+06	1.58E+06
3000	0.346	2.46E+06	3.49E+06	-5.51E+06	1.58E+06
3200	0.352	2.46E+06	3.55E+06	-5.59E+06	1.58E+06
3400	0.357	2.46E+06	3.61E+06	-5.67E+06	1.58E+06
3600	0.36	2.46E+06	3.65E+06	-5.74E+06	1.58E+06
3800	0.365	8.30E+05	1.05E+07	-9.36E+06	2.56E+06
4000	0.37	8.24E+05	1.07E+07	-9.55E+06	2.57E+06

RPM	Cxx (lbf-s/in)	Cxy (lbf-s/in)	Cyx (lbf-s/in)	Cyy (lbf-s/in)
600	4.50E+04	-2.67E+04	-2.67E+04	1.12E+05
800	1.85E+05	-2.89E+04	-2.89E+04	1.32E+05

RPM	Cxx (lbf-s/in)	Cxy (lbf-s/in)	Cyx (lbf-s/in)	Cyy (lbf-s/in)
1000	4.89E+04	-2.44E+04	-2.44E+04	8.05E+04
1200	1.34E+05	-1.37E+04	-1.37E+04	1.01E+05
1400	3.86E+04	-1.73E+04	-1.73E+04	6.21E+04
1600	3.45E+04	-1.47E+04	-1.47E+04	5.58E+04
1800	3.14E+04	-1.27E+04	-1.27E+04	5.09E+04
2000	8.99E+04	-5.48E+03	-5.48E+03	7.26E+04
2200	2.86E+04	-1.13E+04	-1.13E+04	4.41E+04
2400	2.66E+04	-1.02E+04	-1.02E+04	4.11E+04
2600	2.75E+04	-9.99E+03	-9.99E+03	3.90E+04
2800	2.59E+04	-9.18E+03	-9.18E+03	3.69E+04
3000	2.45E+04	-8.50E+03	-8.50E+03	3.49E+04
3200	2.33E+04	-7.90E+03	-7.90E+03	3.32E+04
3400	2.22E+04	-7.38E+03	-7.38E+03	3.17E+04
3600	2.12E+04	-6.92E+03	-6.92E+03	3.03E+04
3800	5.45E+04	-1.83E+03	-1.83E+03	4.69E+04
4000	5.25E+04	-1.66E+03	-1.66E+03	4.54E+04

Vita

Justin Garrard graduated from Coffee County Central High School in 2007. He attended Tennessee Technological University from August 2007- December 2010, where he graduated with a Bachelor of Science degree in Mechanical Engineering. After graduation, he accepted a position in January 2011 as a mechanical system engineer in the Propulsion Wind Tunnel and Von Karman Gas Dynamics facilities for the primary contractor, Aerospace Testing Alliance, at Arnold AFB, TN. As a mechanical system engineer, he has managed dessicant air dryer and air cooler systems for both facilities. He currently is the mechanical system engineer for the Von Karman Gas Dynamics facility compressor drive system including all electrical motors and compressors. He is obtaining a Master of Science degree in Mechanical Engineering from the University of Tennessee. In the future, he plans to obtain his Professional Engineering license and continue his education, working to obtain the Doctor of Philosophy degree in Mechanical Engineering from the University of Tennessee.